Bio-inspired cell sense-and-respond systems through bio-synthetic and robotics approaches

Submitted in partial fulfillment of the requirements for

the degree of

Doctor of Philosophy

in

Mechanical Engineering

Kyle Blaine Justus

B.S., Mechanical Engineering, Michigan State University

Carnegie Mellon University
Pittsburgh, PA

May 2017

Acknowledgments

I would like to express my sincere gratitude to all of those who provided support and assistance throughout the course of my PhD. First, I would like to thank my advisors, Professors Phil LeDuc, Carmel Majidi and Cheemeng Tan. I would also like to thank Eric Parigoris for his 4 years of fantastic work as an undergraduate researcher working alongside me. I'd also like to thank the rest of the members of the LeDuc Lab, specifically Melis Hazar Lina Gonzalez, Mary Beth Wilson, Adam Wood and Brian Stancil for their contributions and valuable input. I would also like to thank Daniel Lewis and Tess Hellebrekers for their contributions as well as the members of the Integrated Soft Machines Lab. I would also like to thank the funding agencies that made this work possible, specifically the National Science Foundation Graduate Research Fellowship Program under (Grant DGE1252522), the National Science Foundation (Grant CBET-1547810) and the Air Force Office of Scientific Research (Grant FA9550-13-1-01 08). For their impact and support outside of the lab, I would like to thank my loving girlfriend, Lauren Finkenauer, my parents, Bill and Sandy, my siblings, Kevin, Megan and Maggie and my good friends Kosa Goucher-Lambert, Chandrajit Thaokar and Justin Freedman. Finally, I would like to thank the members of my committee, listed below.

Thesis Committee:

Philip R. LeDuc, PhD (Chair)

Carmel Majidi, PhD

Cheemeng Tan, PhD

Rebecca Taylor, PhD

Table of Contents

Table of Figures

Figure 5.3(A) Microvilli stained using fluorescently tagged villin antibody under healthy conditions. (B) Tight junction protein ZO-1 stained using fluorescently tagged anti-ZO-1 antibody under healthy conditions. (C) Caco-2 stained for actin using fluorescently tagged phalloidin (green channel) and nuclei with DAPI (1) under normal conditions. (D) Caco-2 cells

Abstract

Living systems have developed intricate multi-functional methods of sensing and responding to their surroundings at the cellular level at low spatial and energetic costs. Exploiting or mimicking these functionalities would have tremendous implications in both wearable devices, where both weight and power requirements are limiting factors, and drug delivery, where timed, localized release can have tremendous impact on drug efficacy. These goals can be achieved by either altering existing structures, such as modifying genetics in organisms to respond to stimuli, or by building synthetic lipid vesicle systems to mimic cellular morphologies. To the end of altering existing biological frameworks, we have genetically modified strains of *Escherichia coli* to function as chemical sensors within flexible, biomimetic systems. This approach expands the functionalities of soft machines at low cost to spatial and power considerations, two limiting factors to the development of these devices. By utilizing existing biological architecture and implementing modified organisms in flexible devices, we can produce high-functioning, low-energy wearable bio-sensors. Alternatively, we have also worked to replicate the mechanical sensing capabilities of cellular systems from a bottom-up direction, building a liposome-based system designed to sense mechanical deformation due to external forces. This device could be used as a localized drug release mechanism capable of responding to cues from outside of the body, as well as the framework for an artificial mechanotransduction system. To test this, we have developed a gut-on-a-chip framework in which to apply the magnetoliposomes for controlled rupture and localized drug delivery.

Chapter 1 Introduction

Cell Sense-and-Respond Mechanisms

Cellular systems exhibit a phenomenal capacity for interacting and responding with myriad environments, translating numerous inputs or cues into outputs. These inputs can comprise mechanical forces, chemical stimuli or gradients, light sources, electrical impulses and others while common responses can produce energy, movement, chemical release or cytoskeletal reinforcement. This versatility in combination with the general compactness of cells yields promise for exciting avenues in biotechnology related to exploiting these sense-and-respond capabilities in larger systems. The fields of synthetic biology and metabolic engineering are based around this principle, in essence modifying the genetic components of cells to function as miniature machines or production facilities.

From an engineering perspective, a common way to approach a system featuring measurable inputs and outputs is that of the classical controls approach featuring a plant and a corresponding transfer function. Using this transfer function, typically defined in s-space rather than the time-domain, one can relate the dynamics of the input of the system to the output. This approach is highly effective in linear bounded input, bounded output (BIBO) systems and can also be applied in non-linear or decentralized cases. In the case of mechanical systems with traditional components, one can often characterize the dynamics of the system using equations of motion and then implement

control strategies to stabilize an output or improve response times using sensors, controllers and compensators.

In the realm of cellular systems, we see analogous biological components that allow cells to dynamically respond to a variety of inputs and produce measureable outputs. These inputs can be mechanical in nature, including mechanical forces (*3, 4*), substrate stiffness (*5-7*) or shear flow (*8, 9*). In these cases, cells often elicit electrochemical responses in the form of mechanotransduction where the stimulus is converted through a complex signal transduction pathway. Similarly, cells can exhibit responses to substrate stiffness by spreading or through cell motility. While the ultimate outputs of these sense-and-respond mechanisms are easily observable using optical microscopy, the intermediate events often involving receptor proteins and cascading pathways are much more difficult to delineate. For instance, the focal adhesion complex, which is an essential part of cell spreading and motility, features a large number of interconnected components (Geiger, 2009 #7611) .

Beyond mechanical inputs, cellular systems are able to sense and respond to a wide variety of cues and inputs. These inputs can be light (*10-12*) (*13*), chemical (*14*), electrical (*15-17*), cell-cell communication quorum sensing (*18*) (*19*) (*20*) (*21*)) and others. There is perhaps no better example of this sensitivity and corresponding versatility than stem cells, which can differentiate into a variety of cell types depending on the microenvironment (*22*).   Because of this multitude of sensitivities to microenvironments, responses can be difficult to isolate for applications in biotechnology (Figure 1.2).
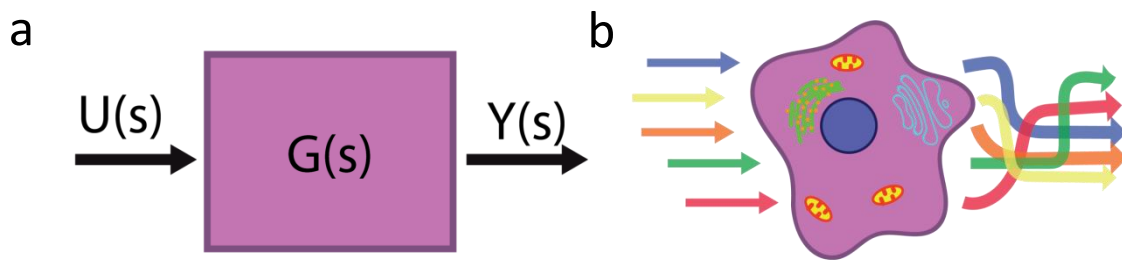
Figure 1.1 a) Schematic of a block diagram in classical control theory with input U(s) and output Y(s) related by the transfer function G(s). (b) Representation of a cell as a system subjective to numerous inputs and producing a complex combination of responses.

Efforts to exploit or mimic the inherent biological components associated with organisms' abilities to interact with environments. At the meso-scale, bioinspired design is commonplace in fields such as robotics and materials development. Within robotics, researchers look to organisms to inspire bipedal locomotion (*23*) (*24*) (*25*) as well as swimming (*26*) (*27-30*) and grasping (*31*) (*32, 33*) (*34*). Traditional robots are noted for their ability to define a well-defined task quickly and repeatability but possess limited adaptability, an area where biological organisms excel. A main reason for this proficiency in organisms is the nervous system, which is effectively a soft, embedded sensory network capable of providing feedback to mechanical inputs across the surface volume of the organism. Conversely, due to hardware limitations and power consumption, robotic systems lack this expansive array of feedback to direct actions.

In an effort to emulate the versatility of living organisms, the field of soft robotics has developed with the aim of improving the capabilities of robotics from a materials perspective. While traditional robotics relies on discrete, rigid components, most organisms are a combination of soft tissue and rigid skeletal structure working in concert. To address this, efforts have been made to develop soft robots to function as
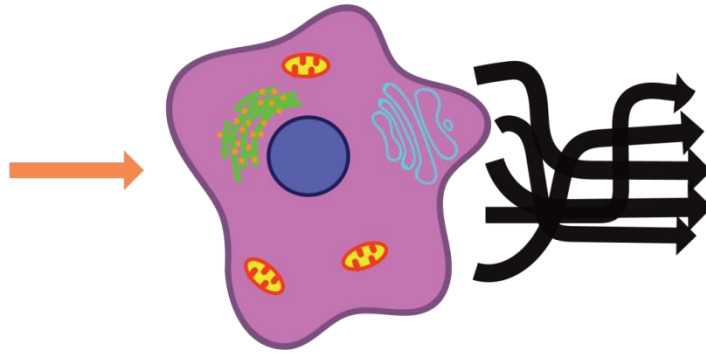
Figure 1.2 Representation of coupled responses to a solitary input due to the complex internal components and sensitivities of cells. This non-linear "black box" produces challenges with regards to exploiting the inherent abilities in biotechnology applications.

wearable skins, typically composed of electrically conductive elastomers or liquid metals embedded within elastomers (*35-38*), though issues still remain with regards to compact power sources.

Fully soft robotic architectures are also limited by the materials themselves with regards to both force exertion and power consumption. Due to the low mechanical stiffness of the elastomers typically used in soft robotics, controlled deformation when subjected to loads is very difficult to achieve. While rigid members connected at discrete joints in traditional robotic systems can often be modeled and subsequently controlled using dynamics and classical control systems theory approaches, soft roboticists currently lack this plethora of tools and techniques (*39*). This is due in large part to the fact that deflection of these soft devices must be characterized as a continuous curve rather than a series of vectors. Furthermore, the materials make it difficult to predict the deformation under loading conditions due to the many degrees of freedom.

Existing methods for actuation of soft robotics are typically hydraulic-based or utilize electrically-actuated materials such as dielectric elastomers (DEAs) (*40*) (*41*) (*42*) (*43*)
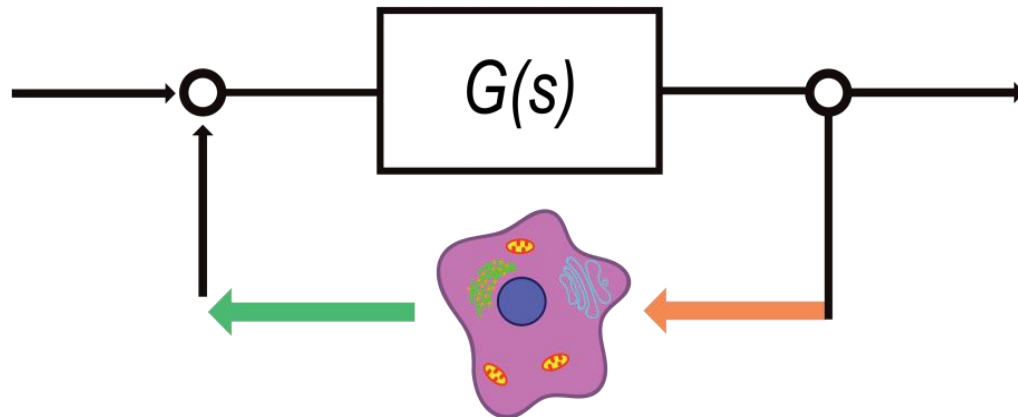
Figure 1.3 Representation of a cellular system featuring a robust input-output relationship being utilized as a sensing component within a larger device.

or shape memory alloys (SMAs) (*44-46*). Embedded hydraulic systems rely on compressed air or fluid to actuate as "artificial muscles" (*50*) (*51*) (*52, 53*). However, these systems lack the compactness seen *in vivo* and their reservoirs are typically too bulky to allow for autonomy. Similarly, autonomous systems featuring DEAs and SMAs would require soft, stretchable battery technologies with capacities beyond the current state-of-the-art (*47-49*). Conversely, fully soft organisms such as cephalopods and annelids demonstrate excellent control over their soft bodies and remain autonomous due to their compact actuation systems in the form of muscles, their nervous systems for feedback, and their dependence on energy-dense chemical compounds for food (*39*). Additionally, efforts have been made to incorporate muscle cells into polymer thin films to produce biohybrid soft robots capable of swimming (*54*). Despite these efforts, the capabilities of bio-inspired devices still lag far behind those of living organisms due to the versatility of cells.

Synthetic biologists work to emulate and exploit this versatility of cellular systems by working primarily at the cellular and sub-cellular levels. According to Andrianantoandro
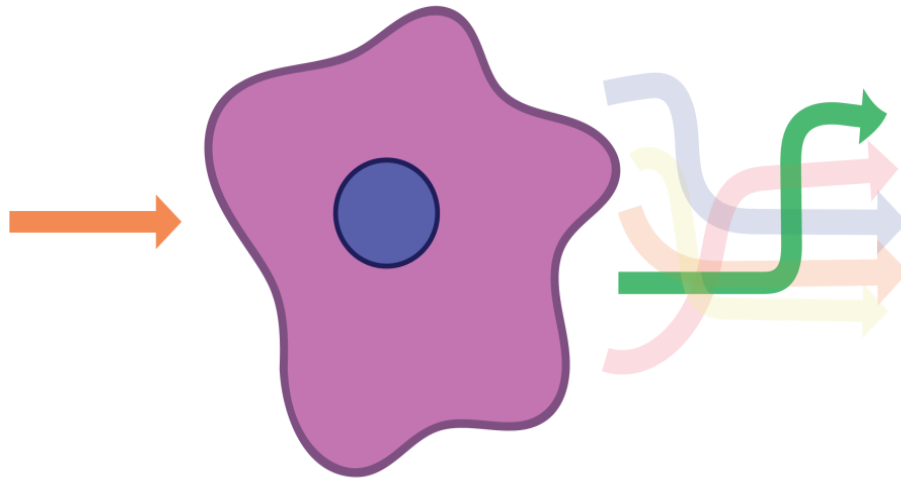
Figure 1.4 A reduced order system designed to emphasize specific inputs and outputs.

et al, the overarching objective of the field is to "extend or modify the behavior of organisms and engineer them to perform new tasks" (*55*). These efforts can be focused on genetic engineering, where the DNA of existing cells is modified to encode certain proteins. This has produced genetic circuits capable of functioning as toggle switches (*56*), computational modules (*57*) (*58*) (*59*) and light-sensitive circuits (*60, 61*). From the perspective of a cell functioning as a computer, the associated proteins and genes can be compared to the electronic components (i.e. capacitors, diodes, etc.) and the biochemical reactions such as translation and post-translational modification are analogous to the gates which the aforementioned electronic components are arranged to create. Furthermore, the metabolic or signal transduction pathways are similar to modules found within physical computers (*55*).

In the following chapters, we explore two approaches to utilize cellular sense-and-respond motifs for applications in biotechnology. The first approach involves the implementation of genetically modified cells as functional components within a

functional device. To achieve this, one must use or create a cellular system with a robust input-output relation to produce a useable signal. As described in the following chapters, we accomplish this by modifying *E. coli* cells with a genetic module that cause the cells to function as a chemical sensor which responds to the input IPTG and outputs green fluorescent protein (GFP) as a measurable signal.

The second approach detailed in the following work is to create a reduced order synthetic system by eliminating components extraneous to the desired outcome. We attempt this by designing a liposome-based system sensitive to external magnetic forces to trigger localized drug release. To meet this goal, a microfluidic chip for live imaging of magnetic tensile cytometry was developed in parallel. Lastly, these efforts were supplemented with the development of a gut-on-a-chip platform with which to ultimately test the capabilities of the magnetically-triggered drug delivery system.

Chapter 2 Materials and Methods

Soft Robotics and Synthetic Biology

Biological components

Chemo-sensing cells

The *Escherichia coli* BL21(DE3) was used to create z-competent cells before transformation. The plasmid *pIV_GFP* was created in a previous work (*139*) and inserted into cells to allow for synthesis of GFP (Figure 2.1A). This plasmid was designed to initiate transcription of the *gfp* gene in presence of the chemical stimulus isopropyl β-D-1-thiogalactopyranoside (IPTG) (Figure 2.2).

These cells grow well in luria broth (LB) as well as M9. Depending on the test, we would switch between the two of them. LB was advantageous in that it allowed the cells to grow more rapidly but especially in early stages of fluorescence imaging, there was a significant auto-fluorescence signal due to the media. This was most noticeable when testing was performed using a broadband imaging approach with a UV-Vis spectrometer. As a result of this auto-fluorescence, we typically used M9 media for any sort of fluorescence imaging outside of a plate reader, where it is very easily to account for the auto-fluorescence of LB. The cells grow less rapidly in M9 media but the media is optically transparent (in comparison to the orange translucency of LB) and shows extremely low levels of autofluorescence.

Constructing Optogenetic Plasmid

To construct a plasmid capable of changing gene expression in response to blue light, we digested the pDusk plasmid (Addgene 43795) with SalI and NotI, ligated in a PCR fragment containing GFP, and transformed the assembled vector into Top10 cells (Figure 2.1B). Variants of pDusk_GFP, pDusk_v37_GFP and pDusk_v38_GFP were made by changing the ribosome binding site. The ribosome binding site was manipulated by annealing two short single stranded DNA oligomers together to form an insert with a new RBS, then phosphorylating the insert, and ligating the insert with the vector at the XbaI and SalI sites.

Similarly to the chemo-sensing cells, the opto-sensitive cells grow in both LB and M9. However, due to the fact that the cells are responding to light, testing was primarily performed with M9 media due to the optical transparency of the media itself (Figure 2.3).

Growth rate detection

The growth rate of the bacteria within the device was measured either through a Beckman Coulter DU730 UV-vis spectrophotometer (Beckman Coulter, Brea, CA, USA) or using a Tecan SafireII plate reader (Tecan, Mannedorf, Switzerland) depending on the nature of the imaging (Figure 2.4). The UV-Vis spectrophotometer was used in early prototyping when volumes of roughly 500 µL were grown in patterned wells of varying shapes. This volume allowed us to use cuvettes rather than rely on 96 well plates for the measurements. For later testing, when the biological volumes decreased to below 300 µL for the whole device, optical density measurements were performed using the plate readers, typically in combination with a fluorescence readout for *gfp* gene

expression. Optical density measurements at 600nm wavelengths were recorded before the introduction of the bacteria to the device and after subsequent growth in an incubated shaker (37 °C).

Testing for growth rates in varying well geometries were carried out using 3-D printed molds of 1mL polygonal prisms with basal geometries of a circle, ellipsoid, rhombus and square (Figure 2.5). These volumes were accessed laterally by channels 1mm in width and height to allow for introduction of bacteria in liquid media. To increase testing through-put, I placed triplicates of each shape onto a single PDMS chip. The patterned wells were sealed with PDMS membranes roughly 1-2mm thick, and membrane thickness could have a significant impact on the growth rate of the cells as PDMS is oxygen permeable. A thinner PDMS membrane would yield a higher availability of oxygen which would then lend itself to aerobic growth of the bacteria. It was challenging to produce a membrane that was uniform thickness by pouring a prescribed volume into a petri dish due to un-level surfaces and the pre-polymer wetting the edges of the petri dish to form a meniscus.

In retrospect, I would suggest using a thin film applicator on heat-release tape to achieve the uniform thickness. This method is described in detail in the membrane fabrication section of these methods, but is briefly outlined as follows. First, cut the heat-release tape sheet to size, remove the top, clear protective layer and adhere the heat-release tape (120 °C is preferred) to a smooth, level surface. In my case, I used an aluminum plate. Pour the PDMS pre-polymer along the top edge of your heat-release tape and set the thin-film applicators clearance to your desired height plus the thickness of the tape itself. The carriage of the thin-film application should be wider than the tape

itself, allowing you to glide smoothly over it provided you are using a smooth level surface such as the aforementioned aluminum plate. Slowly draw the thin-film applicator down the length of the tape and ensure a smooth, even coverage across the entirety of the sheet. In the case that there are bare regions, simply pour additional pre-polymer "upstream" of those locations and repeat the pass with the thin-film applicator.

For the optical density measurements, the bacteria were allowed to grow in the patterned wells on an incubated shaker table at 37 °C for a period of 8 hours. Triplicates for every well geometry were measured at 2 hours intervals via extraction and then introduction into an appropriately sized cuvette (Figure 2.4). Rather than risking contamination or disrupting the growth of the cells through removal of the shaker, measurement and then reintroduction to the growth set-up, pre-designated triplicates were set aside for each time point, requiring 4 chips in total for a single growth curve. The three bacteria samples required for each of the 4 chips were held constant across the length of the experiment (i.e. diluted overnight cultures A, B and C were injected as triplicates A, B and C respectively in each of the 4 chips).

Protein expression measurement

The fluorescence intensity of reporter proteins was measured using a Tecan Infinite M1000 plate reader (Tecan, Mannedorf, Switzerland). Fluorescence intensities were normalized by optical density measurements to obtain average intensity per cells. Because the primary fluorophore of interest was green fluorescent protein, typical excitation and emission wavelengths were based off the default settings of the device (490nm and 520nm, respectively). With the exception of the growth curve measurements, all measurements are performed at or after the onset of logarithmic

growth to produce a robust signal and response.

Culture well fabrication

The culture wells were created using a negative plastic master mold via 3D printing (Stratasys, Eden Prairie, MN) due to the deep feature depths, which are more difficult to achieve with traditional photolithography approaches (Figure 2.6). Desired molds were produced using SolidWorks (Dassault Systemes SolidWorks Corporation, Waltham, MA) and imported to the Objet printing set-up where the molds were then formed with VeroWhite printing material. The molds were then baked at 60°C for 4 hours to remove residue solvents, which can inhibit the curing of PDMS. This step is critical and can cause a few headaches if you don't properly post-bake to remove the inherent solvents. In the case that the solvents aren't fully removed, there will be an intermediary layer of pre-polymer between the cured PDMS and the 3-D printed mold. The presence of this layer is detrimental because it can impact the patterned features as well as produce a rough surface after cleaning which will render plasma oxidation bonding difficult.

An alternative method to prevent the formation of the prepolymer interface is to silanize the 3-D printed mold with TFOCS. To do this, place the 3-D mold in a desiccator along with 1-3 drops of TFOCS in a plastic petri dish. Turn on the vacuum pump and ensure the outlet is feeding into the fume hood. Allow the pump to run for 1-2 hours before flushing the reservoir with fresh air and opening up. Once this is completed, the molds are ready to use.

PDMS was mixed at a 10:1 base-to-curing agent ratio and poured into the 3D printed master molds before desiccation for 45 minutes. The PDMS-filled molds were then transferred to an oven at 60°C for at least 2 hours until fully cured. Last, the PDMS

layers were removed from the mold using an X-acto knife and excess PDMS was removed. Be sure not to actually use the X-acto knife on the mold itself as the knife will score the mold, which will then transfer to the PDMS. In many cases, this will lead to a local ridge which will then affect the bonding capabilities of that PDMS mold and all subsequent molds from that 3-D printed piece. Furthermore, the presence of scratches on the 3-D printed mold can cause the PDMS to stick in some places or lead to tearing during removal from the mold. As a result of this, I typically use the X-Acto knife to remove the 3-D printed mold and PDMS from the petri dish, then run the X-Acto knife along the outside edge of the 3-D printed mold to ease the removal of the PDMS.

Electronics integration

An LED circuit was designed featuring 3 or 5 LEDs (depending on the gripper configuration) with a peak wavelength of 465 nm and gull wing leads (Kingbright, City of Industry, CA) all arranged in series in a compact, circular pattern. The LEDs were soldered together and connected to a copper wire lead to which an external DC power supply was connected. Once the circuit was completed, it was placed centrally within uncured PDMS deposited in the 3D printed negative mold of the fluidic channels and culture wells.

Due to the challenges of soldering the very small LEDs without breaking the leads or damaging the LEDs themselves, I typically only integrated the LEDs into the device when I was actually doing direct testing of the LEDs. In retrospect, I would suggest using flux and perhaps even creating a board that can create series of 5 LEDs in a higher throughput fashion. My method for soldering the LEDs was very crude and involved a combination of adhesives and forceps to hold critical components in place

while I actually guided the solder and soldering iron with my hands. Obviously, the LEDs are diodes and thus must be arranged in the proper direction to function properly. You can tell the directionality of the gull-wing LEDs used in this project by examining the bottom of the LED.

Porous membrane fabrication

Through similar work by Jiao et al (*89, 140*), porous PDMS membranes were created via *in situ* reaction. The Sylgard 184 curing agent was mixed with sodium bicarbonate powder at a 1:1 mass ratio and mixed thoroughly before setting for 1 hour. The two materials were mixed once again before mixing with the Sylgard 184 base agent at a 1:5 mass ratio and desiccating for 20 minutes. The prepolymer-sodium bicarbonate mixture was then deposited on 120°C heat release tape at a thickness of 100 μm via thin film applicator. The PDMS was then cured at 60°C in an oven for at least 2 hours. The cured membranes were then submerged in a bath of 13M HCl plus Triton X-100 (100X dilution) for 1 hour before being thoroughly washed with water and allowed to dry in an oven at 60°C (2-4 hours).

This was also attempted using alternative methods to varying degrees of success. The primary challenges associated with these membranes are related to the transferability and the surface roughness. The issue of transferability is challenging due to the elastomeric properties of PDMS in combination with the material tackiness. These two characteristics in combination cause the membranes to wrinkle and fold upon themselves when they are sufficiently thin (~100um) in the absence of some sort of backing sacrificial layer.

Initial efforts with the PDMS-based membranes were attempted by spin coating at 1000

rpm on petri dishes, removing the membranes and etching in an HCl bath for 1-3 hours. Following this, the membranes were then rinsed with dH_2O and dried in the oven before binding to the device via plasma oxidation. However, this proved extremely challenging due to the aforementioned difficulties of transferring the membrane while avoiding folds and wrinkles. To address this, I tried to wet the membrane before placing it on another sacrificial layer, either a petri dish or aluminum foil, and then drying it in the oven for a few hours. When the membranes are wet, you can manipulate them relatively easily and remove the folds and wrinkles without worrying about tearing. In the case of the aluminum foil, removing the sacrificial layer after bonding the membrane to the device was difficult and often resulted in removing the portions of the membrane suspended over the patterned wells in the biolayer (the most critical portion of the membrane) so aluminum foil was scrapped.

The petri dishes are too wide to fit within out plasma oxidation chamber within the LeDuc Lab, so plasma oxidation for this attempt was performed in the Majidi lab's machine. However, removing the petri dish without tearing following plasma oxidation to the device proved a very challenging endeavor. To make this procedure a little easier, I started coating the petri dishes with gelatin by soaking the dishes in a 1% gelatin solution for 30 minutes at 80 °C on a hot plate. Once the gelatin dried, I would then spin coat the petri dishes with the PDMS-sodium bicarbonate pre-polymer mix at 1000rpm and then allow it to cure at 60 °C for 2-4 hours. The membranes were then bound to the device using plasma oxidation and then submerged in a heated water bath (40-50 °C) to dissolve the gelatin and release the membrane from the petri dish. Following this, the membrane would be etched in HCl while attached to the device. Unfortunately, the

deposition of the gelatin on the petri is not uniform and seemed to result in ridges and valleys that affected membrane structure. In addition to local mechanical weaknesses that resulted in tearing because of this, it was also difficult to create a tight seal between the membrane and the biolayer which lead to leaking during testing.

Heat release tape works very well for this reason, as the deposition surface is very flat and uniform in comparison. I first used 80 °C release tape which worked much better than the gelatin system and made the fabrication much easier. However, after repeated testing with the following steps, I found that 120 °C heat release tape worked more effectively for a few reasons. For one, the 120 °C tape releases more easily at its listed temperature. Secondly, the 120 °C tape turns from a bright blue to an opaque sky blue when heat activated which provides a useful visual cue. Conversely, the 80 °C tape is a creamy beige color and its transition is much less noticeable.

For initial testing with the heat-release tape, I would cut the heat release tape out into circles roughly the size of petri dishes and spin coat the PDMS-sodium bicarbonate prepolymer on it at 1000 rpm. However, this wouldn't always result in the most uniform deposition as the circular cut-outs would sometimes warp out-of-plane due to the cutting.

To address this, I then began using a thin-film applicator to deposit the prepolymer, typically using a thickness of around 100-150 µm. The width of the heat release tape sheets is slight wider than the clearance of the thin-film applicator provided by the Majidi lab, so I would cut roughly a quarter inch off the edge of the tape sheet so the applicator could pass over it cleanly. I secured the sheet to an aluminum plate long and wide enough to allow for easy movement of the thin-film applicator while also ensuring a flat

surface. I would then use calipers to measure the thickness of the heat release tape after removing the protective coating on the deposition side. This thickness, which includes the heat release tape as well as an additional backing protective coating, would measure roughly 250 µm. I would then set the height of the thin film applicator to be equal to my desired height plus the measured height of the heat-release tape.

Once the heat-release tape was position and the thin film applicator was set to the appropriate height, I would make 2-3 test passes to ensure that the clearance was correct and the path was free of obstacles or debris. The PDMS-sodium bicarbonate pre-polymer was then poured over the top edge of the heat-release tape sheet (roughly 10 mL spread across the width of the sheet). The thin-film applicator was then dragged along the length of the sheet to deposit a uniform pre-polymer layer. The heat-release tape sheet was then carefully removed from the aluminum plate and placed in the oven to cure at 60 °C overnight.

Due to the embedded sodium bicarbonate particles within the prepolymer mixture, the resulting surface after curing is often rough. This surface roughness causes problems during plasma oxidation bonding as it can prevent the formation of a tight seal and lead to leaks. To offset this, I performed an additional thin-film application step using pure PDMS pre-polymer and an added 5-10 µm of clearance. This produces a smoother top coat while still not creating a thick layer of PDMS lacking sodium bicarbonate such that through-pores are unable to form. After deposition, the membranes are placed in the oven once again at 60 °C for 2 hours.

Once the membranes are fully cured on the heat-release tape, I perform a rough-cut of the device outline. This is done for two reasons – the first is to maximize the amount of

devices I can create from a single sheet of PDMS-sodium bicarbonate membranes and the second is to allow the membranes to fit into the plasma oxidation chamber more easily. I typically lay a pre-cured PDMS biolayer on the membrane sheet like a stencil and cut out the membrane about 0.5 cm from the biolayer edges. This gives additional freedom in combining the membrane and biolayer during the following plasma oxidations steps when the two components must be aligned within about 30 seconds before the bonding efficiency decreases.

Lastly, the etching step for the PDMS membranes was performed once the membrane was bonded to the device. This is due to the difficulties highlighted earlier related to adhering a thin PDMS membrane to another substrate without a sacrificial as well as the requirement for opposing faces of the membrane to be uninhibited during the etching process to allow for through pores to form.

Device assembly

The device was comprised of two main layers, one containing the biological components and the other housing the electronic components. First, 25g of PDMS prepolymer was poured into a negative mold possessing the features of the fluidic channels and bacterial growth wells. A series of blue wavelength LEDs were then placed in the center of the PDMS layer and allowed to partially cure on a hot plate. Once partially cured (25 mins @ 70°C on a hot plate), a fully cured EcoFlex layer possessing pneumatic channels (achieved through 3D printed negative mold) was placed on top of the PDMS layer and allowed to adhere and seal off the interior channels. Following this curing process, the PDMS-EcoFlex device was carefully removed from the fluidic channel mold and the biolayer interface was then sealed off

with a microfilter membrane (PDMS-NaHCO$_3$, polycarbonate or polyethersulfone) via plasma oxidation (Figure 2.6).

Polycarbonate track etched (PCTE) and polyethersulfone (PES) membranes were purchased from Sterlitech with pore sizes of 0.2 μm (PCTE and PES) and 0.4 μm (PCTE). PES membranes were adhered to the PDMS biolayer component via an APTES pretreatment process outlined by Aran et al. (*89*) while the PCTE membranes were adhered using a combination of an APTES approach and sealing the membrane edges using PDMS prepolymer before curing to prevent delamination. However, other members of the LeDuc lab have suggested that an additional plasma oxidation step within the protocol laid out by Aran et al. improves the bonding. As such, the protocol is as follows. First, the PES or PCTE membranes are plasma oxidized for 1 minute. They are then placed into a heated bath of 6% APTES at 80 °C. The membranes must be fully wetted and allowed to sit in the bath for 30 minutes. They are then removed from the bath, dried with disposable wipes and then plasma oxidized for a further minute alongside the partnering PDMS substrate. The two components are then removed from the chamber and carefully placed into contact with one another to prevent the formation of wrinkles. Following that, the two components are sandwiched between two flat, black plastic blocks and clamped together before being put in the oven to set the bond at 60 °C for at least two hours.

In the case of the PDMS-sodium bicarbonate membrane, the membranes are bound to the biolayer-Pneu-net composite via plasma oxidation and put in the oven to set the cure for at least 2 hours. Once the membrane is set, the device is then placed on a hot plate set to 125 °C. The heat-release tap then activates within 1-2 minutes. Ensure solid

contact between the tape and the hot plate to guarantee that the tape is fully activated. Once fully activated, the tape should visibly change color from a translucent bright blue to an opaque sky blue. This transition should be followed by a gentle removal to ensure the membrane remains intact across its entirety.

After separation from the heat release tape, the adherent membrane must be etched in an HCl bath. As a surfactant, add 1-3 drops of Triton X-100 to facilitate the etching process. After 1-3 hours, the pores should have sufficiently formed across the membrane. Pockets of air should be noticeable within the bath and device, suggestive of the CO_2 released as a product of the *in situ* reaction. Using extreme caution and proper PPE, rinse the devices thoroughly with dH_2O before placing in the oven to dry for 1-2 hours at 60 °C.

Permeability

Permeability of the membrane to IPTG was measured using multiple methods to verify molecular transport through the transmembrane pores. As an initial validation, membranes were suspended across microchannels (500µm width), which were formed as PDMS negative molds from 3D printed masters, and sealed using plasma oxidation. Following sterilization with 70% ethanol and UV radiation, fluorescent beads (1µm diameter) in LB media were introduced into the upper channel while sterile LB media was flowed into the lower channel, separated by the membrane. The two fluids were left to sit statically in the channels for 2 hours before fluorescent measurements using a plate reader were performed and compared with initial fluorescent readings of each solution.

For further validation of the permeability, chemo-sensing bacteria were introduced into

sealed biolayers with PDMS-sodium bicarbonate, PCTE and PES membranes. The sealed biolayers were then placed in aqueous baths within petri dishes which featured 100mM IPTG in solution. The petri dishes were placed on a shaker table in an incubator at 37 °C for two hours before imaging using a laser scanner. The laser scanner imaged for GFP across the entire device to detect levels of gene expression due to the permeation of the IPTG into the device through the membranes.

The results for this method in Chapter 3 show disparity between the PDMS, PES and PCTE methods with regards to the fluorescence expression. Though we did not quantify the actual permeation rates of these membranes using traditional cross flow assays, there are a number of possible explanations for these disparities. In the case of the PDMS-sodium bicarbonate membranes, the pores are formed using an *in situ* reaction and according to the originators of the technique, range between 15-500 nm. This dispersity in pore sizes could limit permeation if those pore sizes are predominantly on the lower end of that range, which would be smaller in comparison to the 200 nm pores found in the off the shelf PES and PCTE membranes. For the disparity between the PES and PCTE membranes, the sources of discrepancy most likely like in the material or mechanical properties. PES is a glassy membrane that can be difficult to fully seal against a relativity rough PDMS surface molded from a 3-D printed template and it is difficult to ascertain whether or not there was additional leaking. There are also additional coatings on the two materials to improve hydrophilicity, which would impact the permeation rates. Future work could be directed towards characterizing these membranes and their performance in relation to this device. The largest consideration for us was to ensure small molecules (i.e. IPTG) could permeate in while single cell

organisms (i.e. *E. coli*) would be contained within.

Stereomicroscopy

A digital charge-coupled device (CCD) camera (The Imaging Source Europe GmbH) mounted on a stereomicroscope (SZX12, Olympus Corp., Waltham, MA) was used to perform wide-field imaging of the device to create a composite view of the LED excitation of GFP-producing cells housed within the PDMS layers. Imaging was performed with 1X magnification with 18 V of power supplied to the 5 gull wing LEDs, while the sealed bio-layer was positioned on an actuating stage and moved accordingly during a time series capture with 3 second intervals (Figure 2.7).

The need for a stereomicroscope lay in the fact that the epifluorescent microscope in the LeDuc Lab features 5X as its lowest magnification objective. In order to create a composite image of the entire device under LED excitation, it would require more than 300 images to be collected, indexed and stitched together. The LED excitation imaging could not be performed using a laser scanner or traditional organism-level fluorescence imaging tools because of the presence of metallic materials in the LEDs and the wires.

The images collected on the stereo microscope appeared to have a gradient of noise from left to right which manifested itself with higher average pixel intensities on the left side of the image than the right. Though I accounted for this in my calculations by measuring consistently in the same regions across images, it is something that could be addressed in future experiments using this method (Figure 2.8). In retrospect, I believe the primary cause for this could be in the misalignment of the light source or condenser of the microscope itself. Because I was not familiar with that particular microscope, I wasn't able to take lengths to properly calibrate it before use. A simple secondary

approach that one could use would be to take a "blank" image without any fluorophore sources and use that image as a subtraction template to remove the appropriate noise from all images.

Pneumatic actuation

Deflection of the device through pneumatic action within the EcoFlex layer was measured using open source motion tracking software (Tracker). Pressure was increased within the channel manually with a syringe pump and pressure levels were monitored using a piezoelectric pressure sensor (Honeywell, Morristown, NJ) interfaced with a microcontroller and MATLAB (Mathworks, Natick, MA). Pressure was increased in 0.5 psi increments from 0-5 psig. Positions were recorded along the pneumatic appendage in 0.5cm increments for each pressure step (Figure 2.9).

I initially attempted to use house air for this testing however it was challenging to regulate the pressure at such low intervals from such a high pressure source. Often the pressure would go well beyond the 5 psi goal and the device would rupture. The initial design also featured interconnected PneuNet channels for all 5 fingers of the device. This became problematic as it introduced a much larger area in which imperfections could occur that would lead to ultimate failure for the whole device. To make testing easier and alleviate this problem, I redesigned the PneuNet channels to be 5 independent channels rather than 1 interconnected series. This allowed me to test, at least 4 out of 5 fingers of the device pending proper fabrication strategies. It is challenging to produce a fully functioning device due to the formation of air pockets during the partial cure step outlined previously, as these air pockets at the biolayer-PneuNet interface serve as local weaknesses where rupture or leaks can occur.

Hydrogel Preparation

Gelatin molds were prepared by mixing 15% w/v of gelatin from porcine skin (Sigma-Aldrich, St. Louis, MO) and heated to 80°C on a hot plate. Test samples were mixed with 1μM IPTG (Sigma-Aldrich) before being left to cool in the plastic mold. After cooling, cover the molds with parafilm or aluminum foil and store at 4 °C for 1-2 weeks. If left uncovered, the hydrogels will dehydrate or will become contaminated. Mold and other contaminants can grow on gelatin very easily so it is important to maintain sterile practice during these steps.

Hydrogel sensing test

Overnight cultures of bacteria were prepared in 3mL volumes of LB with 1 μL of 50 μg/mL stock ampicillin before placing on a shaker table at 37 °C for 16 hours. The overnight cultures were then diluted 100X into fresh media and antibiotics, and allowed to grow on the incubated shaker table for 4 hours. The bacteria were then extracted from the test tube and injected into the fluidic reservoirs of two devices. The remaining bacteria were then split into 1 mL volumes in fresh test tubes, one of which was induced with IPTG (1mM).

The two devices were placed in incubators at 30°C. One was brought into contact with an IPTG infused gelatin mold submerged in LB while the other was brought into contact with a standard gelatin mold submerged in LB. The pneu-net channels of the devices were activated in parallel using syringes and tubing fixed within a quick-clamp to insure constant pressure. The devices were left in place for 4 hours before extraction via syringe. The samples were then measured using an absorbance and fluorescence plate

reader (Tecan, Mannëdorf, Switzerland) along with the samples from the test tubes.

Supplemental discussion

We were able to analyze the response of genetically altered synthetic circuits within an integrated soft robotic platform. We first measured the growth and optical properties of the bacteria within the fluidic channels of the PDMS layer. We designed PDMS bio-layers with different geometries to produce desired multi-phase flow properties for manipulating biofluids in the device and to achieve reproducible growth patterns. First, the growth rates of bacteria were measured in four distinct well geometries (circular, square, rhombic, and ellipsoidal) at constant basal surface areas and volumes. This analysis was performed by creating PDMS chambers from 3D printed negative molds possessing the well and channel features. These PDMS chambers were sealed with thin (1 mm) PDMS layers via plasma oxidation and sterilized before being filled with overnight bacteria culture diluted 10µL per 1 mL of M9 media. The wells were placed on an incubated shaker and measured for optical density at 2 hour intervals over an 8 hour period.

The growth patterns related to optical performance in each one of these devices were also evaluated. A culture well geometry that produces consistent bacterial growth and subsequent fluorescent expression across the base of the well is desired for control of the device. To evaluate these properties, bacteria cultures in the exponential growth phase were stimulated to produce GFP through the introduction of IPTG and were introduced into PDMS biolayers featuring the same four shapes and allowed to growth on an incubated shaker for 4 hours. The biolayers were then removed from the shaker and imaged for GFP in a gel imager as well as on an epifluorescence microscope.

From this result, surface plots were constructed showing the relative intensities while viewing from the z direction and variance between the shapes was determined. From these data, the circular wells produced the most uniform expression of GFP across the base of the wells.

To enable chemical communication between the device and environment, we used a nano-porous PDMS-sodium bicarbonate layer as described previously (*88*), which possesses 15-500 nm pore sizes that are small enough to retain *E. coli* while allowing the perfusion of chemical inducers. To further validate the transport of nano-scale objects through the PDMS-sodium bicarbonate membrane using perfusion tests of fluorescent beads (5nm) and Cy5 dye, distilled water and fluorescent markers diluted in media were introduced into channels and culture wells separated by the membrane for 2 hours. Fluid from the top and bottom fluidic networks was then measured for fluorescence using a plate reader. These data show that perfusion is occurring through the membrane for small particles, and as particle size increases, the corresponding rate of diffusion decreases.

Next, the membrane-sealed layer was submerged in a bath of 30 ml LB media with 1 mM IPTG. After submersion for 4 hours, the sealed biolayers were removed from the bath, rinsed, and then imaged for GFP expression using a gel imager. Fluorescence expression of GFP in induced regions of bio-layer wells submerged in an environment with IPTG showed a two-fold increase in GFP expression over those submerged in standard growth media lacking the chemical stimulus. This result indicates successful perfusion of IPTG from the outside environment through the sealing porous membrane into the culture wells as well as retention of cells within the wells.

We then integrated the biolayer with existing flexible robotic actuation systems and embedded LED circuits. The integration process combined a series of curing and plasma oxidation techniques. First, PDMS was poured into a negative mold possessing the features of the fluidic channels and bacterial growth wells. A series of 5 blue wavelength LEDs was then placed in the center of the PDMS layer and allowed to partially cure on a hot plate. Once partially cured (35 mins @ 80C on a hot plate), a fully cured EcoFlex layer possessing pneumatic channels (achieved through 3D printed negative mold) was placed atop the PDMS layer and allowed to adhere and seal off the interior airways. Following this curing process, the PDMS-EcoFlex device was carefully removed from the fluidic channel mold and the biolayer interface was then sealed off with a PDMS membrane.

To evaluate the mechanical performance of the device, we measured deflection of the device under pneumatic actuation using a syringe pump connected to the pneumatic channels within the EcoFlex 0030 layer via polyeurythane tubing. An increase of internal pressure within the patterned EcoFlex layer caused an expansion of the internal air compartments, resulting in a preferential bending due to the discrepancy in mechanical stiffness between the PDMS-EcoFlex interface and the free edge of the EcoFlex. To improve stability and consistency, a 3D printed base was designed and implemented for testing purposes. Pressure within the line was measured using a pressure transducer and administered within the range of 0-3psig. Deflection was quantified using video tracking software with point displacement measurements at varying pressures to determine the overall effect of the microfluidic channels on the mechanical performance of the device. The presence of the fluidic channels and the centrally located LED circuit

did not inhibit the soft robotic functionality of the device. Additionally, the fluorescence within the cells in the device remained the same after pneumatic actuation, indicating that the integration of these individual components did not affect functionality.

We analyzed the fluorescent response of the cells in the presence of IPTG embedded in a controlled functioning soft robotic system. Excitation of GFP-producing cells within the device by the embedded LED circuit was observed using stereomicroscopy and a combination of fluorescent filters. A 495 nm long-pass filter was utilized to minimize the signal from the blue LEDs, which produce an observable signal in the green spectrum (485-565 nm). In conjunction with the long-pass filter was a green filter to further reduce noise. Images were taken with a 1X objective in a time series on a moveable stage to allow for wide-field data collection at all areas of the device. The subsequent images were then integrated together into a macro-image to demonstrate the overall fluorescent signal appearance as a result of the LED excitation (Figure 2.8A). Intensities within each well were measured by creating a ratio of a random area sampling of pixel intensities within the wells to intensities within the PDMS layer outside of the well (Figure 2.8B). This approach allowed us to normalize images to background noise and compare between controls. Fluorescence imaging of LED excitation was performed with genetically modified cells induced with IPTG as well as uninduced genetically modified cells and unmodified MG1655 *E. coli*. The relative fluorescent intensities were compared, showing that the induced cells had a fluorescent signal approximately 4 times greater than MG1655 cells and uninduced modified cells. The signal acquired using stereomicroscopy was compared with traditional epifluorescent imaging, which shows that the more conventional epifluorescence was similar to the embedded LED

system.

We then demonstrated the capabilities of the integrated device by engaging the pneumatic gripper in the presence of IPTG-infused hydrogels. A 10% w/v mixture of gelatin in dH$_2$O was created at 80°C and then poured into a rounded 3D mold before being allowed to cool to room temperature. Once cooled, the mold was submerged in aqueous solution and placed in an incubator at 30 °C before the device was brought into proximity with fresh cultures of *E. coli* in liquid growth media filling the channels and wells. After appropriately positioned, the pneumatic arms were engaged with 2 psig to initiate contact with the submerged hydrogel. This contact was maintained for 4 hours before evaluating the fluorescent response of the housed bacteria with epifluorescence microscopy. This produced a roughly 3 fold increase in the *gfp* expression compared to cells contained within the device in contact with standard hydrogels lacking the chemical inducer.

Lastly, we introduced a photo-responsive bacterial cell line to the device set-up. Through activation of the embedded blue LED circuit, the genetic circuit could be repressed and the subsequent synthesis of GFP inhibited. Repression of GFP synthesis within the device was observed over a period of 4 hours with bacterial cultures in logarithmic growth and decreased normalized fluorescence expression. This result is comparable to the controls performed in standard testing conditions, which yield decreases expression by roughly 50%.

Supplemental Figures
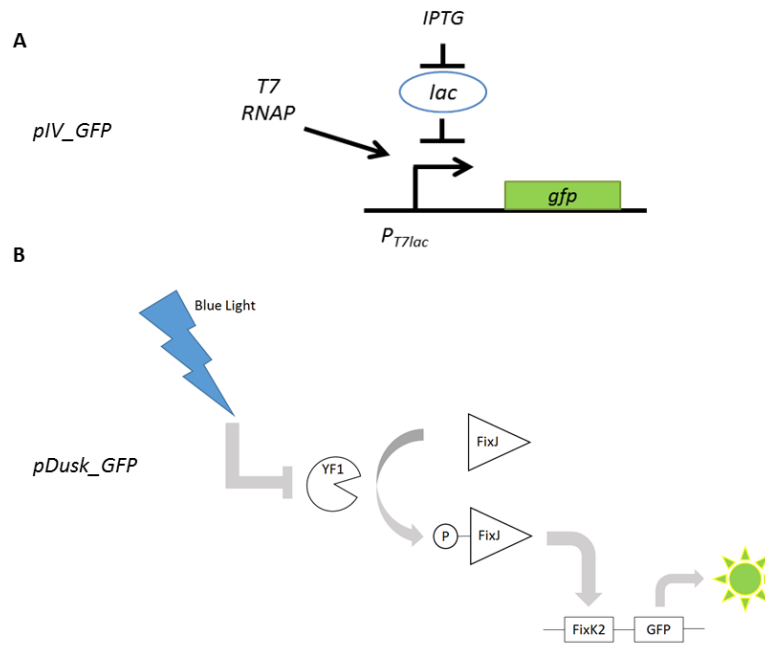
Figure 2.1 Schematic representation of genetic modules. (A) The chemo-sensitive E. coli genetic module features a T7 promoter and a lac repressor, which inhibits the synthesis of green fluorescent protein (GFP) through the gfp gene in the absence of IPTG. (B) The genetic modules pDusk_GFP, pDusk_v37_GFP and pDusk_v38_GFP all exhibit opto-sensitive behavior. The plasmids pDusk_GFP, pDusk_v37_GFP, and pDusk_v38_GFP have the same genetic structure except for the sequence of their ribosome binding sites. In the absence of blue light, YF1 phosphorylates FixJ. Phosphorylated FixJ activates transcription at the FixK2 promoter, allowing for the expression of GFP. In the presence of blue light, the kinase activity of YF1 is blocked, preventing the phosphorylation of FixJ and the subsequent activation of GFP expression. Lines capped with arrows represent activation or expression, and lines capped with bars indicate repression.
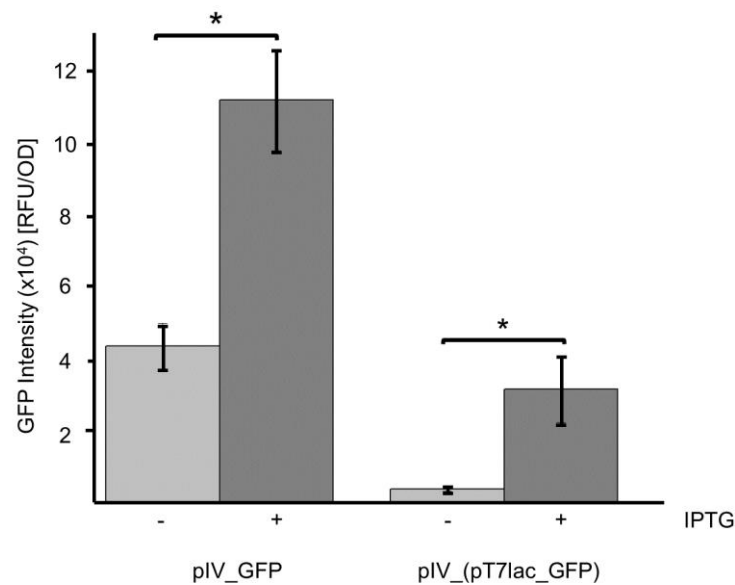
Figure 2.2 Fluorescence measurements of pT7 strains after IPTG induction and incubation for 4 hours. GFP intensity was measured in two chemo-sensitive strains, named pIV_GFP and pIV_(pt7lac_GFP), 4 hours after introduction of IPTG. The cells were grown overnight in LB media (2 mL volumes) supplemented with 50 µg/mL ampicillin after inoculation using bacterial colonies from LB-agar plates. The overnight cultures were then diluted 1:100 in fresh LB media and 50 µg/mL ampicillin, and placed on an incubated shaker table for 4 hours to reach the logarithmic growth phase. IPTG was introduced at 1 µM concentrations into the test tubes and allowed to induce GFP synthesis for 4 hours. After 4 hours, the samples were measured using a Tecan Safire II fluorescence and absorbance plate reader for fluorescence at 480 nm/510 nm excitation/emission wavelengths and for absorbance at 600 nm (optical density). The fluorescence values were normalized by the corresponding optical density measurements. The data represent 6 replicates and SEM (*p<0.05).
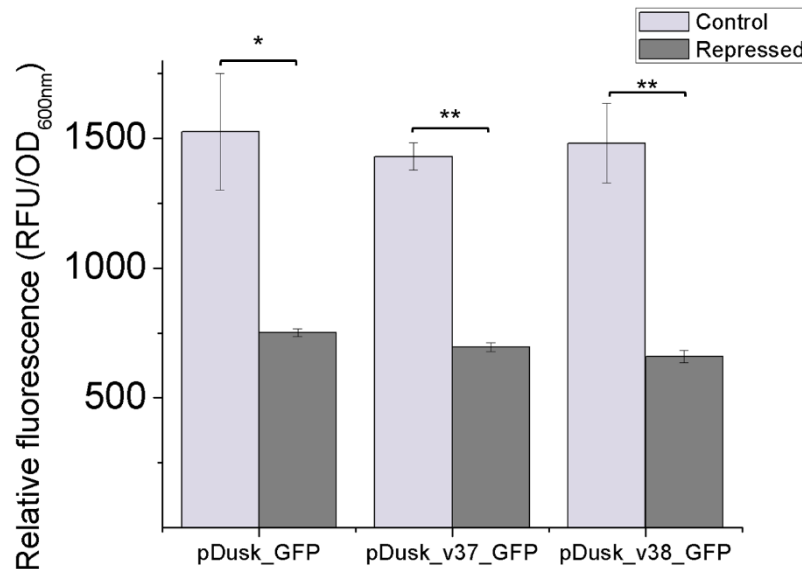
Figure 2.3 Repression of gene expression in pDusk strains using blue light. GFP intensity was measured in three opto-sensitive strains, named pDusk_GFP, pDusk_v37_GFP and pDusk_v38_GFP, 4 hours after repression due to blue LEDs (λ_{peak} = 465 nm). The cells were grown overnight in LB media (2 mL volumes) and 50 µg/mL kanamycin after inoculation using bacterial colonies from LB-agar plates. The overnight cultures were then diluted 1:100 in fresh LB media and 50 µg/mL kanamycin and placed on an incubated, dark shaker table for 4 hours to reach the logarithmic growth phase. LEDs were then introduced into the incubator near the test tubes to repress GFP production (control test tubes were shielded with aluminum foil). After 4 hours, the samples were measured using a Tecan Safire II fluorescence and absorbance plate reader for fluorescence at 480 nm/510 nm excitation/emission wavelengths and for absorbance at 600 nm (optical density). The fluorescence values were normalized by the corresponding optical density measurements. The data represent six replicates and SEM; (*p<0.05).
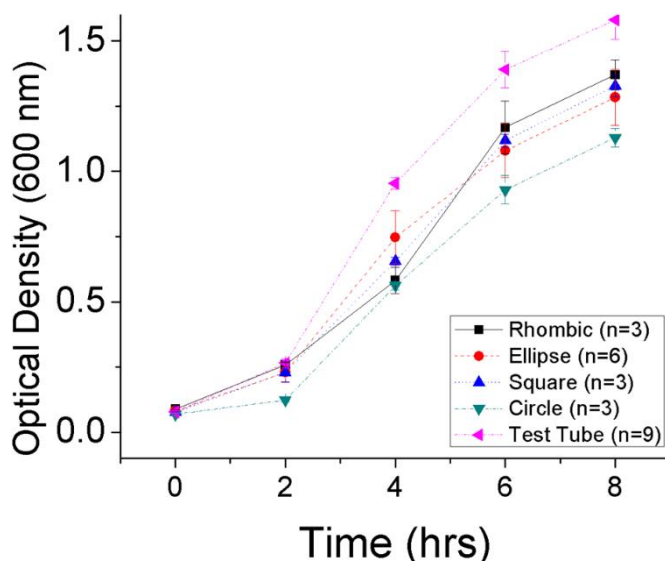
Figure 2.4 Growth curves of pT7 strains in varying well shapes over 8 hours. To establish growth behavior of the bacteria within PDMS wells of varying geometries, four cross sections (circular, ellipsoidal, square and rhombic) of constant volume (300 µL) were developed for testing. PDMS molds featuring these patterned wells were filled with freshly diluted overnight cultures of chemo-sensitive bacteria and allowed to grow on an incubated shaker table at 37 °C. Optical density measurements were recorded at two hours increments using an electrospectrophotometer. Data represent three to six replicates and SEM.
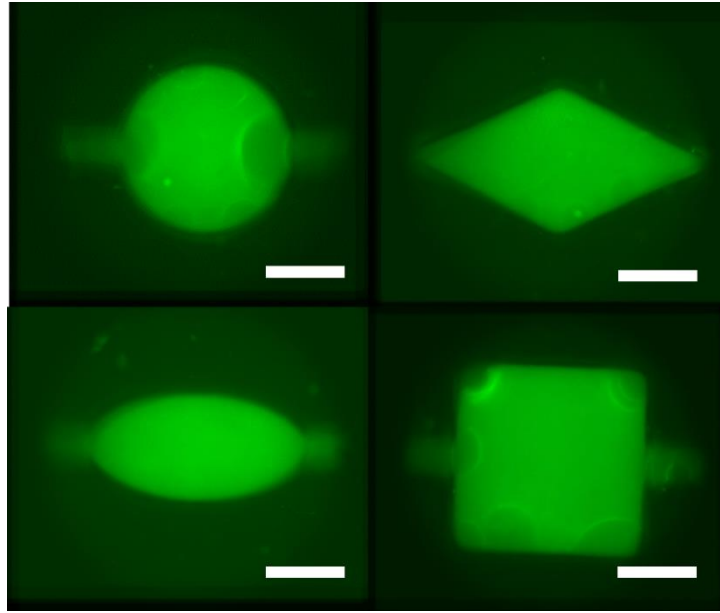
Figure 2.5 Fluorescence images of induced pT7 strains in varying well geometries. Induced chemo-sensitive bacteria were grown in the four well cross-sections and imaged using an epifluorescent microscope. Shown are aggregate images of n=10 wells, with air pocket formation shown in some wells, most notably in the square wells. Scale bars = 1 mm.
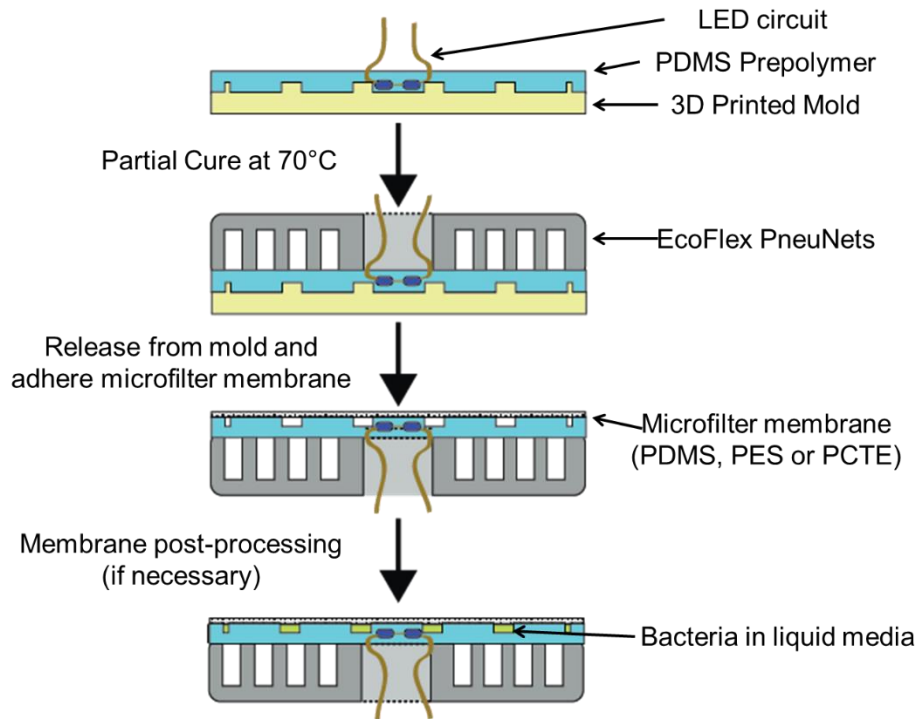
Figure 2.6 Schematic of the device fabrication. The device is fabricated using a combination of 3-D printed molds and a series of curing, partial curing and plasma oxidation steps. First, the biolayer is created by pouring PDMS prepolymer into a 3-D printed mold featuring the desired well design. The LED circuit is then set in place and the layer is partially cured on a hot plate at 70 °C for 20 minutes. Following this, an EcoFlex layer featuring the Pneu-Net channels (formed from a separate 3-D printed mold) is placed over the partially cured PDMS, which is then allowed to fully cure on the hot plate. Once the two layers are cured together, they are removed from the initial 3-D printed mold and cleaned with adhesive tape. Following this, the desired membrane is sealed using either direct plasma oxidation (PDMS-NaHCO3 membrane), or APTES pre-treatment followed by plasma oxidation (PES, PCTE) and necessary baking or etching.
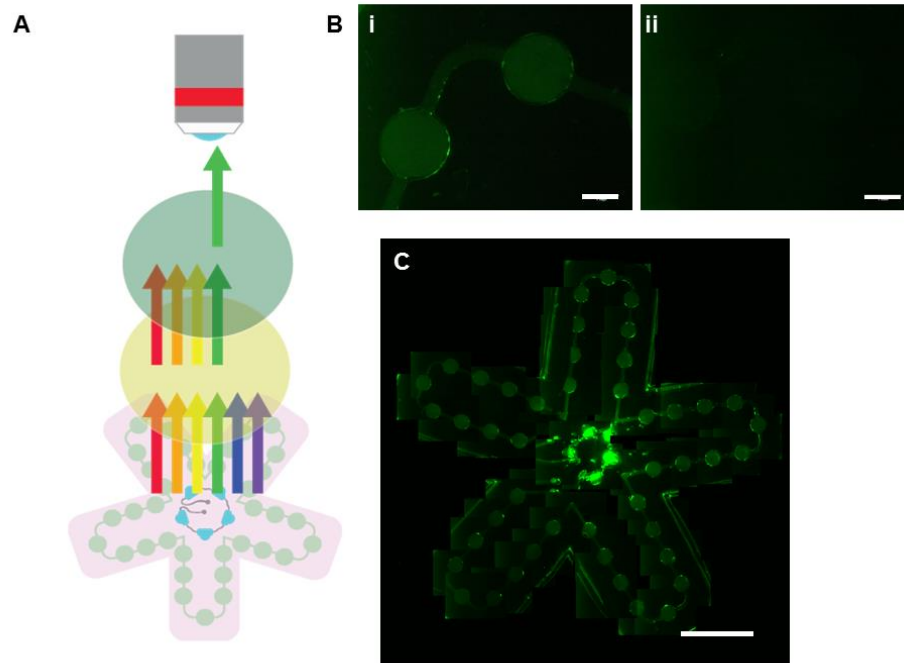
Figure 2.7 Wide-field imaging of induced GFP synthesis within the device.

(A) Wide-field imaging of the device was conducted using a stereomicroscope and a series of filters designed to permit only green fluorescence due to LED excitation.

(B) Imaging was performed on the device possessing pIV_GFP after IPTG induction (i) and the same bacteria without induction (ii) as well as MG1655 bacteria (not shown); Scale bar = 1mm.

(C) The wide field images were stitched together using Adobe Photoshop after applying green colorization in ImageJ. Scale bar = 10 mm.

$$RFI = \frac{A_{avg}}{B_{avg}}$$
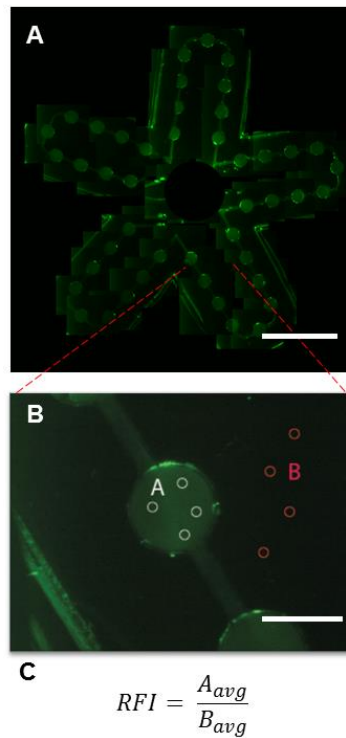
Figure 2.8 Method used to determine relative fluorescent intensities. (A) Individual images taken through wide-field stereomicroscopy were analyzed individually to determine the efficacy of excitation by the LED circuit. (B) To analyze the relative fluorescence intensity of each image, multiple regions were randomly selected inside and outside of the wells to normalize for background noise; scale bar = 10 mm. (C) The representative relative fluorescence intensity was determined by dividing the average pixel intensity of the regions inside the wells by the average values in the surrounding PDMS. Scale bar = 2 mm.
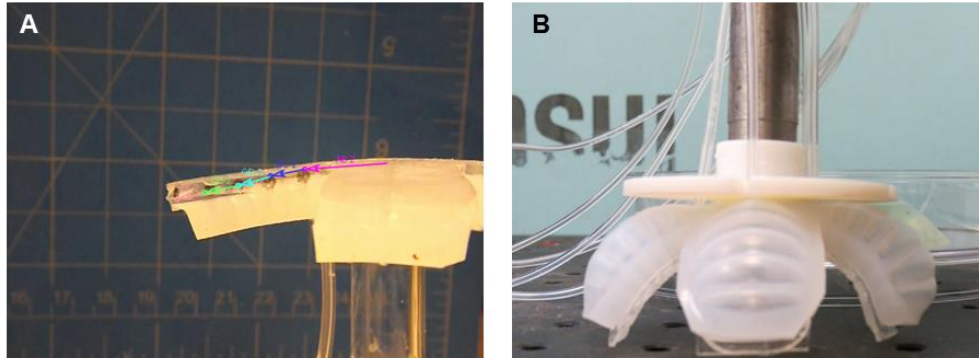
Figure 2.9 Tracking software used to determine deflections in the actuated device. Deflection due to Pneu-Net actuation was measured using video recording and piezoelectric pressure sensors. Pressure was manually increased in 0.5 psig increments using live tracking of the pressure readings and correlated with deflections from video recording. (A) The deflections were acquired by analyzing the recorded video using open-source Tracker software (Open Source Physics). (B) The gripper in its fully actuated state at roughly 5 psig.

Magnetoliposome preparation and characterization

Liposome formation

Liposomes are formed with a combination of DPPC and biotinylated phosphatidylethanolamine (bioPE) lipids as well as cholesterol (Chol) (Avanti Polar Lipids). The lipids and cholesterol were stored at -20°C in a chloroform solution at a concentration of 4 mg/mL. To begin the liposome synthesis, mixtures of 80:5:20 µL DPPC:bioPE:Chol were introduced into 10mL glass beakers before the addition of 50µL of methanol. The beakers were then vortexed for 30 seconds to ensure homogenous mixing of the contents and then covered with parafilm. Using a sterile needle, the parafilm covers were vented with three holes and the beakers were placed under vacuum in a desiccator for 8 hours.

After successful dehydration of the lipid mixture and the resulting formation of lipid bilayer films at the base of the beakers, the lipids were resuspended in 1mL of aqueous media with quenched calcein (0.05 g/mL) and sucrose (0.05 g/mL). The aqueous solution was heated to 45°C beforehand to surpass the gel-to-liquid transition temperature of DPPC lipids, which is reported to be 41°C. This was done to ensure fluid lipids which are important for effective liposome formation. Following the introduction of the solution, the mixtures were vortexed for 30 seconds each to suspend the entire lipid bilayer film. Fully agitated mixtures were then placed on a heating block (45°C) overnight and covered with parafilm to allow the liposome mixture to reach an equilibrium state. This method is known as thin-film hydration and is one of many methods used for synthesizing liposomes.

The liposome mixture was then aliquoted in 100µL volumes into sterile microcentrifuge tubes and covered with perforarted parafilm. The microcentrifuge tubes were placed in a -80°C freezer for 20 minutes to allow the solutions to freeze. Once the mixtures were frozen, they were quickly transported to a lyophilizer and allowed to freeze-dry for 12-16 hours. The lyophilization was performed to increase the long-term stability of the liposomes.

The freeze-dried lipids were then resuspended with 150mL of deionized water or 5% sucrose in PBS and mixed via micropipette. The liposomes were then pelleted using a centrifuge at 2000 rpm for 15 minutes before removing the excess liquid and resuspending in fresh deionized water. This was done to remove the extra-liposomal calcein and was repeated 5 times to achieve a significant reduction in calcein signal outside of the liposomes. Depending on the liposome composition, the vesicles will pellet better in different solutions. This is dependent on the osmolality of the liposomes and unfortunately, we do not possess an osmometer to test this value directly. As such, a combination of literature searching and trial-and-error was used to determine the ideal solutions for a given liposome design. For the case of DPPC liposomes, the best solution in which to centrifuge is 5% sucrose. Conversely, if you are using POPC-based liposomes, ice-cold water or PBS are typically most effective. It is important in both cases to ensure that the solution is near or below the phase transition temperature of the primary lipid. This allows the vesicles to pellet without rupture or leaking. After centrifuging, there will be an opaque, white pellet in the bottom of the centrifuge, similar to what one would see when pelleting mammalian cells for culture.

Substrate binding preparation

As an initial test, glass sides were coated with heparin, upon which avidin was then seeded to create a biotin-binding functionalized surface. Liposomes possessing streptavidin-coated ferromagnetic beads were introduced via micropipette to the functionalized surface. The system was allowed to equilibrate for 1 hour at 37°C to facilitate binding of the free bioPE lipid heads to the heparin-avidin conjugates. Once liposomes were bound, the vesicles were imaged using epifluorescence microscopy and subjected to external magnetic force by the Helmholtz coil arrangement.

Introduction of beads: pre-mixing

Following the dilution of the extra-liposomal fluorescence, red-fluorescent ferromagnetic streptavidin-coated 200nm beads were added to the liposomal mixture to bind with the biotinylated phosphatidylethanolamine lipids. This was done after centrifugation to maintain integrity of the liposomes in light of the difference in density between the beads and the lipids. The beads were purchased in a stock solution at a concentration of 1mg/mL, of which 15µL were then diluted in 60µL of deionized water. From this diluted solution, 3µL were added to each of the microcentrifuge tubes containing liposome mixtures to bind with the biotinylated PE lipid heads.

Beads are sonicated in aqueous solution for 1 hour at 37 °C before introduction into the liposome mixture. The primary motivation for this is to break apart the aggregations of beads that can occur while in storage. Furthermore, after introducing the beads into the liposome mixture, the solution is placed on an incubated rotary shaker table at 37 °C and low frequency (0.5-1 Hz) for 1-3 hours. This allows the beads and liposomes to constantly mix and bind. One of the major drawbacks of this approach is that it allows for beads to bind to multiple liposomes. Each steptavidin molecule features 4 binding

locations for biotin to bind in combination with the fact that each bead is coated with many streptavidin molecules. The end result is the formation of bead-liposome aggregates, which are not ideal for our purposes. Another drawback of this approach is that there is no control over where the beads bind on the liposomes themselves. Thus it is possible to have beads on opposite sides of the liposome, which is not ideal for magnetic tensile cytometry when we wish to put the liposomes in a state of tension.

Introduction of beads: laminar flow deposition

In order to achieve antagonism between an anchor point and the magnetic beads, a microfluidic bead-binding approach was employed. To accomplish this, microfluidic channels were created using traditional soft lithography techniques. Two chip designs were used, one with a 250 μm channel width and the second with a 500 μm width, both with channel heights of roughly 200 μm. The PDMS channels created from the photoresist-patterned silicon wafers were sealed with thin cover glass to enable imaging under 63X objectives. Said cover glass slide was functionalized with APTES as described in the Substrate Binding Preparation step and coated with avidin protein via EDC reaction. Following the avidin coating, the channel was rinsed with PBS two times. Next the liposomes were loaded into a syringe and placed in syringe pump before being introduced into the channel at a flow rate of 200 μL/hr. Once the length of the channel has been filled with liposomes, the pump is stopped and the liposomes are allowed to settled to the seeded avidin proteins at the bottom of the channel. A syringe pump is employed rather than manual injection as low flow rates are difficult to achieve by hand and high shear rates can result in rupture of the vesicles.

After the liposomes are seeded on the protein-coated cover glass slide at the bottom of the channel, the magnetic beads are then introduced in the same fashion. The beads are loaded into a syringe and introduced into the channels at a flow rate of 30 µL/hour. This lowered rate of introduction is used as a precautionary method to ensure the liposomes do not detach or rupture due to the bead flow. Using this approach, beads are able to bind to the seeded liposome, though further optimization is required with regards to the concentrations and flow rates to improve the ratio of beads per liposome.

Alternative liposome synthesis approaches and their implications

There are a number of different tweaks one can make to the general thin-film hydration protocol which I have used to synthesize liposomes. First, there are a wide variety of lipids one can interchange with the structural phospholipids used (DPPC or POPC) as well as the functional lipids (biotinylated PE lipids) used in this work. In the case of the structural lipids, the important characteristics to consider are the phase transition temperature of the lipid and the critical packing parameter. These properties will determine the behavior of the lipid bilayer membrane at a given temperature and the mode of self-assembly respectively. I briefly experimented with DOPC lipids as my structural membranes but the majority of my work features DPPC and POPC based liposomes. The important difference between these two is the phase transition temperature (41 and -2 °C, respectively). This renders POPC liposomes much more fragile at room temperature, with the lipid bilayer membrane behaving more like a liquid than a gel. This property manifests itself if you try to centrifuge the liposomes without chilling the solution beforehand or if your spin them down at too high of a speed. In these cases, the vesicles can rupture and you are left with a very low yield.

As an alternative to the biotinylated lipid head, we also looked to an amine head to conjugate with carboxyl coated beads. These two components would then be joined via EDC reaction. Though synthesis of these liposomes is possible, the protocol is more involved than the protocol involving biotin-strepatavidin binding and is more time intensive, with further work being required to characterize the optimal reagent concentrations.

There are a number of different mixtures one can use for organic solvents in which to disperse the lipids. Most lipids are stored in chloroform, however in my experience, for the formation of forming a dehydrated lipid layer cake, a 2:1 mixture of chloroform to methanol works best. There are also multiple ways to dehydrate the lipids suspended in organic solvents. The method typically used in the experiments of this dissertation involves placing the samples in a desiccator under vacuum pump. However, it is also possible to use a dry nitrogen stream to dehydrate larger volumes (~1mL). This is achieved by covering a sample, either with foil or a rubber stopper, and then introducing inlet and outlet needles. Place the sample in the fume hood and attach a nitrogen air source to the inlet needle. Allow flow through the sample for 2-3 hours or until fully dry. Should one require even larger volumes of lipids, it is possible to employ a rotary evaporator to dry the lipids into a layer cake.

Once a lipid layer cake is formed, the next step is the hydration step where aqueous solution is introduced and the lipid layer is agitated to allow for self-assembly of the vesicles. This can be done with beads, cargo and additional cryopreservants (i.e. sucrose) to mixed results. In general, the addition of beads should be withheld until as a late as possible. There are a few reasons for this; the primary one being that the

binding capabilities of the streptavidin coated beads can affect the self-assembly of the vesicles. Especially in the case of larger beads that are within the range of vesicle diameters (2-10 μm), there is the possibility of forming lipid-coated beads rather than liposomes with beads bound. Furthermore, the inclusion of beads in early stages adds difficulty to later centrifugation steps where the heavy magnetic beads could damage the vesicle membranes while being spun down.

Cargo should be introduced during the hydration step, especially in cases when concentrations are important to the system function. In this case, we look to exploit the self-quenching property of calcein dye as a visual cue of rupture, so it is pivotal that the internal concentration of cargo is within the desired range. Early stage synthesis and subsequent imaging showed that adding calcein dye after hydration and lyophilization produced a very low fluorescent signal, suggesting low cargo retention.

The use of cryopreservants such as sucrose has been beneficial in the synthesis of liposomes, though their main advantage has been related to osmolality rather than cryopreservation. As lyophilization is performed for long-term storage of the liposomes, the impact of sucrose in this regard has not been analyzed. However, as stated in previous sections, in the case of DPPC liposomes, the inclusion of sucrose allows the liposomes to pellet easily during the centrifugation step to remove cargo suspended in the supernatant.

Inhibiting membrane fusion

Owing to the presence of SNARE proteins within the cellular plasma membrane, it is important to incorporate a steric barrier in the design of the system. Because of the SNARE complex, phospholipid liposomes will fuse with cell membranes in the absence

of some sort of lipid functionalization. In an effort to keep the design of the liposome relatively simple, a functionalized linking molecule with one end capable of binding to biotinylated phosphatidylethanolamine heads is desirable. Additionally, the opposite end of the linker would need to be bound to some sort of ligand with which it could bind to a receptor protein on the exterior of the cellular plasma membrane.

As discussed previously, the use of PEG would be effective with regards to the inhibiting membrane fusion initiation by the SNARE protein complex as the hydrophilic nature of the molecule as well as its large size would provide steric forces as well as significant hydration forces. However, the PEG backbone may not be stiff enough to achieve the desired shearing of the liposome via magnetic actuation. As such, the possibility of using a polysaccharide chain as a linker to achieve this goal was explored. While the polysaccharide chain would not bring the same hydration forces that PEG would, a sufficiently long polysaccharide chain could provide sufficient steric separation between the liposome and the cell membrane to prevent membrane fusion. Owing to its stiffness, a chitosan chain linker appears to be a promising candidate for anchoring the liposomes.

Magnetics tensile cytometry

Helmholtz coil microscopy stage

A custom-built Helmholtz coil apparatus was constructed using copper wire wound around acrylic plastic hollow cylinders. Two sets of coils were created, one measuring 18 inches in diameter and the other measuring 6 inches. For the purposes of shearing

the liposomes via magnetic force on the streptavidin coated beads, the smaller of the two Helmoltz coils was used and run off an external power supply. The power supply is operated at a maximum of 1.3 amps during testing. Previous work has seen the use of an Arduino microcontroller used to switch the current to the coils on and off, however for this work, the flow of current through the coils is controlled manually via the external power supply.

The imaging is done via kinetic series acquisition with one image collected each second at a maximum series length of 40 due to computational memory limitations. The 63X objective is then introduced slowly to the bottom of the slide to be imaged and the halogen lamp is then dimmed to a power of roughly 0.8 V such that the imaged collected is not saturated yet features within the viewing plane are discernable.

Laser cutting of mu-metal foil

Metallic foil used for magnetic shielding and 50 µm in thickness (McMaster-Carr, Elmhurst, IL) is patterned using a UV laser cutter (LPKF, Garbsen Germany). Cutting paths were designed in SolidWorks and saved as .dxf files to be imported into the LPKF software. As the material is very thin, an appropriate laser cutting program must feature high frequencies, low power and fast marking speed. However, this must be done using a combination of passes to prevent the formation of a rough edge. By varying the marking speed, the location of the laser spot varies along the length of the cut with each subsequent pass, yielding a smoother edge. An example of tool path combinations is as follows.

Task 1

140 kHz , 2 W , 500 mm/sec , 100 repetition

Task 2

140 kHz , 2W , 350 mm/s , 100 rep.

This procedure is repeated as necessary until the cut is completely through the material. It is important to properly fix the metallic sheet in place using adhesives to ensure that the part does not drift while cutting and so that the foil does not warp out of plane due to thermal stresses. The inserts must be completely detached via the laser as attempting to remove them manually or with the assistance of tweezers will result in bending or indentation.

Magnetic tensile cytometry microfluidic chip fabrication

The microfluidic chips used in combination with the magnetic tensile cytometry chips were designed using traditional photolithography. Channel designs were drafted and sent to CAD/Art (CAD/Art, Bandon, OR) for printing as dark field masks. The masks were then used with SU-8 2100 (Microchem, Westborough, MA) to create channels on a silicon wafer. The photoresist was deposited using a WS-400 spin-coater (Laurell Technologies, North Wales, PA). The protocol used for these channels is outlined as follows.

1. Spin coat
   a. SU-8 2100
   b. Step 1: 500 rpm for 10 seconds (acceleration of 100 rpm/sec), step 2: 1800 rpm for 30 seconds (acceleration of 300 rpm/sec)

2. Soft bake

       a. 5 minutes at 65 °C
       b. 30 min 95 °C

3. Exposure
       a. 1 minute at UV exposure

4. Post bake exposure
       a. 5 minutes at 65 °C
       b. 12 minutes at 95 °C

5. Wait 20-30 minutes because features are 100 um or greater

6. Development
       a. Rinse with developer until you see excess SU-8 is gone
       b. Wash with isopropyl
       c. Dry with air

7. Silanization
       a. Silanize for 1-2 hours

The microfluidic channel mold on the silicon wafer was patterned with two alignment posts corresponding to two holes cut into each laser cut mu-metal chip. This was designed to create a consistent distance between the tips and the main channel wall as well as to prevent drifting of the mu-metal foil during curing. To create the channels, a thin layer of PDMS prepolymer was spin-coated onto the wafer at 2000 rpm for 1 minute. The mu-metal inserts were then deposited on the prepolymer layer and the wafer was degassed in a desiccator for 20 minutes. Following desiccation, the base layer of PDMS and the mu-metal insert were allowed to cure together in an oven at 60 °C for at least one hour. Next, additional PDMS prepolymer was poured over the wafer to a final thickness of roughly half a centimeter, degassed and then cured as before. Once cured, the channel molds with embedded mu-metal inserts were carefully removed using an X-acto knife and cut to size using a straight edge razor.

Liposome-cell anchoring and liposome rupture assays

For the purposes of testing liposome anchoring to cellular systems, Caco-2 intestinal endothelial cells were cultured for 24 hours on fibronectin-coated glass slides. The liposome mixtures were then introduced via micropipette in volumes of 15 μL. The solution was analyzed via epifluorescence microscopy to evaluate whether liposomes were attaching to cells via the ligand-bound linkage mechanism. To test whether the liposomes were indeed bound to the plasma membrane of the cells, imaging was performed in the red wavelength to locate fluorescently-tagged ferromagnetic beads before inducing fluid flow on the sample.

Initial testing for liposome rupture has been unsuccessful as the force achievable through the magnetic tensile cytometry system is below to target of 500 pN per liposome. Anchored liposomes with bound beads in microfluidic channels have been subjected to tensile forces via the Helmholtz coils and accompanying mu-metal inserts, but in the case of DPPC liposomes, the vesicles have remained intact. For preliminary testing with permanent magnets and paramagnetic needles using POPC liposomes, there has been instances of tethering, but no rupture, indicative of the liquid behavior of those lipids at room temperature (beyond the phase transition temperature of -2 °C).

Caco-2 Culture and Gut-on-a-chip Fabrication

Caco-2 Culture Protocol

Protocol provided by Mary Beth Wilson and modified by Kyle Justus and Eric Parigoris

Cell plating for adherent cells

1. Pre-warm all reagents to 37°C in water bath.
2. After reagents are warmed, spray bottles and hood surface down with ethanol to sterilize.
3. ***Aspirate*** the medium within the flask with an aspirating pipet.
   a. Take care not to touch or disturb the cell layer. Tilt flask and remove medium at the back corner.
4. ***PBS wash***: Wash once, gently, with PBS to remove any debris. (~3 mL PBS in T25, ~7 mL in T75).
   a. Tilt flask and add PBS near the back wall. Gently rock flask back and forth to wash cells. Tilt flask and remove PBS at back corner.
5. ***Trypsinization*** (detachment of cells from bottom of flask): Add just enough trypsin to cover the cell layer (1 mL in T25, ~3 mL in T75).
6. Seal flask and incubate for about 2 minutes in the 37°C incubator.
   a. After incubation, examine the cells under a microscope. Fully trypsinized cells should appear rounded up and no longer attached to the surface of the flask/dish.
   b. If the cells are not fully detached, place the flask back into the incubator. Some cells may require some mechanical agitation (including "rapping" the flask or "scraping" the culture surface), BUT THIS IS NOT PREFERRED.
7. ***Cell suspension***: Add 10mL of cell culture medium and mix the cells thoroughly by pipetting up and down to ensure a single cell suspension (removal of cell clumps).
   a. Note: The medium must contain serum in order to act to inhibit the trypsin. Trypsin will start to act on the excess serum proteins instead of harming the cells. Serum-free media can only be used if a trypsin inhibitor is used.
8. Stand flask on its end (cap facing upwards) to inhibit cell re-attachment, then proceed to A or B…

A) Cell Passaging

9. Add fresh media to the new culture flask(s). (~7mL for T-25 and ~12mL for T-75)
10. With pipet, resuspend cells in the stock solution, as they may have settled over time.
11. Draw an appropriate amount of the cell suspension into the pipet, and add to the new flask containing fresh media. Gently rock to distribute cells.
12. Screw cap on loosely (to allow for adequate oxygen perfusion of the flask).
13. Label the flask with the cell type, passage number, name and date.
14. Place flask in 37oC incubator.

B) Cell plating in Transwells

9. Make a diluted "working cell solution" by adding fresh media and cells into a 50 mL conical tube.
10. Gently mix the working solution by pipetting up and down.
11. Add the appropriate volume of diluted cell solution into each well of the Transwell plate. For 24-Transwell plate, seed 20,000 cells/membrane.
12. Label the plate lid, and place plate in 37oC incubator.

Caco-2 Culture Maintenance

1. For growth in T25 or T75 culture flasks, change rinse flask with PBS and change media after cells are adherent, typically 12-24 hours after passaging cells into a fresh flask. This is done to remove residual trypsin from solution.
2. Check cell proliferation daily under optical microscope. Wear gloves and disinfect flask with ethanol before placing back into incubator.
3. Once cells have reached 70-80% confluency, prepare reagents for cell passaging.

Caco-2 Transwell Maintenance

For growth in Transwell membranes, change media in apical and basal reservoirs (i.e. above and below the membrane) every 2-3 days.

1. Aspirate old culture media using fine-tipped glass aspirating pipette.
2. Rinse top and bottom compartments with PBS (200 µL and 500 µL, respectively)
3. Aspirate PBS
4. Pipette fresh culture media into top and bottom compartments (200 µL and 600 µL, respectively). In the interest o cell viability, deliver media to the top compartment first as it is a time sensitive process and cells can dry out.

Staining Protocol for Phalloidin and Hoechst

1. Cultured cells for 21 days in Transwells
2. Remove media and rinse cells with ice cold PBS 2 times (5 minutes each) (1.5 ml top and 2.5 ml bottom)
3. 4% Parafomaldehyde for 15 minutes at room temperature (1.5 ml top and 2.5 ml bottom)
4. Rinse cells with ice cold PBS 2 times (5 minutes each) (1.5 ml top and 2.5 ml bottom)
5. Add 0.1% Triton X and let sit at room temperature for 5 minutes (top only from here on)
6. Rinse 3 times with PBS (5 minutes each)
7. Add **200 µl** (or 500uL) of actin stain (5 µl of methanolic stock solution for every 200 µl of 1% BSA in PBS) to top only and leave at room temperature for 20 minutes
8. Rinse 3 times with PBS (5 minutes each)
9. Add **500 µl** of Hoechst stain to apical side (**varying concentrations**) at leave at room temperature for **5/10 minutes**
10. Rinse 3 times with PBS (5 minutes each)
11. Put on cover glass and add fluoromount

Staining Protocol for Immunostaining of Caco-2 for Villin and ZO-1

Antibodies:

Rabbit anti-ZO-1 [1.0 µg/mL] + Alexa Fluor 488 donkey antirabbit [10 µg/mL](Green) - 500 µl for 1 hour

Villin (CWWBI) (mouse) [1:50 dilution (?)] + Alexa Fluor 594 goat antimouse [10 µg/mL] (Red) - 500 µl for 1 hour

1. Cultured cells for 21 days in Transwells
2. MG1655 bacteria grown overnight and diluted 10:1 Caco-2 media : overnight culture mixture
3. MG1655 introduced above or below well for a predetermined period of time (between 2 and 6 hrs) and incubate
4. Remove media and rinse cells with ice cold PBS 2 times (5 minutes each) (1.5 ml top and 2.5 ml bottom)
5. 4% Parafomaldehyde for 15 minutes at room temperature (1.5 ml top and 2.5 ml bottom)
6. Rinse cells with ice cold PBS 2 times (5 minutes each) (1.5 ml top and 2.5 ml bottom)
7. Add 0.1% Triton X and let sit at room temperature for 5 minutes (top only from here on)

8. Rinse 3 times with PBS (5 minutes each)
9. Add 5% BSA and incubate for 30 minutes
10. Add primary antibodies for ZO-1 (1 µg/ml) and Villin (1:50 dilution) in a 1% BSA solution for 1 hour (room temperature)
11. Rinse 3 times with PBS (5 minutes each)
12. Add secondary antibodies ZO-1 and Villin (10 µg/ml) in a 1% BSA solution for 30 minutes (room temperature)
13. Rinse 3 times with PBS (5 minutes each)
14. Add 500 µl of Hoechst stain to apical side (1 µg/ml) at leave at room temperature for 5 minutes
15. Rinse 3 times with PBS (5 minutes each)
16. Put on cover glass and add fluoromount

Live/Dead Staining Protocol

1. Rinse cells with ice cold PBS 2 times (let PBS sit for 5 minutes for each wash)

2. Add live dead stain (Calcein - 2 ug/ml and Ethd-1 - 2 ug/ml) and leave for 40 minutes (add 3 ml)

3. Rinse cells with ice cold PBS 2 times (let PBS sit for 5 minutes for each wash)

4. Image with microscope

I. Upper and Lower Channel Fabrication
Following protocol established by Eric Parigoris and modified by Kyle Justus

A. Silicon Wafer Silanization

1. Clean the wafer with isopropyl alcohol, rinse it with water, and dry it using the air in the fume hood. Don't open the air valve too much, as it can damage the features on the wafer. Clean the wafer after each use.
2. Make sure the wafer is clean, by following step 1. Add the silicon wafer with the channel mold in an open petri dish. Add 1 drop of TFOCS to a small petri dish, and also place it in the desiccator. Leave it running for 2 hours. After 2 hours, seal off the vacuum, and shut the pump off. Leave it in the desiccator overnight. **Note:** I would recommend silanizing the channel wafer every few weeks.

B. Fabrication

3. Mix 30 grams of PDMS base with 3 grams of curing agent and pour onto the silicon wafer (containing 4 channels) to make the top channel.
4. Put the wafer in the desiccator and degas for 30-40 minutes.
5. Take the petri dish out of the desiccator, and let it sit on a flat surface for a few minutes to make sure the PDMS is level.
6. Using 2 popsicle sticks, push the silicon wafer down to make sure it is as close to the bottom as possible, and center it in the petri dish.
7. Turn the hot plate on 85 – 90 ° C. Make sure to cover the petri dish so dust particles don't fall in it. Leave the wafer on the hot plate for ~45 minutes. **Note:** try to do this step on the hot plate since it is more level than the oven, and if you forget it in the oven, the petri dish can warp and crack the wafer.
8. Use an X-Acto knife to cut out the PDMS. Be really careful with this step, since it is not that hard to crack the silicon wafer. I would recommend cutting the knife along the edge of the petri dish. Be careful not to cut on top of the wafer, if it not in the center of the petri dish. Then move the knife inward a little and cut a concentric circle. Peel this outer ring off. Once the PDMS has no contact/little contact with the outer surface of the petri dish, it is easier to remove the wafer. Once the wafer is out of the dish, carefully peel off the channels. You can then cut them to size.
9. Repeat steps 3 – 8 using 13 grams of base, and 1.3 grams of curing agent for the top channels. Make sure to clean the wafer in between. Degassing times and heating times may be slightly shorter since there is less PDMS.

II. Membrane Fabrication

A. Post Array Mold Silanization

10. Repeat step 1, but be very careful with this wafer, since it is much more expensive and the features are more delicate. Only use very light air.
11. Repeat step 2. However, instead of silanizing this wafer every week, you will need to silanize it every other time you use it.

B. Spin Coating PDMS

12. Mix ~10.3 ml of cyclohexane (approximately 7.5 grams) with 15 grams of PDMS base, and 3 grams of curing agent. If you have membrane tearing issues, you can increase the amount of curing agent to 3.5 or 4 grams.
13. Desiccate the cyclohexane and PDMS mixture for about 30 minutes, or until there are no more bubbles coming out. Use the smaller desiccator for this.
14. Spin coat the cyclohexane/PDMS mix on the wafer for 1 minute at 500 rpm.
    a. Bring the weigh boat as close to the wafer as possible (without touch it) to minimize bubble formation.
    b. Add it close to the center of the wafer – I usually poured at the space between where the 3 post arrays meet the 1 post array going the other direction. You only need to pour a few ml of the mixuture.
    c. Make sure the wafer is completely centered to get an even layer. If you have trouble centering it, look at the circular mark on the bottom of the wafer to help guide the placement on the chuck.
15. Press the vacuum button to turn it off. Carefully remove the wafer from the chuck, and cover it with half of a petri dish so no particles get in it as your prepare the polycarbonate sheets.

C. Polycarbonate Sheet Preparation

Note: Steps 16 – 17 must be done beforehand. These steps only must be performed when the polycarbonate sheets that I left run out.

16. Use the laser cutters in the machine shop to cut the polycarbonate sheets to size ("Polycarbonate rectangles.SLDPRT"). Be sure to leave both sides of the backing on the polycarbonate sheet so the laser cutter does not damage the

polycarbonate itself. Use the following settings for the laser cutter, and try to use the one on the left:

Speed: 40

Power: 15

Frequency 500

Leave a few millimeters between each of the polycarbonate rectangles, as it turns a small region around the rectangle yellow.

17. Put a few textbooks on top of the polycarbonate sheets, and leave them for a few hours so they flatten.

D. Polycarbonate Sheet Application

18. Use very fine tweezers to carefully remove both backings on the polycarbonate sheet. Peel from the corner, and be careful not to scratch the polycarbonate or dent it. If there is a dented sheet or you put a dent in it, throw it away and use a new one (otherwise it can affect the contact area between the PDMS and polycarbonate).

19. Plasma oxidize the polycarbonate sheets on the standard plasma oxidation cycle.

20. After the plasma oxidation is finished, gently place the polycarbonate sheets over the post array regions. This is one of the trickiest part of the procedure, so here are some tips:

    a. Using fine tweezers, pick up one polycarbonate sheet, and align the long edge of the polycarbonate sheet with the long edge of the etched rectangle. Once the edge is aligned and is touching the PDMS, drops the polycarbonate sheet.

    b. Make sure that the side of the polycarbonate sheet that was plasma oxidized is face down, so that it contacts the cured PDMS.

    c. Once you release it, you can then ensure that the PDMS wets the entire polycarbonate sheet. Use the tweezers to lightly push down on the polycarbonate membrane, to facilitate the PDMS spreading. Work your way along the rectangle from one side to another.

    d. NEVER press your tweezers on the region above the post array, only on the areas surrounding it. Try to minimize the amount of air bubbles.

    e. Don't work from either side towards the middle, because you will get a large air bubble in the middle, above the post array. Work from one side down to the other.

    f. Once the PDMS has spread across the entire polycarbonate sheet, you

can then reposition the polycarbonate rectangle. Ensure that the polycarbonate rectangle is completely within the outlined rectangle in the wafer, as close to being centered as possible.

g. Repeat this process for all 4 of the post array regions.

h. Don't rush so that you can damage the wafer, but try to do this process with all 4 polycarbonate sheets in less than 2 – 3 minutes, as the plasma treatment will wear off in that time scale. At the same time, don't rush and create a lot of air bubbles. If you need, place down all of the polycarbonate sheets first, and once they are all down, begin the process of spreading the PDMS and reposition them. However, this will increase the chance for bubbles.

E. Desiccation

21. Once all 4 polycarbonate sheets are inside of the etched rectangles on the silicon wafer, carefully place the wafer inside of the desiccator. Desiccate until any bubbles trapped under the polycarbonate sheet are removed.

a. If there are minimal or very small air bubbles, you do not need to do this step.

b. If there are large air bubbles before you desiccate, the polycarbonate sheet will lift and separate from the PDMS and wafer during desiccation. This will weaken the effect of the plasma treatment, and the PDMS will later separate much easier from the polycarbonate sheet. This happens more so in the smaller desiccator. May need to re-examine this step, and find a better procedure to reduce air bubbles so this does not occur during desiccation, or a way to eliminate the need for desiccation.

22. CAREFULLY let the air into the desiccator. If you do it too quickly, the wafer will go flying and can crack.

F. PDMS Slab Fabrication

Note: Steps 23 – 28 must be done beforehand. I left an acrylic template, so step 23 is only necessary if it breaks. The one that I left is made out of black acrylic, NOT clear. The clear one is the wrong size. I also left a few PDMS slabs – you will only have to perform steps 24 – 28 if they break or warp.

23. Laser cut the file called "Laser cutting template.SLDPRT." Additionally, cut a 4" circle. Cut both of these out of 1/8" acrylic. Use the acrylic glue to glue these two

pieces together. Use a clamp to ensure they are concentric. The glue works by capillary action, so brush around the edges, and the glue will seep in and bond the two pieces of acrylic together. Let it sit for a few minutes, and it is good to go.

24. Place aluminum foil around this laser cut piece that you just made. Mix 60 grams of PDMS base, and 6 grams of curing agent, and pour it into the acrylic mold.

25. Degas the PDMS for about 1 hour, or until all of the air bubbles are gone. Sometimes it take a while, since the bubbles will get trapped in the small gap between the 2 acrylic pieces.

26. Heat the PDMS on the hot plate for about 1 hour at 90 ° C, or until it is completely cured.

27. Carefully peel off the PDMS slab. When you get to the regions with features, be careful that the PDMS doesn't rip.

28. Cut the PDMS slab to the appropriate size.

G. PDMS Slab Silanization

Note: These 2 steps must be done beforehand. It is only necessary to silanize the PDMS slab every few weeks.

29. Plasma oxidize the PDMS slab, with the features facing upwards. You will need to bend it a little for it to fit in the machine. Quickly transfer it to the desiccator. **Note:** I left a few of these – you will only have to do this process if they break or warp.

30. Add 1 drop of TFOCS to a small petri dish, and place it in the desiccator. Leave it running for 2 hours. After 2 hours, seal off the vacuum, and shut the pump off. Leave it in the desiccator overnight. **Note:** I would recommend silanizing the PDMS slab every few weeks.

H. Testing Stand Fabrication

Note: These steps must be performed beforehand. I left a testing stand, so this is only necessary if it breaks.

31. Laser cut the file "Membrane_stand_bottom.SLDPRT" out of ¼" acrylic.
32. Laser cut 3 of the "Membrane_stand_legs.SLDPRT" out of ¼" acrylic.
33. Laser cut the file "Membrane_stand_top.SLDPRT" out of 1/8" acrylic.
34. Glue each of the 3 legs into the bottom of the testing stand, using the acrylic glue

as described before. Make sure they are straight, and can easily fit in the top portion of the testing stand.

I. Application of Weight to Silicon Wafer

35. Take the wafer (directly from step 22) and place it on the bottom portion of the testing stand. There is an outline etched in the acrylic for where it should be placed.
36. Use tape to clean the bottom of PDMS slab (the side with the features).
37. Place double sided top on the top side of the PDMS slab (the side with no features). Make sure the tape is flat on the PDMS.
38. Carefully place the PDMS slab on top of the polycarbonate sheets sitting on the wafer. Ensure that the PDMS sits directly on the polycarbonate sheets for all four of them. **Note:** The post array regions are not exactly centered on the silicon wafer, so the the PDMS slab should not be exactly in the center of the wafer.
39. Carefully place the top of the testing stand through the legs, and gently push it against the PDMS slab. Make sure that the top acrylic piece is level, and that the tape sticks to the PDMS slab.
40. Go to the vacuum oven in the yellow room, and cover the bottom with aluminum foil. Place the entire assembly in the oven on top of the foil, and make sure it is OFF.
41. Fill a 1000 ml beaker with water, and add a 1 pound weight to the water. The weight is in the top drawer in the 3D printing office in the machine shop. The total mass of the water, beaker, and weight should be about 1.8 Kg.
    a. If this is not enough, you can add a larger weight to the beaker. Alternatively, you can use the green mortar in the lab.
42. Carefully place the beaker on the top piece of acrylic. Make sure the weight is in the center of the beaker, and the beaker in the center of the post array regions. **Note:** The post array regions are not exactly centered on the silicon wafer, so the beaker should not be exactly in the center of the wafer.
43. Let the weight sit on the testing stand for 30 minutes – 1 hour with the oven power OFF.

J. Curing the Membrane

44. After waiting 30 minutes – 1 hour, close the oven door, and turn the power on.
45. Turn the oven temperature to approximately 60 ° C.
46. Close the left valve, and leave the right valve open slightly. Then turn on the pump, and wait for the reading on the gauge reads 25.

47. Shut the pump off, and quickly close the right valve. Both of the valves should now be closed.
48. Let the apparatus sit in the oven overnight.

K. Membrane Removal from Wafer

49. Open both valves on the vacuum oven, and wait for the pressure value to drop below 5. Turn off the oven, and remove the weight.
50. Carefully remove the entire assembly, and bring it back to the lab.
51. Make sure to shut off the oven, clean up any water, and leave the door open so it cools down quickly, in case you repeat the procedure.
52. Remove the top of the testing stand. The wafer and PDMS slab will stick to it.
53. Use the squirt bottle to carefully squeeze isopropyl alcohol between the PDMS and the top acrylic layer. Try not to drip isopropyl on the silicon wafer.
54. The isopropyl alcohol will help to remove the slab from the top acrylic portion, since it wets the double-sided tape.
55. Once you remove the top acrylic layer, carefully peel the PDMS slab off of the silicon wafer. If you have a lot of trouble peeling it off, or the spin coated PDMS bonded to the slab, this means you need to silanize the slab again.
56. Once the slab is removed, use the fine tweezers to trace the outline of each polycarbonate sheet. Press hard enough to rip the PDMS as you slide the tweezers, but don't press too hard or you can damage the wafer. Again, don't touch the wafers to the post array, or on the polycarbonate sheet directly above the post array region.
57. Run the tweezers under the edges of the polycarbonate sheet to delaminate all 4 sides. Be very gentle, as you don't need to press hard to do this.
58. After the edges are delaminated, grab the polycarbonate sheet along the shorter side. Try to have the tweezers grab the entire side. Carefully, peel away the polycarbonate sheet and cured PDMS membrane.
    a. The membranes often rip, or crinkle. They need to be flat against the polycarbonate sheet in order for the devices to properly seal.
    b. Try to lift the polycarbonate sheet up without bending it backwards. This is the hardest step, and you may need to try different ways to successfully get them off without wrinkling/ripping them. NOTE: Adding a few drops of ethanol between the PDMS and the silicon wafer during removal will ease the process and hinder the formation of wrinkles or tearing
    c. If you are having a lot of trouble, go back and follow the procedure for silanzing the wafer. You will probably need to silanize it every other time you do this entire procedure.
    d. Once you successfully remove one, place the polycarbonate sheet with

the PDMS face up in a petri dish to keep it clean until you are ready to use it.

L. Residual PDMS Removal from Membrane

59. Because the thin layer of PDMS often breaks on at least one of the post array regions and is hard to remove, it is easiest to spin coat a new layer of PDMS on top of it to prevent damaging the post arrays. Mix 20 grams of PDMS base with 2 grams of curing agent.
60. Degas for ~30 minutes.
61. Follow step 14 using the regular PDMS instead of the PDMS/Cyclohexane mix. Still use 500 rpm for 1 minute.
62. Remove the wafer from the chuck, and put it on the hot plate at 90 ° C for 20 – 30 minutes. Make sure it is on aluminum foil, and not directly on the hot plate.
63. Once it is cured, peel off the thicker PDMS layer. This will help to clean the wafer, and remove any broken/residual PDMS pieces that are remaining from the previous spin coat.
64. Follow step 1 to clean the wafer, and you can use it again to make more membranes.

III. Device Assembly

A. Upper and Lower Channel Preparation

Note: The top channel is the thicker channel, and the bottom channel is the thinner channel. The top channel will have the four holes for the inlets and outlets. The bottom channel needs to be thinner so that you can image the devices on the 10X.

65. Punch 2 holes in the inlet and outlet of a channel top (thicker one).
66. Punch 2 holes in the inlet and outlet of a bottom channel (thinner one). This will *not* be used in the device, but this will be used as a template. You only need one of these, and can reuse it every time until it rips.
67. Place the thick (top) channel facing up, and align the thin (bottom) channel *template* facing down on top of the thicker channel. The straight parts of the channels should be well aligned.
68. Next, punch the outlet and inlet (for the bottom/thin channel) into top/thick portion, using the two holes from the bottom/thin that you created in step 66. Place the flat needle in the hole in the thinner channel (previously created in step 66), and push straight down into the thicker channel. The point of this is just to use the thinner channel as a placeholder so you know where the hole should be in the thicker channel. The end result should be four holes in the top/thick channel.
    a. Note, steps 67 and 68 might be a little confusing, because of the way you need to do this, the top (thick) channel is temporarily on the bottom of the assembly. You can find a different way to do this, as long as the end product is a thick channel with 2 inlets and 2 outlets, which will line up nicely when the thin channel is placed on top of it.
69. Take a new bottom channel (thin) and align it with the thicker channel containing the 4 holes. Once the straight channel portion, inlet holes, and outlet holes are nicely aligned, cut any portions of either channel that overhang. You want the rectangles for the top and bottom portions of the PDMS to be the same size, to help create a good seal.
70. Next, cut a small portion off of each of the four corners, using a razor blade, at a 45-degree angle. This will later help with the alignment.

B. Sealing the Device

71. Take one of the good membranes, and peel away the edges. There will be

thicker regions of PDMS around the edges that you have to remove. If you don't there won't be a good seal and the devices will leak. Use a razor blade and/or tweezers to pull them away. Be careful to keep the membrane clean when doing this.

72. Take the top channel containing 4 holes (from step 70), and clean it 3X with scotch tape. Place this and the membrane, both face up, into the plasma oxidizer and treat it for the standard cycle.

73. Once it is treated, place the channel against the membrane. Make sure that the channel is facing down, and the membrane is facing up. The portion of the membrane with the pores should cover the entire channel, and end right before the inlet/outlet. Press down on the channel to seal it against the membrane, and place it in the 60 ° C for a few hours.

74. Remove the channel top and membrane from the oven, and peel off the polycarbonate sheet.

75. **Use a needle to push through the two holes in the PDMS that are not connected to a channel. These are the inlets and outlets for the bottom channel, which will soon be placed on it. If you don't do this step, it will be harder for the fluid to enter the bottom channel, since the thin membrane is blocking the path. This step is very easy to forget, and if you don't do it, the device is no good.**

76. Place the channel/membrane face up in the plasma oxidizer.

77. Clean the channel bottom (thin channel from step 70) with scotch tape 3X, and place it face up in the plasma oxidizer.

78. Run the standard plasma treatment cycle, and carefully align the devices. You can use the channel inlets/outlets, the straight channel portion, and the cut edges to help you align the device.

79. Press the two channel halves against each other, and place it in the oven for a few hours.

80. Remove the device from the oven, and you have a completed gut-on-a-chip device!

IV. Permeability Verification

A. Food Coloring

81. Cut four 1" long pieces of tubing. At the end of each of them, cut it at a 45 degree angle.
82. Place tubing into each of the inlets and outlets. The angled portion should open facing towards the channel (ie the longer side of the tubing end is closer to the edge of the PDMS and the shorter side of the tubing end is closer to the channel). Using a 3 ml and a yellow needle tip, add red food coloring in the top inlet, and blue food coloring in the bottom inlet.
83. Inspect the device to ensure there is no leakage: 1) between the channels, 2) inside the device and outside of the channels, and 3) outside of the device. You will see faint traces of blue/red if there is leaking.
84. Remove the food coloring from the device, rinse the channels with water, and remove the water.
85. Plasma treat the entire device.
86. Repeat step 82 by adding red food coloring to the top inlet, and blue food coloring to the bottom inlet. This time, because the device is now hydrophilic, you should see diffusion between the red and blue food dye. However, the whole device is now hydrophilic, so it also makes leaking (that is not due to the permeable membrane) more apparent.
    a. Look for leaking around the edges of the device, and out of the device
    b. Diffusion, of the fluid across the permeable membrane, should take place *first* in the straight channel portion where the channels are collinear, and work its way outward towards the inlets and outlets. The diffusion should *not* begin at the angled inlets and outlets, and work towards the center.
87. If the diffusion seems to occur first in the collinear portion of the channels, it is a successful device. If you are unsure, use the second verification method as well. If there is significant leaking outside of the channels or outside of the device (a little is okay), it is no good. If diffusion *first* occurs at the flanked regions, move onto the second permeability verification method.

B. Fluorescent Beads

88. Plasma oxidize the entire device.
89. Dilute 1.9 um green fluorescent polystyrene beads 1:100 in a 0.2% tween-20 in DI water solution.
90. Place 1" long tubing in each of the inlets and outlets (following steps 81 – 82).

91. Use a 3 ml syringe, and add the bead solution to the top channel inlet, and 0.2% tween-20 in DI water solution with NO beads to the bottom inlet.
92. Let the device sit for ~10 minutes.
93. Look at the device with fluorescence under the microscope. Look for leakage 1) between the channels, 2) inside the device and outside of the channels, and 3) outside of the device
94. In particular, look at the region between the two flanked inlets, and two flanked outlets. This is a common region of leakage, which would cause diffusion from the inlets/outlets towards the center (*not* due to permeability of the membrane), instead of from the center outwards (due to permeability of the membrane).
95. If there is no leakage, then this is a successful device.
96. After you verify a few devices, you may not need to verify the permeability of all of them. If fluid leaks out of the device or you think it is not permeable for a certain reason, you can just throw it away and start with a new one, or double check the permeability using one of these methods. You can also try a Lucifer yellow assay to further investigate the permeability.
97. Additionally, you can intentionally offset the top and bottom channels such that there is a "step" between them. Flow fluorescent beads through the top channel and then using confocal fluorescence microscopy, observe the trajectory of the beads, using the "step" as a sort of fiduciary marker.

V. Cell Culture

Note: Step 105 should be done beforehand.

98. Dilute rat-tail collagen at a concentration of 100 ug/ml into pre-chilled DMEM (recommended by gut-on-a-chip protocol paper). I have always used Caco-2 media with FBS and pen/strep, and have never had a problem.
99. Plasma oxidize a successful gut-on-a-chip device along with four 1" long pieces of tubing (follow steps 81 – 82 to cut and insert the tubing), and bring them into hood right away.
100. Place the tubing into each of the channel inlets and outlets.
101. Add the collagen to a 3 ml syringe, and using the yellow needles, add it to the top and bottom channel through the tubing.
102. Incubate the device with the collagen in the 37 ° C cell culture incubator overnight.
103. Fill two 10 ml syringes with warm Caco-2 media using the yellow syringe tips. Place each of them in the large syringe pump.
104. Specify the settings of the syringe pump (ie – ensure the diameter is for the 10 ml syringes, and not the 3 ml syringes), and set the flow rate to 30 ul/hr.
105. Cut two pieces of tubing large enough to go from the end of the needle, to the tray on the left cell culture incubator. You may want to measure this out by placing a device in the incubator to get the exact length of tubing needed. Follow steps 81 – 82 for how to cut and insert the tubing into the PDMS.
106. Punch holes in the top of two 15 ml centrifuge tubes that are a size slightly larger than the tubing. These will be used as the waste containers for the media.
107. Cut two pieces of tubing that will go from the two outlets to the 15 ml test tubes. Cut them long enough so a few inches (about 2 – 3) of the tube can extend into the centrifuge tubes (to ensure they don't come out and leak in the incubator).
108. Plasma oxidize the 4 pieces of tubing, and quickly transport them to the syringe pump.
109. Attach one end of the longer tubing to the needle, and the other end to the top channel inlet. Repeat this for the bottom inlet as well.
110. Attach one end of the shorter tubing to the top outlet, and place the other end in the centrifuge tube. Remember a few inches should extend into the centrifuge tube. Repeat this for the bottom outlet. You can sit the centrifuge tubes in a test tube rack.
111. Turn on the syringe pump and purge it briefly to ensure media is going through both inlets, and leaving both outlets. If it is not working, make sure that

the tubing isn't wedged into the PDMS and blocking flow. The tubing should be placed in the inlet/outlet so it is snug enough to remain in place a few days, but not too far that it will become wedged into the PDMS and block the flow.

112.   After a brief purge, let the media run through the device overnight, or throughout the day (6 – 8 hours minimum).

113.   Take a confluent flask of Caco-2 cells, trypsinize them, and spin them down. Resuspend the cells in 1 – 2 ml of media. When I used the hemocytometer, I would get concentrations of 2.5+ million cells/ml, but the exact concentration isn't too important. Just do this step when the flask is fully confluent.

114.   Stop the syringe pump, and remove all four pieces of tubing.

115.   Cut two 1" long pieces of tubing, plasma treat them, and insert them into the top inlet and outlet ONLY. Be sure to double check that you are using the top channel.

116.   Add the centrifuged cells in 1 – 2 ml of media to a 3 ml syringe with a yellow needle, and add the cell solution to the top channel. Let it incubate in the top channel for 3 hours.

117.   Repeat steps 108 – 109 using the same tubing set. **Note:** The protocol paper from Harvard recommended to only perfuse the top channel with media until the cell layer was confluent, but we decided to do both, as we didn't think it would cause any harm.

118.   Repeat step 110, but very briefly. The purpose is to make sure that fluid can travel through both channels, since it will be left for a few days. Only purge for a very short time, otherwise the cells will begin to lift.

119.   The Harvard protocol paper claims it takes 24 – 36 hours for the layer to become confluent (this is when they would flow fluid through the bottom channel). I let it run for a few days, and imaged the cells. The Harvard paper claims 3 days to differentiate.

120.   I never had time to do an actin stain as a marker of the cell differentiation. When you do this, you will need to devise a way to easily flow different fluids through the channels. If you do it by hand with a syringe, it will lift the cell layer. If you do it with a syringe pump, it will take a really long time since you have a bunch of different fluids you need to use (PBS, BSA, Phalloidin, etc), and in small quantities.

Chapter 3 Integrating genetically modified cells and stretchable materials within a bio-sensing soft robot

Introduction

Developing the next generation of soft robotic and soft matter systems will be tremendously enhanced through advancements in the emerging field of synthetic biology. Essentially, synthetic biology allows development of bio-inspired architectures that enable integrated functionality of biological systems across different length-scales. These approaches have been utilized to produce soft, lightweight, and multifunctional systems that match the robust mechanical properties and rich versatility of natural biological tissues and organisms (*39, 62-65*). Examples include artificial skin composed of deterministically patterned electronics (*66, 67*) and pneumatically-powered robots capable of color change through microfluidics (*68, 69*), chemical stimulation (*70*) or electroluminescence(*71*). Similarly, soft and elastic materials have been utilized to create devices that mimic natural organisms (*72-77*) and bioinspired grippers (*63, 78, 79*). In addition to pure materials-based systems, natural cells can be integrated with soft materials to respond to external stimuli, such as swimming and crawling bio-hybrid robots powered by cardiomyocyte cells cultured on polydimethylsiloxane (PDMS) film (*54, 80*)and skeletal muscle tissue engineered from myoblasts (*81*). By effectively reprogramming the inner workings of cells to exploit their inherent versatility, researchers have also created microscale machines capable of functioning as sensors, computational tools, and timekeeping devices (*56, 61, 82-85*). The resulting synthetic biological systems offer robust and versatile performance, and allow for miniaturization.
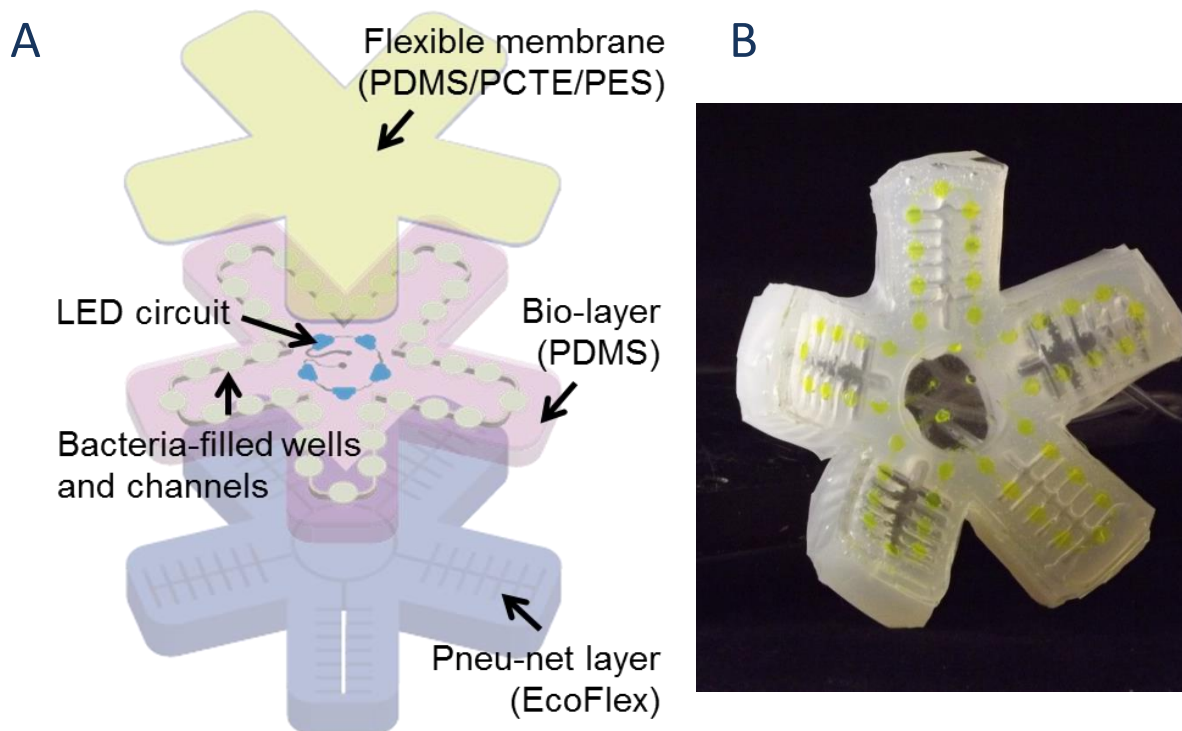
Figure 3.1 (A) Our approach integrates genetically modified E. coli housed in fluidic wells and channels within a PDMS polymer mold. This enabled an integrated established soft robotic system featuring pneumatic actuation and embedded electronics with feedback from engineered cellular systems. (B) The device filled with calcein under PN actuation (LED circuit not shown).

Together, these properties make synthetic cells promising candidates as subcomponents within an integrated, flexible, bio-inspired structure. Implementation of synthetic biological systems within flexible systems has the potential to dramatically increase system functionality, as well as reduce spatial requirements for external control systems.

Device Design

The construction of a biosensing soft-robot requires matching the dynamics of biological reactions inside synthetic cells and mechanical-electrical controls inside the soft robot,
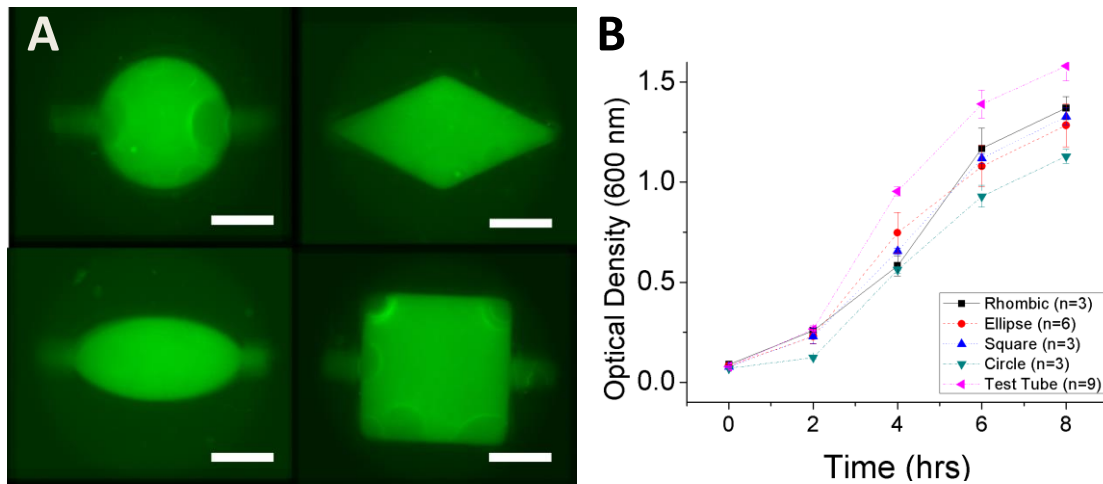
Figure 3.2 (A) Induced chemo sensitive bacteria were grown in the four well cross-sections and imaged using an epifluorescent microscope. Shown are aggregate images of ten wells, with air pocket formation shown in some, most notably in the square geometry. Scale bars = 1 mm. (B) Growth curves of pT7 strains in varying well shapes over 8 hours.. Optical density measurements were recorded at two hours increments using an electrospectrophotometer. Data represent three to six replicates and SEM.

as well as ensuring compatibility of interfaces between synthetic cells and robot host. To demonstrate how these challenges can simultaneously be addressed, we create a pneumatically-powered gripper that incorporates each of the basic sub-modules for biosensing. Controlled biological response is accomplished using a genetically modified bacterial strain that functions as a receptor for chemical or optical sensing. This bio-hybrid system enables a unique combination of soft robotic actuation and synthetic photobiology through light-activated gene expression. The gripper is composed of an array of "pneu-net" actuators (*70, 86*), an LED circuit, and a microfluidic network filled with modified Escherichia coli (Figure 3.1). The E. coli are contained in isolated growth chambers, which are separated from the environment by a porous membrane that retains the bacteria but allows for exposure to chemicals in the surrounding fluid (Figure 3.1). Synthetic bacteria are engineered using either a chemically-inducible pT7-GFP

genetic module (*87*) that expresses a green fluorescent protein (GFP) or a pDusk-GFP genetic module which expresses GFP in the absence of blue light (470nm) (*60*) (Figure 3.4).

For growing and housing these synthetic bacteria, a flexible PDMS bacterial culture layer is designed and fabricated using 3D-printed molds. The wells and channels within this layer are then sealed with a membrane and synthetic bacteria are delivered through the liquid media via fluidic channels. A flexible electronic layer containing an LED circuit is also embedded within the PDMS layer. Activation of the internal LED excites fluorescent proteins produced within the synthetic bacteria, providing a measurable sensory output (Figure 3.1). The design of the device facilitates easy manipulation of biological materials in liquid suspension and interaction between bacteria and external environments, while retaining biological integrity and mechanical properties suitable for soft robotic applications.
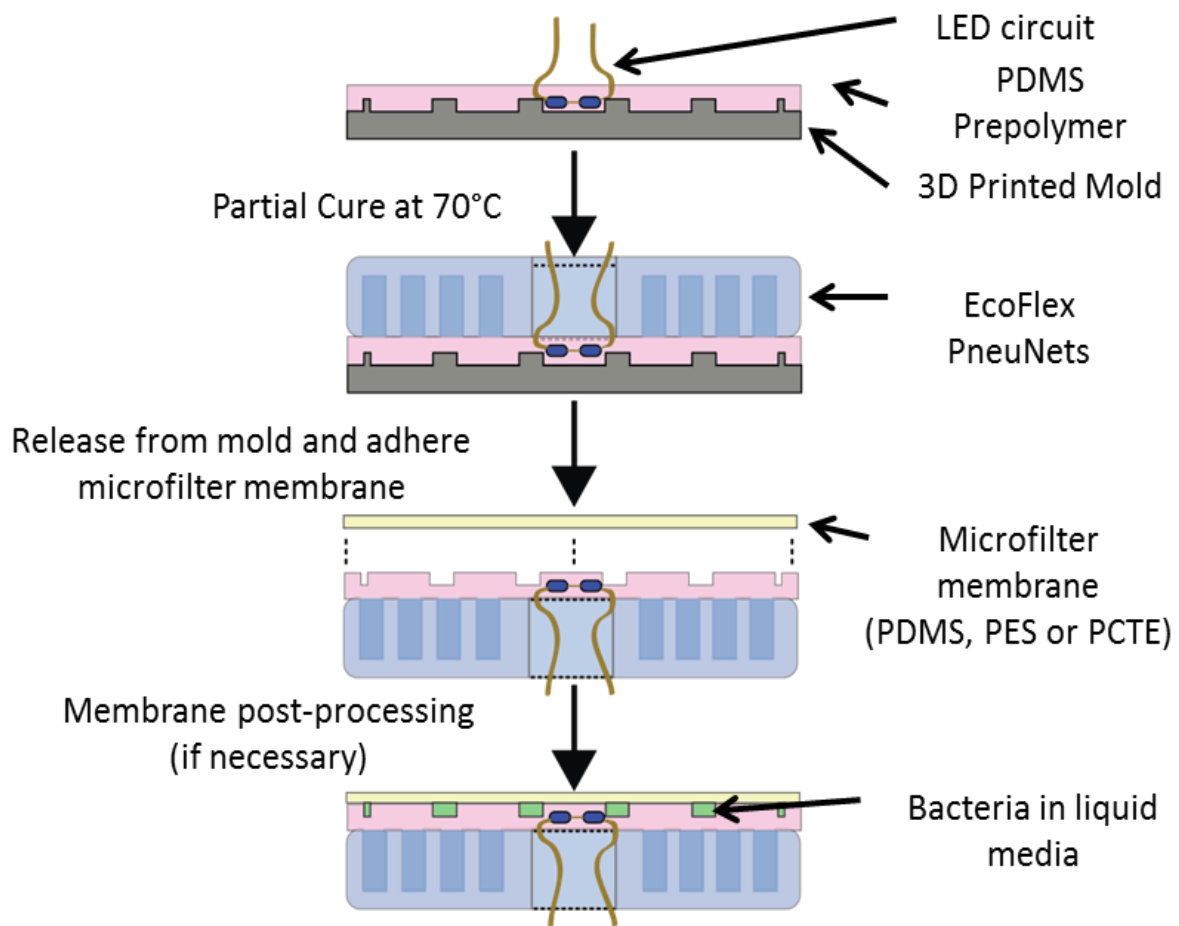
Figure 3.3 The device is fabricated using a combination of 3-D printed molds and a series of curing, partial curing and plasma oxidation steps. First, the biolayer is created by pouring PDMS prepolymer into a 3-D printed mold featuring the desired well design. The LED circuit is then set in place and the layer is partially cured. Following this, an EcoFlex layer featuring the Pneu-Net channels is placed over the partially cured PDMS, which is then allowed to fully cure. Once the two layers are cured together, they are removed from the initial 3-D printed mold and cleaned with adhesive tape before the wells are sealed with a membrane and filled with liquid bacteria cultures.

Next, we examine the patterned well geometries in terms of growth and optical performance. Growth of genetically modified bacteria in four distinct geometries of constant volume (circular, rhombic, square and ellipsoidal patterns) are measured and found to produce minimal effects on bacterial proliferation (Figure 3.2). Due to the
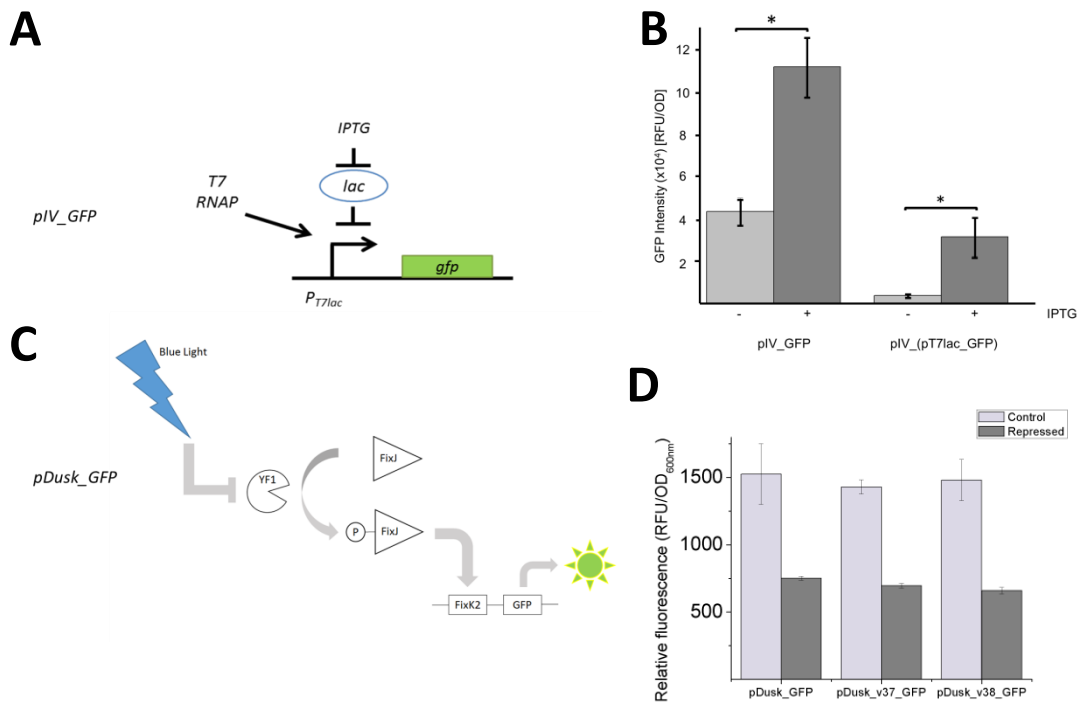
Figure 3.4 (A) The chemo-sensitive E. coli genetic module features a T7 promoter and a lac repressor, which inhibits the synthesis of green fluorescent protein (GFP) through the gfp gene in the absence of IPTG. (B) GFP intensity was measured in two chemo-sensitive strains, named pIV_GFP and pIV_(pt7lac_GFP), four hours after introduction of IPTG. (C) The genetic modules pDusk_GFP, pDusk_v37_GFP and pDusk_v38_GFP all exhibit opto-sensitive behavior. (D) GFP intensity was measured in three opto-sensitive strains, named pDusk_GFP, pDusk_v37_GFP and pDusk_v38_GFP, four hours after repression due to blue LEDs (λpeak = 465 nm).

symmetry and low propensity for air pocket formation during the fluid introduction, circular wells are selected for the implementation of the gripper.

Since the ability to communicate both in terms of excitation and then feedback through fluorescent proteins is a strong path for inorganic-organic communication, we implement a series of blue wavelength flexible LEDs. These LEDs are embedded within the PDMS biolayer to function as both a stimulation mechanism for the optically sensitive strains, as well as an excitation method for GFP in all strains. The LEDs are powered by an off-

board supply and arranged radially in the direction of the five flexible appendages comprising the soft gripper design. The bottom of the biolayer is bonded to a silicone elastomer (Ecoflex 0030) embedded within a network of inflatable air chambers (Figure 3.3). These pneumatic channels are based on the pneu-net architecture previously used for actuation in limbed soft robot actuation and grippers (Figure 3.1B). Here, the pneu-net actuators control the ability of the gripper to conform to a specimen and exert contact pressure. For contact with soft materials, such as the isopropyl β-D-1-thiogalactopyranoside (IPTG)-infused hydrogel described below, such pressure is used to control the release of chemicals and their diffusion through porous membranes. The air pressure delivered to each pneu-net cell is independently controlled via syringes.

Establishing a flexible membrane system to retain cells while allowing for chemical sensing

The ability of the biosensing gripper to respond to chemical stimulation is evaluated based on the fluorescence intensities generated by synthetic bacteria. In order to allow sensing of chemical markers in an external environment, porous membranes are integrated into the system. These membranes enable the biolayer to retain the synthetic E. coli bacteria as they are exposed to chemicals in the surrounding fluid. Log phase chemical-sensitive bacteria are induced with IPTG and introduced into the embedded wells and then cultured for at least 4 hours. The resulting GFP intensities of the synthetic bacteria are measured using a laser scanner (Figure 3.5), yielding an approximately 500% increase in normalized fluorescence.

A critical part of the device design is the control of the interface between liquids

and synthetic bacteria. We test the device with polyethersulfone (PES) and polycarbonate track-etched (PCTE) membranes (*88*) as well as a porous PDMS-sodium bicarbonate membrane (*89*). The PES and PCTE membranes provide more uniform pore sizes and distributions, but lack elastomeric properties and optical transparency, properties which are achieved with the PDMS based membrane. All membranes contain pore sizes less than 0.5µm in diameter. This enables retention of E. coli bacteria while allowing the transport of chemical stimuli into the device from the external environment (Figure 3.5). These membranes retain the bacteria in the patterned wells of the PDMS biolayer. The permeability of each membrane is measured using IPTG-sensitive bacteria and fluorescence microspheres as controls to examine the effectiveness of each membrane. All three membrane materials demonstrate diffusion of fluorescent dye into the device wells, proving all three as viable components within the device design. Due to the position of the membrane relative to the pneu-net actuators, PES and PCTE membranes can be utilized in this device despite lacking elastomeric properties as they are located in the strain-limiting layer and are not required to stretch during the gripper motion.

Optical sensing and signal observation through embedded LEDs

The interaction between the synthetic bacteria and device is examined using an embedded LED circuit, which functions as both an excitation and an induction source. First, the bio-layer is filled with IPTG-induced E. coli, which has synthesized GFP. The GFP within the wells is then excited by the embedded LED circuit at 465nm and observed using filters and a wide-field stereomicroscope (Figure 3.6A, LED circuit removed from composite in image processing; raw images in Supplemental Methods
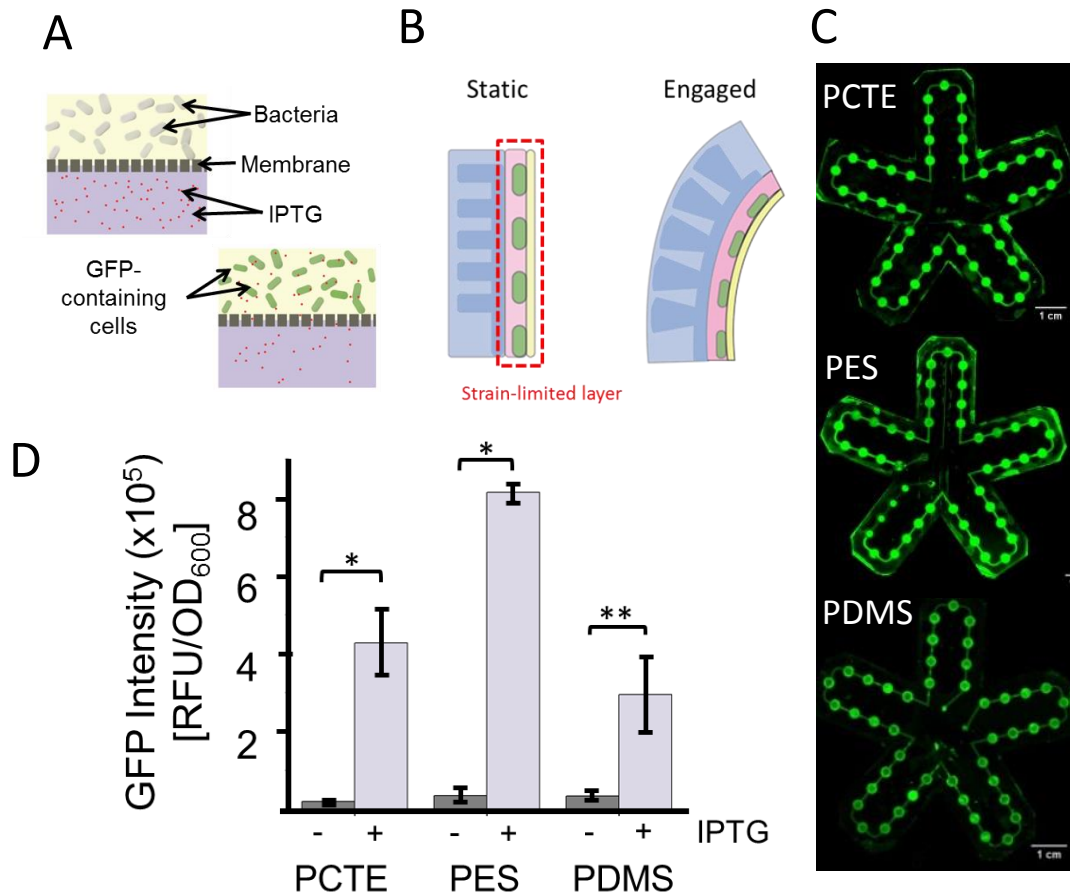
Figure 3.5 (A) The sealing membranes must possess pores capable of permitting chemical stimuli while rejecting bacteria to maintain biosensing capabilities. (B) Due to the membrane being bound on the strain limited layer, the membrane can deflect out of plane without tearing. (C) To have control over the engineered cell interface, various membrane compositions were integrated with the device and evaluated for permeability, including polycarbonate tracked-etched (PCTE), polyethersulfone (PES) and polydimethylsiloxane (PDMS); Scale bar, 2 cm. (D) The level of fluorescence expression due to IPTG permeation through each membrane (PCTE (n=3), PES (n=4) and PDMS(n=4)) was measured using a plate reader. Data represent three replicates and SEM (*$p<0.05$, **$p<0.10$).

and Figures S7, S8). Induced cells within the system produce a fluorescence expression level of approximately 400% of uninduced and unmodified E. coli (Figure 3.6B, Supplemental Methods and Fig. S7). While control over the chemical interface is important, optogenetic interfaces of this system provide multi-input controls. To

accomplish this, light-sensitive strains of E. coli are incubated in the device (Figure 3.6C). The repression of GFP production by the LEDs is measured and yields a decrease of ~19% in relative fluorescent intensity (Figure 3.6D), revealing the actuation component of our system through optical approaches.

Characterizing the soft robotic capabilities of the device

While the cellular interface allows us to control biological response, the ability for the system to be functional from a soft robotics perspective is essential in order to demonstrate the potential for full integration of the sub-modules. To accomplish this, we first measure the actuation of the soft gripper due to increasing pressures (Figure 3.8A) using motion tracking software and piezoelectric pressure sensors (Supplemental Methods and Figure S9). During the actuation of the appendages, the bacteria suspended in liquid media are retained within the wells despite the increase in pressure within the adjacent pneumatic channels (Supplementary Materials and Figure S10). Based on our design configuration, the wells and bacteria function as the strain-limiting layer, which is necessary for preferential bending in a pneu-net actuator (Figure 3.8B).
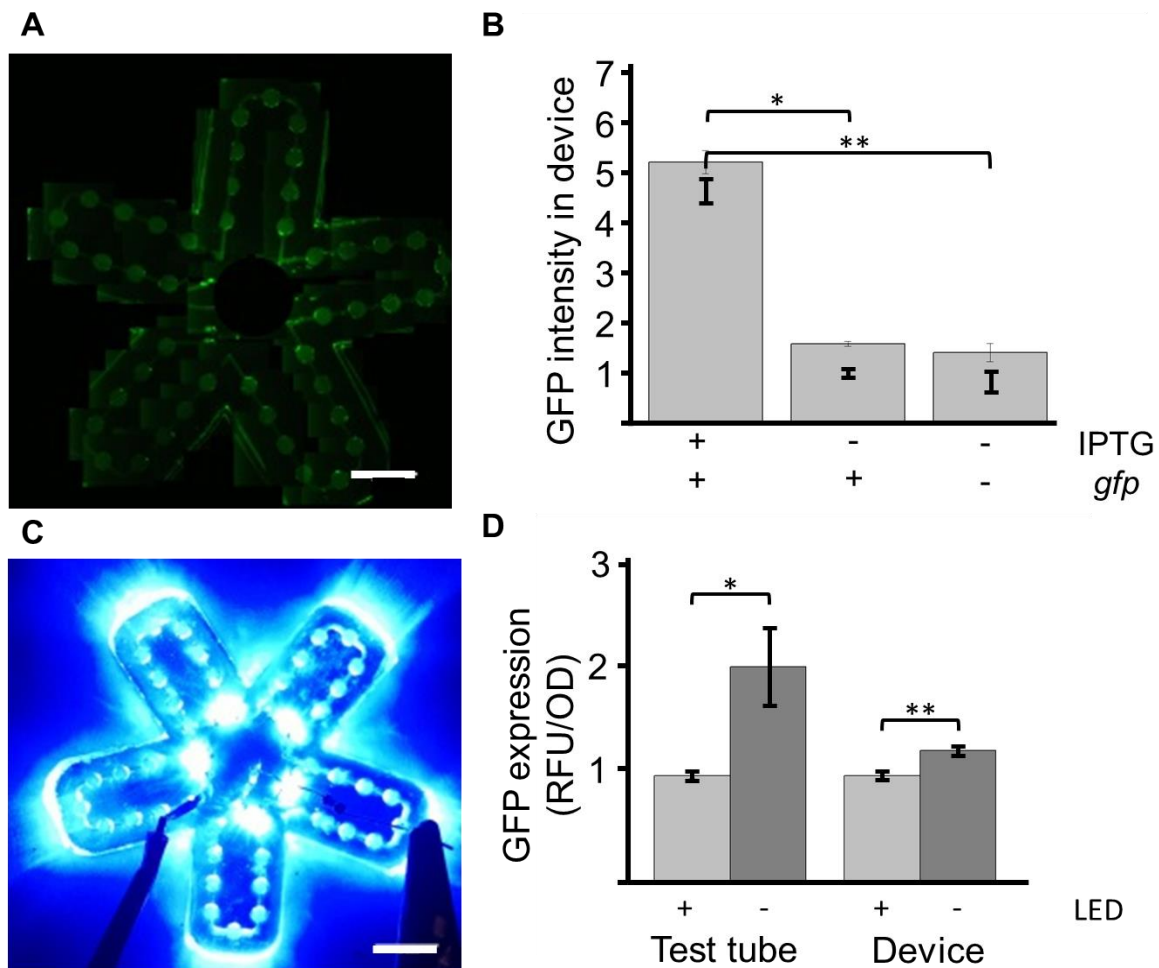
Figure 3.6 (A) Filtered signal of GFP(+) cells under LED excitation (B) Housed within the device, induced bacteria enable higher fluorescence intensities than uninduced and unmodified MG1655 E. coli. Data represent nine measurements and SEM (*$p<0.01$, **$p<0.01$). (C) The radial arrangement of the embedded LEDs enable optical repression of photo-sensitive synthetic cells in all patterned wells. Data represents 3 samples and SEM (*$p<0.05$, **$p<0.05$). (D) GFP expression is repressed by the LED within the device. Each error bar represents SEM of three replicates. See Supplemental Figure S1 for details on the genetic module.

Chemical sensing as part of a tactile gripping modality

Along with active control of the soft robotics platform, it is also essential to demonstrate
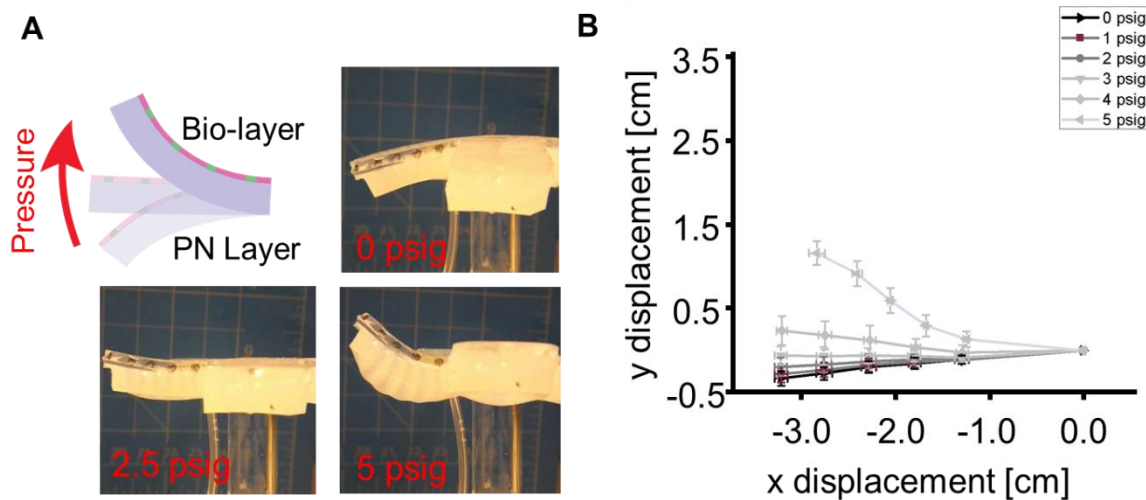
Figure 3.7 (A) The deflection of the device at varying pressures is characterized using video tracking software and piezoelectric pressure sensors. (B) The mechanical deformation due to the PN actuators is shown at varying pressures.

environmental-sensing functionality of the integrated cellular module. We examine the response of our designed sensing approach using a molded hydrogel infused with the chemical stimulus IPTG while submerged in a water bath (Figure 3.7A, B). The device is suspended via pneumatic tubing within an incubator at 30° C, and slowly lowered until the center of the device contacts the hydrogel. Next, the pressure in the pneu-net channels is increased to initiate contact between the membrane-sealed surface of the device and the submerged hydrogel. After 4 hours, the relative fluorescence intensities of the device interacting with an IPTG hydrogel are almost 300 times higher than negative controls lacking IPTG, performing as well as the bacteria in test tubes (Figure 3.7C). The results indicate that the chemo-sensing bacteria within the device are integrated to respond to environmental cues from external environments within our soft robotic system.

By integrating synthetic bacteria into a soft robotic system, we demonstrate the ability to
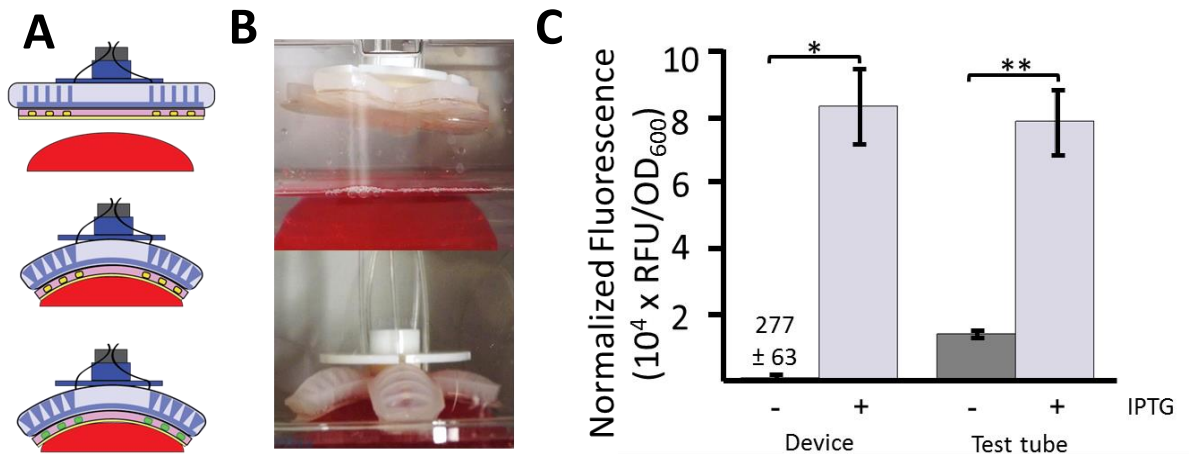
Figure 3.8 (A and B) The sensing capabilities of the device are evaluated in an aqueous environment and chemo-sensitive cells are utilized to determine the presence of IPTG in submerged hydrogels. (B) The device successfully distinguished between IPTG-infused and standard hydrogels, producing a higher normalized florescence ratio between the test and control than the same strains induced in test tubes. Data represent mean ± SEM for 3 separate experiments (*p<0.05, **p<0.05).

expand functionality of flexible devices through the utilization of existing biological architectures. The inclusion of synthetic bacteria as sensing mechanisms exploits the inherent abilities of biological systems to respond to a variety of stimuli at a low spatial cost. The combination of fluidic channels and wells with microfilter membranes allows for the retention of sensory bacteria, as well as the interaction between the synthetic cells and both chemical and optical cues. Along with broader materials selection, this fluidic functionality allows for a versatile and flexible device capable of engaging and responding to foreign objects in an aqueous environment. Future efforts will extend this work by incorporating soft robotic biosensing into human-compatible soft machines, expanding the chemo-optical sensing capability of the synthetic cells, and creating fluidic modules that maintain densities of synthetic cells.

Chapter 4 Magnetoliposomes

Introduction

Liposomes have long been in the conversation for drug delivery due to their ability to fuse into a cell's plasma membrane and deliver cargo to the cell's interior, which makes them ideal tools for drugs with low solubility or in instances of intracellular delivery. However, this propensity to fuse can become problematic in the delivery of drugs which require localized or timed release, as it may result in the wrong cells receiving the cargo or premature delivery. In the human gut, for instance, human cells are vastly outnumbered by bacteria and other organisms within the human microbiome, meaning that successful delivery to mammalian cells using liposomes is difficult. To improve the effectiveness of liposomes in these conditions, long-circulating liposomes are used in favor of conventional liposomes, which utilize polyethyleneglycol or monosialoganglioside components within their lipid bilayers to improve steric stability. By combining these components with ligands added to the liposome surface for specific cell targeting, we aim to demonstrate the successful anchoring of liposomes on a mammalian cell surface via ligand-receptor mechanisms while preventing membrane fusion. By doing this, we aim to form a foundation for targeted liposomal drug delivery with a controllable, timed release mechanism by integrating a magnetically activated liposome shearing system. This chapter will focus primarily on the methods currently existing to increase circulation time and inhibit membrane fusion of liposomes, as well as feature experimental work and plans for future work.
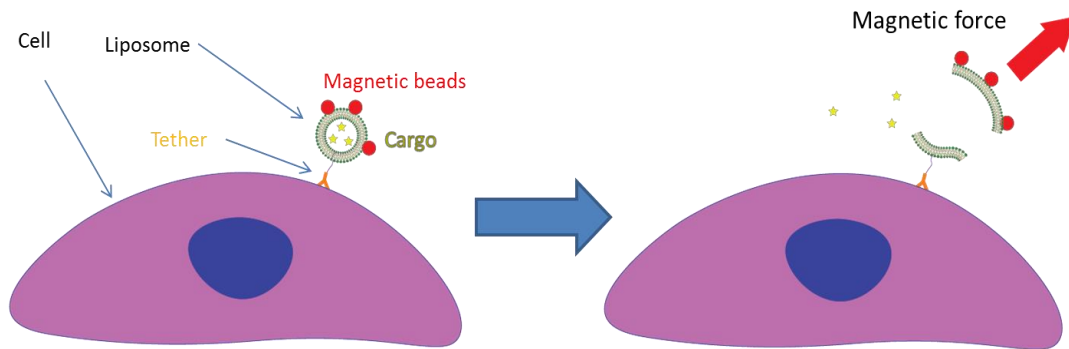
Figure 4.1 Schematic of magnetoliposome seeding on adherent mammalian before being ruptured due to application of magnetic force.

Background

Liposomes have been widely explored for applications as *in vivo* targeted drug delivery candidates due to their ability to encapsulate cargo that might otherwise be insoluble or unable to reach specific areas of the body by intravenous methods. In addition, the high degree of curvature present in lipid vesicles relative to that of a cellular plasma membrane leads to a high affinity for membrane fusion. This fusion provides an excellent means for delivering cargo into the cell. However, many cellular responses are dependent on external cues to receptor proteins which are then cascade signal transduction pathways to determine the ultimate cellular response. For these applications, it is important to deliver cargo to the immediate area surrounding a targeted cell type rather than bypassing the receptor proteins embedded in the plasma membrane via phagocytosis or membrane fusion. As such, we aim to utilize lipid vesicle technology to create a system capable of triggered release via magnetic force to deliver cargo to the apical surface of endothelial cells (Figure 4.1).

To achieve this, there are a few technical challenges which must be addressed. The first is the creation of a liposome design which does not leak its inner contents in physiological conditions. A second consideration is the development of a magnetic coupling system which allows for exerting a shearing force on the liposome to the point of rupture. Finally, the system must be capable of existing for prolonged periods after binding to the apical surface without undergoing membrane fusion or being phagocytosed.

The versatility of lipids and their collective behavior as part of lipid membrane systems is largely due to their amphipathic molecular structure. In living systems, the lipid populations of plasma membranes are composed primarily of phospholipids, which possess two fatty acid chains in their hydrophobic tail region and a phosphate-containing polar head group. This property along with the attraction between the hydrocarbon tail regions and repulsion forces between the polar heads results in self-assembly when introduced in aqueous media. The structures formed during self-assembly depend on a variety of factors, including the nature of the media, and the properties of the lipid with regards to the head group such as size and charge as well as the length of the tail chains and the saturation number. For aqueous media, some of these properties can be used to determine the critical packing parameter, or CPP, which can predict the structures of self-assembly for a given lipid. The CPP is defined according to the relation

$$CPP = \frac{V_c}{a_o l_c} \qquad (3.1)$$

where V_c is the effective volume occupied by the tail chains, l_c is the length of the tail chains and a_o is the effective area of the head group. These parameters are typically

Drying

Dispersion

Purification
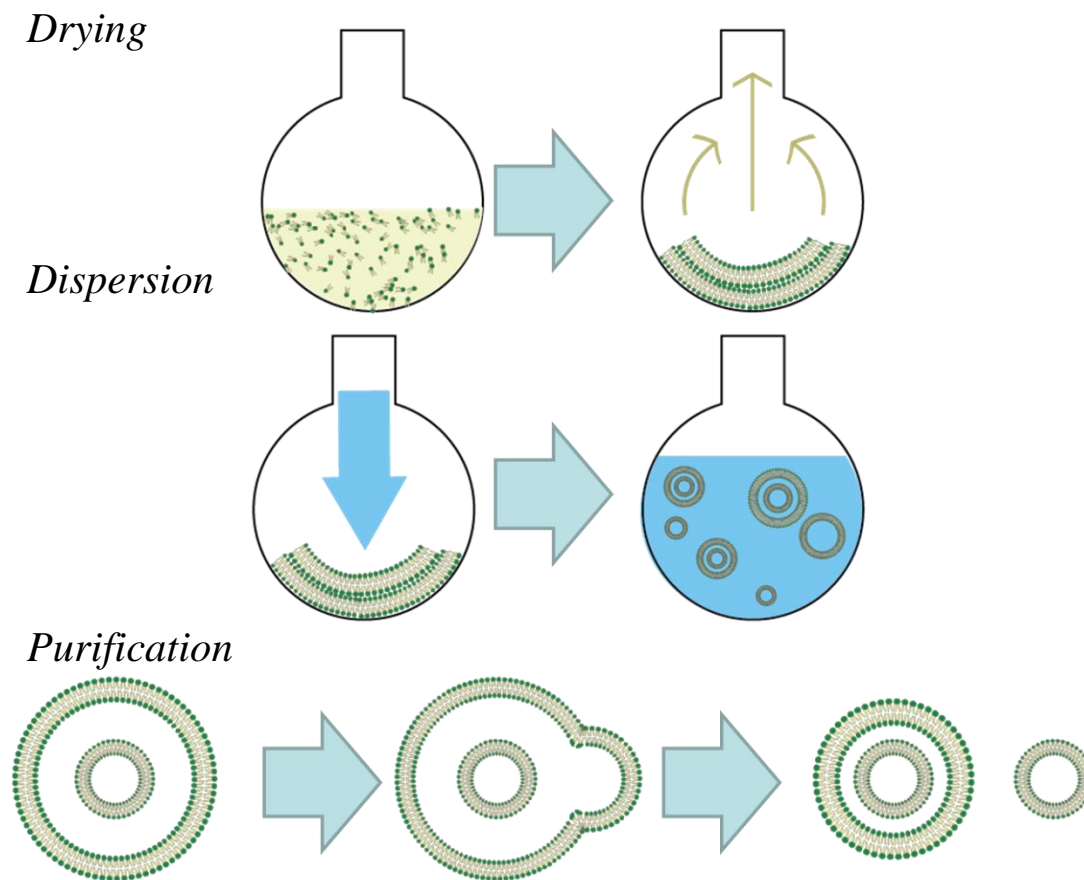
Figure 4.2 Outline of the steps in a traditional thin film hydration liposome protocol

found experimentally using X-ray scattering approaches (*90-93*). For lipids with a CPP between 0.5 and 1, the mode of self-assembly will be that of a liposome, a bilayer membrane enclosed in a spherical shape.

Liposome production

Liposomes can be further classified into a broad collection of lipid bilayer vesicles which are classified in a variety of ways, including size, preparation method or lamellarity. Because of the varying applications and desired characteristics for each, a number of protocols have been developed for forming liposomes. These protocols can vary in
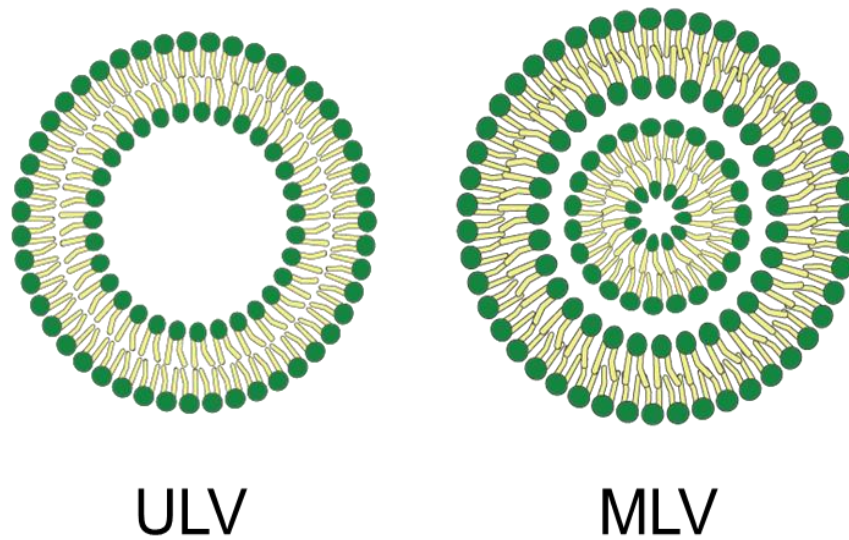
Figure 4.3 General representation of a unilamellar vesicle (ULV) and a multilamellar vesicle (MLV).

regards to materials and methods but almost all of them can be broadly divided into a few main steps with regards to the underlying physical phenomena: *Drying, Dispersion, Purification* and *Analysis* (Figure 4.2).

The drying stage involves first suspending the desired lipids in an organic solvent, typically chloroform or a chloroform-methanol mixture. This is done to ensure a homogenous mixture of the lipids. The mixture is then dried by use of a rotary evaporator or a vacuum line to form ordered lipid bilayer films at the base of the glass container. Because of the amphipathic nature of the lipid molecules, they form ordered bilayer structures as the organic solvent is evaporated away owing to the mutual attraction between the head groups as well as the tail groups. The establishment of this ordered bilayer is essential for high yield of liposomes rather than micelles, and is easily achievable with traditional laboratory equipment. Alternative methods of liposome

formation include establishing an ordered lipid bilayer involve the self-assembly of lipids at the fluid interface of dissimilar liquids from which to extrude liposomes (*94, 95*).

Following the drying stage comes the dispersion stage which requires the rehydration of the lipid cake with a polar, typically aqueous, solution. Owing to the hydrophobicity of the tail region in the lipid bilayer film, the suspended films will self-assemble into spherical vesicles to minimize the free energy of the system, with inner and outer leaflets of lipids arranged to shield the hydrophobic tail groups from the polar solvent. A simple form of agitation is typically applied during the dispersion process to promote the formation of lipid vesicles. Due to the stochasticity of the procedure, the most common result is a population of liposomes dominated by multi-lamellar vesicles (MLVs), which are vesicles comprised of multiple lipid bilayers arranged in onion-like fashion (Figure 4.3). For most applications, single lamellar vesicles are desired, so some type of purification process is required.

There are many existing methods of purifying unilameller liposomes to the desired size distributions, which are generally defined as small unilamellar vesicles (SUVs), large unilamellar vesicles (LUVs) and giant unilamellar vesicles (GUVs), plus a few intermediary classifications. SUVs typically range from 15-30nm in diameter, LUVs can be greater than 100nm while GUVs are on the order of microns. Common methods for purifying liposome populations include extrusion and sonication. The process of extrusion simply involves pressurizing liposome mixtures and forcing them through filters with pore sizes roughly equivalent to the desired vesicle diameter (*96*). The method of sonication is typically used for creating SUVs and can be accomplished with either probe or bath sonicators (*97*). That being said, bath sonicators are often preferred

owing to a few drawbacks of probe sonicators with regards to liposome preparation. For instance, probe sonicators can contaminate liposome samples as metallic debris from the probe tip can find its way into solution. Additionally, the use of a probe sonicator results in localized heating, resulting in a heterogenous size distribution.

Due to the versatility of lipid vesicles and related technologies, the methods for analyzing performance can vary greatly depending on application. However, one common method to evaluate liposome performance is by characterizing cargo retention. This is typically performed by measuring the rate at which a fluorescent dye, such as calcein, can diffuse out of the liposome into a surrounding environment (*98*). The encapsulation and retention efficiency of liposomes is largely dependent on the lipids used and the temperatures at which they are implemented, but it can be improved with a number of different techniques.

Calcein has been used in this work as an indicator of retention and rupture of the liposomes, though other fluorescent probes have been employed as well, such as BODIPY non-polar fluorophores, which serve to image the lipid bilayer rather than the encapsulated cargo. A further advantage of calcein is the self-quenching phenomenon which occurs beyond 60 uM concentrations. By creating liposomes which retain calcein concentrations slightly beyond this threshold, it is possible of achieve a brief flare of fluorescence in the instance of a rupture.
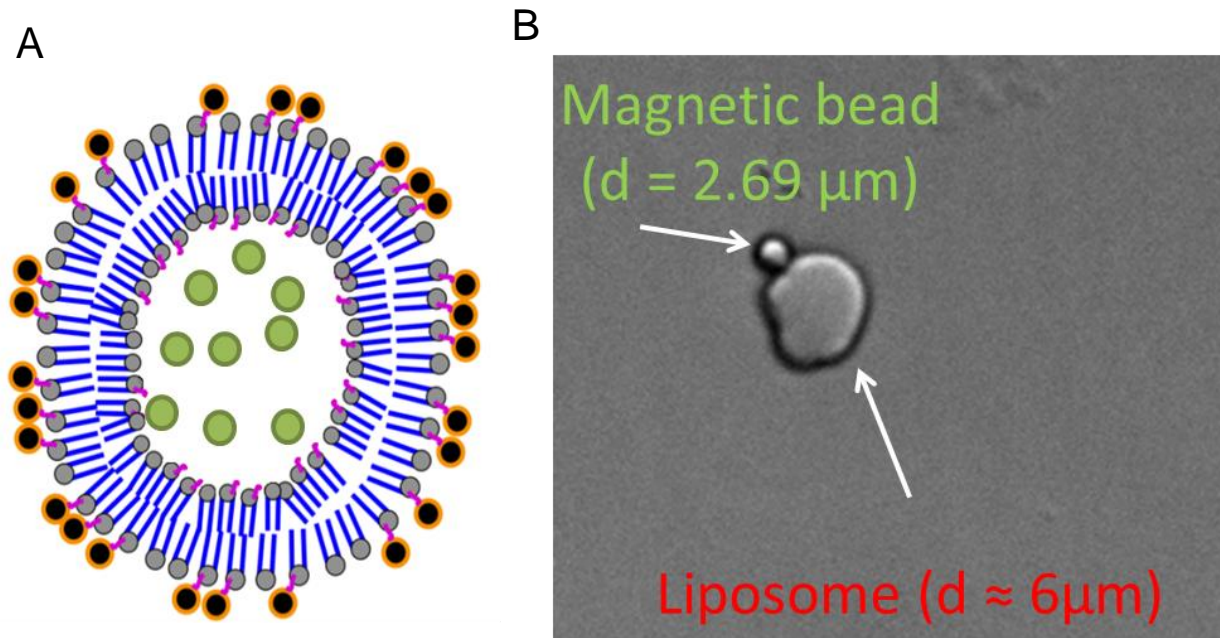
Figure 4.4 (A) Schematic of a liposome encapsulating fluorescent cargo (calcein) with magnetic beads bound to biotinylated lipid heads. (B) Brightfield image of a fixed liposome with a streptavidin coated magnetic bead bound to it via biotinylated lipid head.

Lipid selection

As mentioned previously, lipids found in cell membranes are typically phospholipids which possess polar head groups and hydrophobic fatty acid tail regions. The four most common of these phospholipid head groups are phosphatidylcholine (PC), phosphatidylserine (PS), phosphatidylinositol (*99*) and phosphatidylethanolamine (PE), which each possess unique properties with regards to head charge and size. Similarly, there are a number of commonly occurring fatty acid chains which typically range between 16 and 18 hydrocarbon chains, such as palmitic and oleic acid. These head and tail groups can be combined in a variety of ways to the result of modifying behavioral properties such as CPP. For instance, dipalmitoylphosphatidylcholine

(DPPC) and 1-Palmitoyl-2-oleoylphosphatidylcholine (POPC) vary only by one fatty acid chain, but this variation is significant enough to result in two different self-assembly modes (ie. micelles versus liposomes) as well as a difference in gel-liquid transition temperatures of 43°C. Additionally, by using mixtures of lipid types and varying the respective concentrations, one can tune overall membrane properties accordingly (*91*). Owing to the versatility of lipid vesicle technologies, a wide variety of lipids outside of standard phospholipids can be designed for varying applications. Common manifestations include fluorescently tagged lipid and ligand-modified head groups, as well as polymer grafted lipid heads (*100, 101*). For instance, biotinylated lipids allow the targeted binding of complementary beads or functional molecules. Magnetic beads coated in streptavidin were attached to the liposome construct using this binding strategy (Figure 4.4).

Creating and modeling localized magnetic gradients within a Helmholtz coil microscopy stage

Magnetic tweezers are a common tool in biomedical and biophysical research applications which allow for controllable and reproducible forces to be exerted on targeted cells or biomolecules through an intermediary paramagnetic bead or particle bound to the article of interest. There are multiple established methods to create magnetic tweezers, typically involving permanent magnets or magnetically permeable materials placed within an electromagnet arrangement. Magnetic tweezers are especially effective in biological capacities as most biological matter is neither ferro- or

para-magnetic. As such, it is possible to achieve localized force application through use of modified magnetic beads. Specifically, we can device a system for magnetic tensile cytometry to exert relatively high forces on beads attached to biological materials of interest by introducing a concentrated magnetic field near a paramagnetic bead.

To do this, we must first develop a basic understanding of the underlying physical phenomena related to this technique. While the equations governing the arrangement of the magnetic field $\vec{B}$ are quite complicated, we can define the magnetic force F_{mag} on the bead as a function of $\vec{B}$ and the magnetization of the bead m. This relationship is given as

$$\vec{F}_{mag} = \left(m(\vec{B}) \cdot \nabla\right)\vec{B} \qquad (3.2)$$

However, even with this relationship, developing an accurate model for a given magnetic set-up can still prove challenging. Without use of computational software, it is necessary to measure the magnetic force being applied to the bead experimentally, which can be tedious and inaccurate due to the magnetic force being inversely proportional to distance between a bead and the magnetic source, leading to a large degree of sensitivity that is difficult to capture. This measurement is typically performed with beads subjected to a magnetic field within a viscous liquid media and allowed to reach a terminal velocity due to viscous drag forces. Once this velocity is reached and net acceleration is zero, we can equate the viscous drag force to the magnetic force applied to the bead. For a spherical bead, the drag force is given as

$$F_{drag} = 6\pi\mu RV \hspace{3cm} (3.3)$$

where μ is the dynamic viscosity of the surrounding fluid, *R* is the radius of the bead and *V* is the velocity of the bead. By calculating this drag force, we can gain better insight into the capabilities of our magnetic tweezers. However, as mentioned previously, this method is time-intensive and provides only a small window of insight into the magnetic field. Additionally, a current application of interest is in the creation of a high-throughput magnetic tweezers system embedded within a microfluidic chip system and placed under a constant magnetic field induced by a Helmholtz coil apparatus (Figure 4.5A)(*102, 103*). By using laser patterning to cut complex shapes into magnetic mu-metal, we can create a series of local magnetic potential gradients along the length of a channel due to the relative permeability between the mu metal and the surrounding materials (Figure 4.5B). However, the design of these magnetic inserts would be greatly aided through the use of computational software to visualize the resulting magnetic fields and the achievable force magnitudes.

This principle is dependent on the creation of a magnetic field gradient in the vicinity of the bead such that the magnetic potential difference induces a force. A common way to achieve this is to use a material with a high magnetic permeability featuring a tapered geometry or fine point (i.e. paramagnetic needle). In order to achieve this effect in a high-throughput system, we have combined laser patterned mu-metal with a microfluidic chip to allow live imaging of a series of magnetic tweezers.

An important consideration of this approach is the understanding of how the geometry of the laser-patterned metal impacts the local magnetic fields and subsequent magnetic

forces capable within the chip. To do this, one must first establish an understanding of the underlying physics of electromagnetism, which are founded in Maxwell's equations, which are given by

$$\nabla \cdot \boldsymbol{E} = \rho/\epsilon_o \qquad (3.4)$$

$$\nabla \cdot \boldsymbol{B} = 0 \qquad (3.5)$$

$$\nabla \times \boldsymbol{E} = -\frac{\partial \boldsymbol{B}}{\partial t} \qquad (3.6)$$

$$\nabla \times \boldsymbol{B} = \mu_o \boldsymbol{J} + \mu_o \epsilon_o \frac{\partial \boldsymbol{E}}{\partial t} \qquad (3.7)$$

In these relationships, E is the total electric field, B is the total magnetic field, rho is the electric charge density, J is the electric current density, ϵ_o is the permittivity of free space and μ_o is the permeability of free space. Due to the complexity of these relationships, computational programs are typically used for solving the equations in a given environment. For our purposes, we will be examining thin metallic foils in relatively constant magnetic fields produced by Helmholtz coils. In these relationships, μ is magnetic permeability, ϵ is permittivity and σ is conductivity. Following this, a number of different approaches can be employed depending on the nature of the problem, including discrete dipole approximation, fast multipole method (FMM), and partial element equivalent circuit (PEEC). In the case of magnetostatics, there are multiple methods to approach the problem offered within MATLAB. The focus of this project will be to analyze the capabilities of the PDE Toolbox in comparison with a customized FEM model of the system within MATLAB.
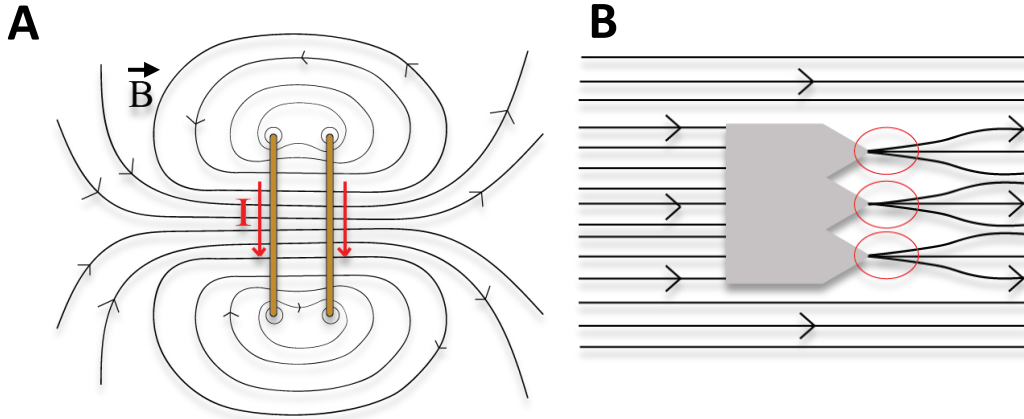
Figure 4.5 (A) Magnetic field induced by Helmholtz coils produces a region of relatively uniform magnetic potential due to current I in the two coils. (B) A patterned material of high relative magnetic permeability distorts the surrounding magnetic potential field, leading to local gradients at acute features.

The computation of magnetic field potential due to varying magnetic permeabilities can be approached under the assumptions of magnetostatics. As such, we only require two of Maxwell's equations, specifically Gauss's law for magnetism (3.5) and Ampere's law (3.7). While Gauss's law is unaffected by the assumption of magnetostatics, Ampere's law can be simplified to the following form by removing the time-dependent derivative:

$$\nabla \times \boldsymbol{H} = \boldsymbol{J} \qquad\qquad (3.8)$$

In this representation, H represents the magnetic field intensity and J the current density. In our model system, the current source will be represented by two rectangular regions representing cross sections of Helmholtz coils with current going into and out of the plane in equal magnitudes (shown as regions R3 and R4 in Figure 4.6A). Positioned between the two coil cross sections is the patterned mu metal foil which comprises a

A

B
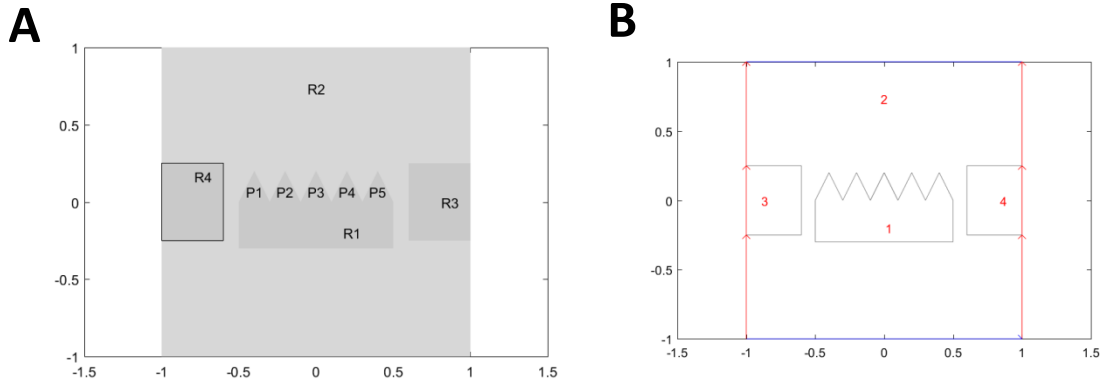
Figure 4.6 (A) Shapes created using the PDE Toolbox. (B) Regions created within the PDE Toolbox after removing interior boundaries to produce four distinct regions.

rectangle with a saw-tooth edge. The features are contained within a surrounding domain (R2), which is represented by air in this arrangement.

Because this problem is a magnetostatic one, the magnetic field B can be determined using the Biot-Savart law without fear of violating either Ampere's law and Gauss's law for magnetism. The Biot-Savart law is shown as follows.

$$\boldsymbol{B}(\boldsymbol{r}) = \frac{\mu_0}{4\pi} I \int_C \frac{d\boldsymbol{l} \times \hat{r}'}{|r'|^2} \tag{3.10}$$

For well-defined geometries, this relationship can be solved analytically to produced governing equations, but in cases of complex geometries such as this, a computational approach is preferable, which requires a discretized form. This discretized form must be calculated for a large quantity of discrete nodes across a predefined planar mesh. This can be done using the PDE Toolbox in MATLAB which we will employ to model the magnetostatic problem. A basic geometry consisting of five isosceles triangles patterned above a rectangle in a sawtooth configuration will be used as the comparative condition, the construction of which is detailed in attached code.
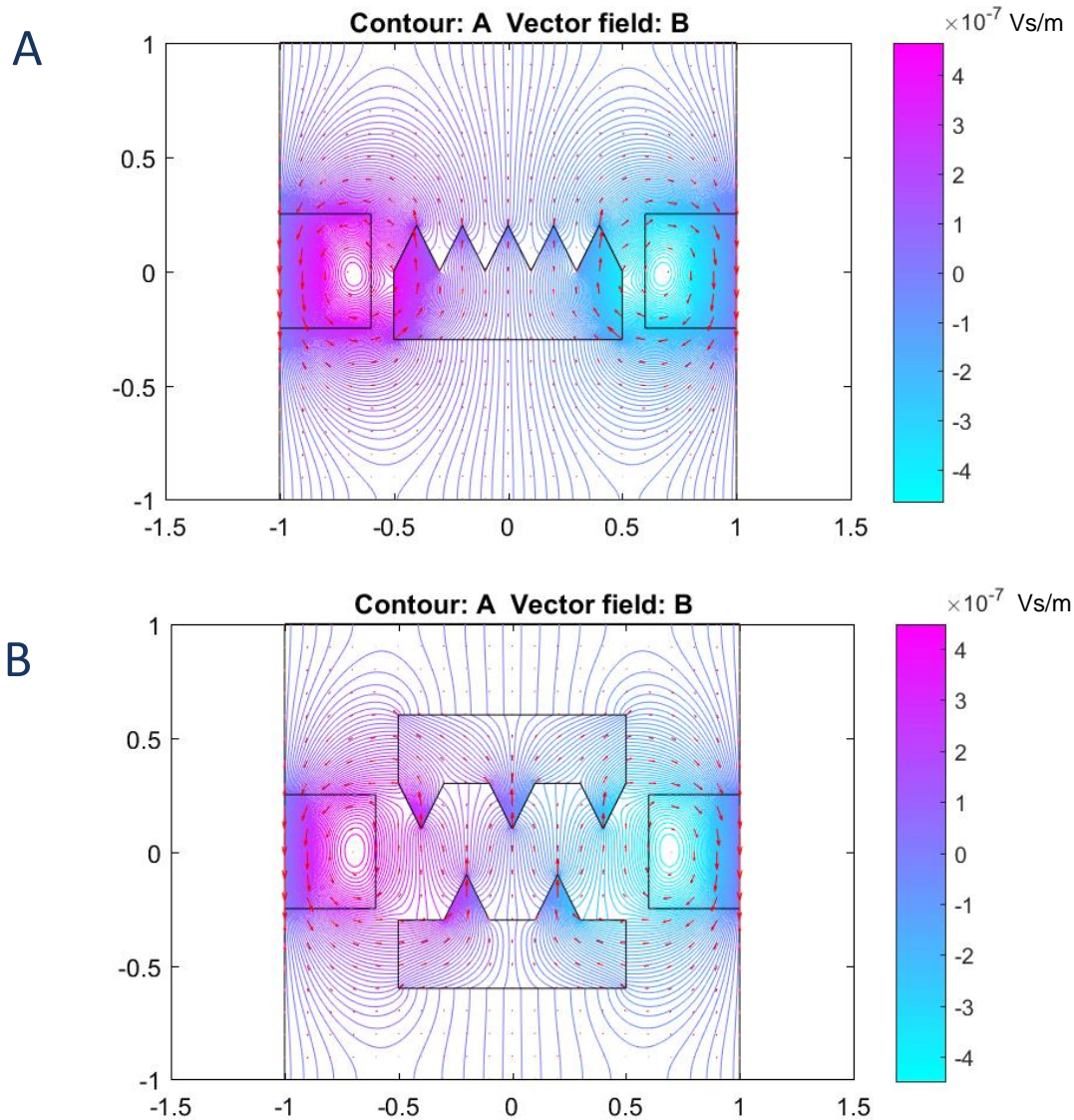
Figure 4.7 (A) Magnetic potential field and vectors of mu metal within activated Helmholtz coil. (B) Magnetic potential vectors of two patterned mu metal inserts featuring interlocking teeth within the Helmholtz coil arrangement

The mu-metal foil is shown centrally within the figure and is flanked by two rectangles to represent the Helmholtz coils which work to induce a magnetic field in the vicinity of the foil.

The application of the aforementioned code within the PDE Toolbox yields the 9 overlapping shapes which can be appropriately joined by deleting interior boundaries (Figure 4.6A). Once the interior boundaries are deleted, we are left with 4 distinct

regions: the mu-metal foil, two Helmholtz coil cross sections and the surrounding air (Figure 4.6B)

Once the appropriate shapes were imported into the PDE Toolbox GUI, the appropriate interior subdomain boundaries were removed and boundary conditions were applied to the outer edges of the domain. Specifically, a Dirichlet boundary assumption was on the lateral edges of the domain (represented with red lines), while a Neumann boundary assumption was applied to the top and bottom domain boundaries, shown in the figure with blue lines. The Dirichlet boundary given is governed by the relationship *h*A = r,* where *h = 1* and *r = 0* and represent weight and magnetic potential respectively. Alternatively, the Neumann boundary condition is given by

$$n\frac{1}{\mu}\nabla A + q = g \qquad (3.11)$$

where g represents the magnetic field and is set to zero. Using the Magnetostatics application mode, the distinct subdomains of the Helmholtz coils, magnetic foil and air were assigned values for their magnetic permeabilities and current densities. As copper and air have similar magnetic permeabilities, the Helmholtz coils and the air domains both were assigned to equal $4\pi x 10^{-7}$ H/m while the current density of air was set to zero. The current densities of the coil were set to 10 and -10 J/m^2 for the left and right regions to represent the direction of the current either in or out of the plane. Lastly, the current density of the magnetic foil was set to zero while the magnetic permeability was given by the following relationship

$$\mu = 4\pi \times 10^{-7}(\frac{\mu_{max}}{(1+c\|\nabla A\|^2)} + \mu_{min}) \qquad (3.12)$$

This result was simplified to read $\mu = 4\pi \times 10^{-7}(\frac{50000}{(1+0.05(ux^2+uy^2))} + 10000)$ within the

PDE Toolbox. Once the appropriate PDEs were set for all domains, the mesh was

initialized and refined three times to yield the following result.

Following the generation of the mesh, the PDE Solver was initiated and computed the

magnetic field lines within the domain. By editing the plotting preferences, a plot

containing both contour and vector lines was produced and is seen in Figure 4.7.

Magnetic channel design

Initially, the concept of flanking microfluidic channels with patterned magnetically

permeable structures was tested with microfluidic channels in which to flow molten

solder. The channels were fabricated using traditional soft lithography on silicon wafers

before the pattern was transferred to PDMS. The PDMS channel was then punched

with flat-tipped needles and sealed with a glass cover slip using plasma oxidation.

Following the construction of the channel, it was placed on a hot plate at 190 °C for 10

minutes to reach temperature. Solid solder wire was then fed into the patterned auxiliary

channel in contact with the glass bottom. The high temperature of the channel caused

the solder to liquefy and flow through to the channel outlet. However, owing to the

viscosity of the liquid solder and the formation of an oxide layer on the liquid, it proved

difficult to fill acute features within the channel. Frequently air pockets were formed at

the pivotal location of the pattern, resulting in a rounded tip rather than a pronounced

metallic feature, reducing the effectiveness with regards to local magnetic potential

gradients (Figure 4.8A). For improved workability, the injection of eutectic gallium

indium (EGaIn), which is liquid at room temperature, was attempted. The material showed improved flow characteristics and removed the necessity for a hot plate, but still proved unable to reliably fill the fine tips within the patterened channels due to the entrapment of air pockets during fluid flow (Figure 4.8B). While this two-phase flow problem might be remedied if performed in a low-pressure glove box, it was decided to pursue other avenues which might enable the use of more magnetically permeable materials than solder and EGaIn while also improving the ease of fabrication.
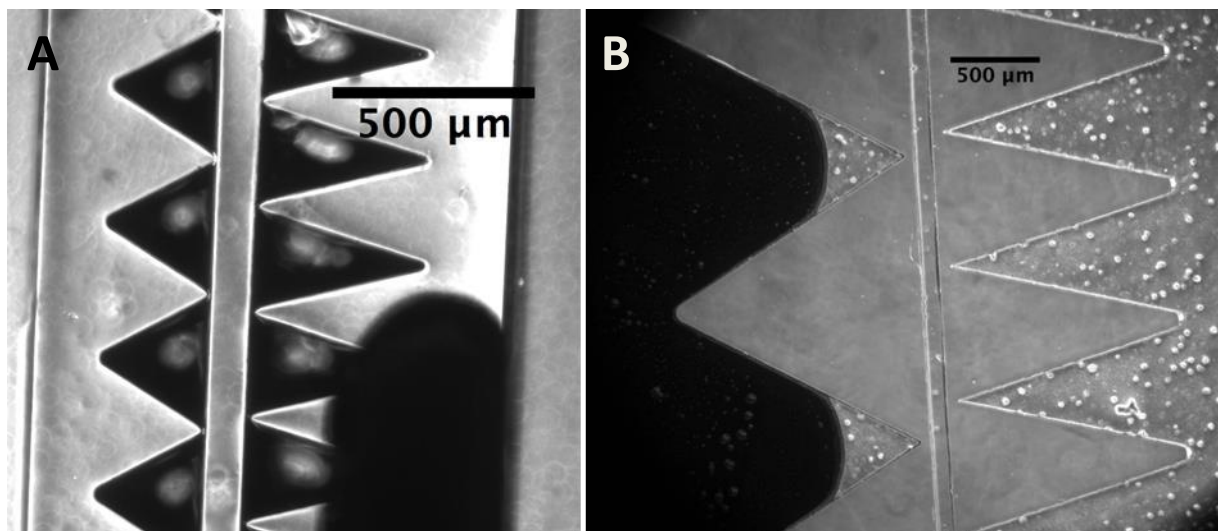
Figure 4.8 *(A) Bright-field image of attempted flow of solder into patterned channels flanking a central microfluidic channel. (B) Bright-field image of EGaIn within a patterned channel. In both cases, the metallic material was unable to completely fill the chamber, specifically in the patterned tips.*

Laser-patterning mu-metal foil

Utilizing the insight gained from modeling the magnetostatic problem in the MATLAB PDE Toolbox, it is possible to create a number of designs capable of producing local magnetic field gradients. To maximize the potential of this application, it is necessary to

A
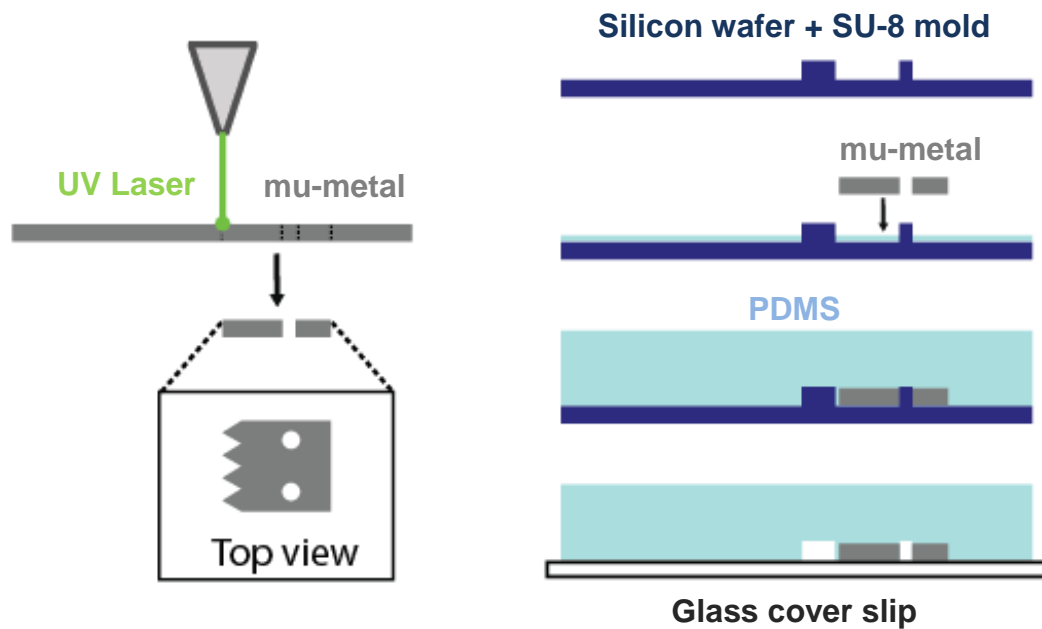
B
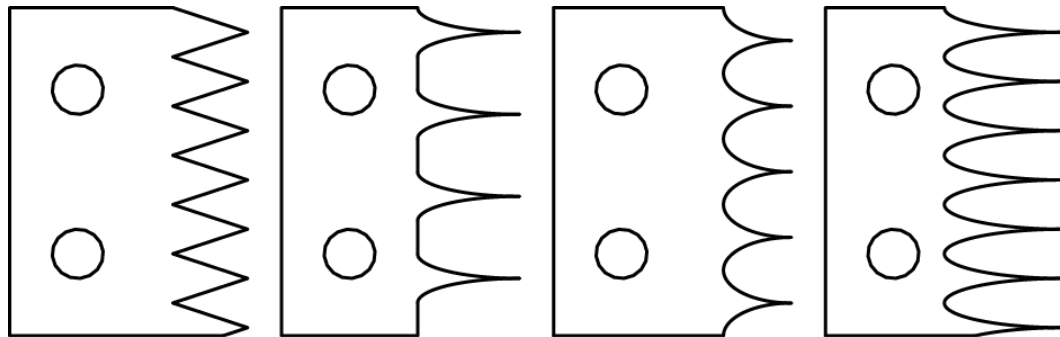
Figure 4.9 (A) Schematic of the magnetic tensile cytometry (MTC) channel produced using a combination of laser cutting and soft lithography processes. (B) Primary mu-metal patterns tested within the MTC channel to evaluate design features.

select a material with a high relative magnetic permeability. For this application, mu-metal foil sheets with a thickness of approximately 50 µm were purchased to be integrated within the device. Four designs were created with varying features to evaluate the most effective design aspects, specifically the depth of the protrusions, the separation of the protrusions and straight versus chamfered edges leading to magnetic tips. These designs all feature two holes within the body of the structure for alignment
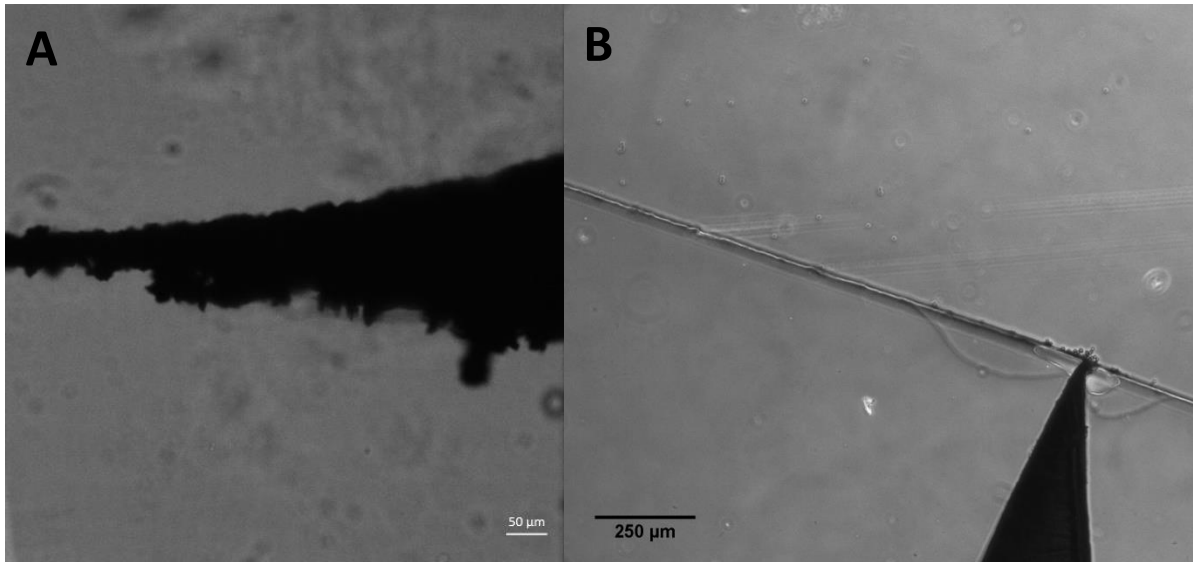
Figure 4.10 (A) Bright-field image of edge produced by high power, lower frequency cutting settings using UV laser cutting. (B) Bright-field image of ideal clean edge produced through low power, high frequency and varying mark separation settings.

purposes (Figure 4.9). On the silicon mold featuring the microchannel, there are corresponding posts to ensure the magnetic structure is always placed at a constant distance from the channel and does not drift while the surrounding PDMS is curing. These designs were created in SolidWorks and imported as paths into a UV laser cutting platform. Because of the material properties of the nickel-iron mu-metal alloy as well as the thickness of the foil, it is pivotal to take multiple passes with the UV laser at varying high frequencies, low powers and fast marking speeds to avoid the formation of a rough edge as seen in Figure 4.10. When these principles are applied within the LPKF, it is possible to achieve a much smoother feature when laser patterning the foil. Once the mu-metal was successfully cut using the UV laser, a thin layer of PDMS was applied to the silicon channel mold via spin coating at approximately 3000 rpm. This was performed to prevent air pocket formation beneath the magnetic structures which would result in drifting during the degassing of the prepolymer. Once the magnetic

structures were put in place using the post alignment feature, additional PDMS prepolymer was poured carefully over the channel mold. The system is then degassed under vacuum pump for 45 minutes before final verification of the positioning of the magnetic inserts. The PDMS was then cured in an oven at 60 °C for 2 hours and then the channels were carefully removed using an X-acto knife and straight edge razor. Following the removal of the PDMS, the inlet and outlets were punched using a flat-tip needle and the channel was bonded to a glass slide via plasma oxidation.
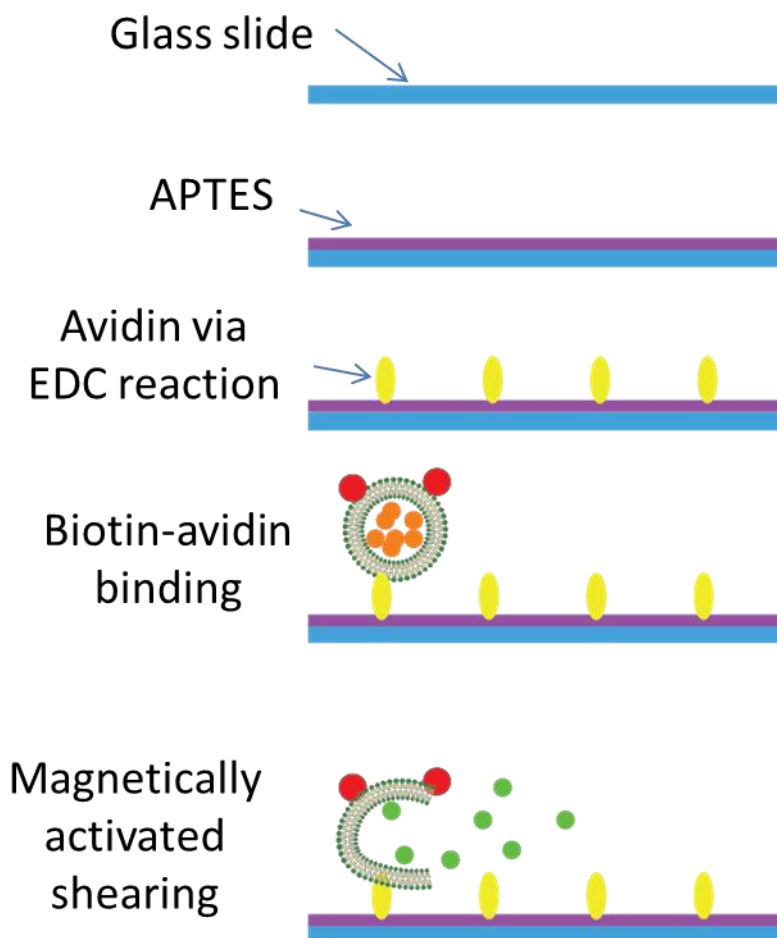
Figure 4.11 Schematic of the avidin coating process for anchoring liposomes before magnetic testing for rupture
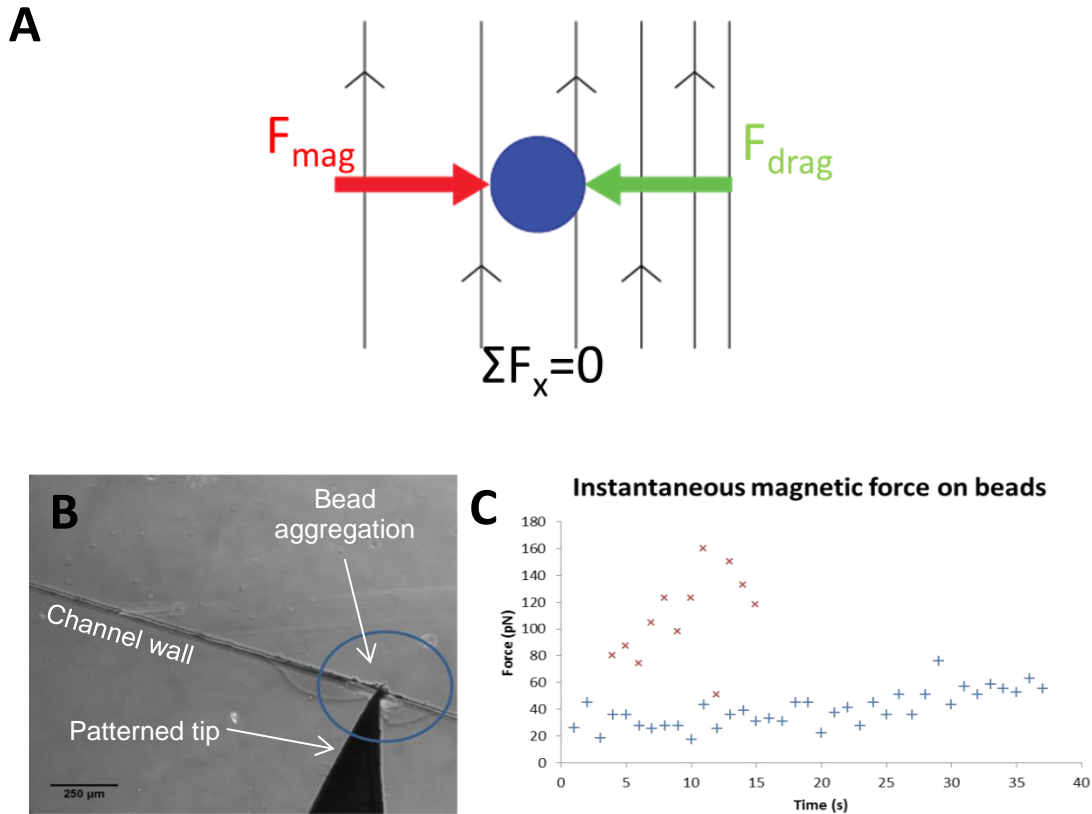
Figure 4.12 (A) Force balance of the terminal velocity state when the drag force is equal to the magnetic force used to determine the magnitude of the magnetic force capabilities via particle tracing. (B) Aggregation of beads near the mu-metal tip within the channel after magnetic activation. (C) Instantaneous force measurements for two beads subjected to magnetic forces through magnetic field distortion within the MTC channel

Avidin-coating channels

Once the channels featuring the metallic inserts were bonded to glass slides via plasma oxidation, an anchoring mechanism with which to seed the magnetoliposomes was needed such that the vesicles could be placed under tension upon exertion of a magnetic force. To do this, the glass surface within the channel was treated with 6% (3-

aminopropyl)triethoxysilane (APTES) for 15 minutes to deposit functional silane groups along the length of the channel (*104*). This silane group was then used as a binding site for an 1-ethyl-3-(3-dimethylaminopropyl)carbodiimide hydrochloride (*105*) reaction with avidin protein over the course of 2 hours (Figure 4.11). The surface was then blocked with casein to prevent non-specific binding and the liposomes were seeded by flowing into the channel then remaining static for 30 minutes before a wash step with PBS.
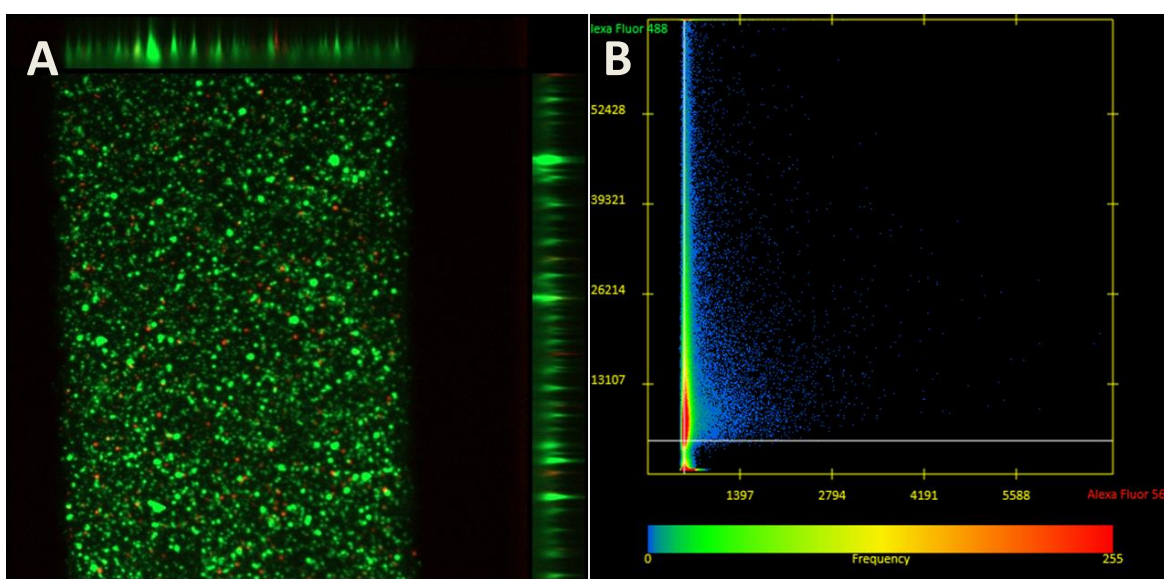
Figure 4.13 (A) Orthogonal view of liposomes bound to avidin coated glass within a microfluidic green with red fluorescent beads bound to biotinylated lipid heads. (B) Colocalization result of the seeded liposomes with red fluorescent beads bound showing the positional relationship between red beads and green liposomes.

Testing magnetic capabilities

In order to characterize the capabilities of the magnetic microfluidic chip, it was necessary to determine the magnetic force achievable upon the magnetic beads to be used in our designs. Streptavidin coated magnetic beads measuring 2.69 μm in diameter were suspended in glycerol for additional viscous drag before being placed

within the channels. Using bright field microscopy, the velocity of the magnetic beads was tracked in the vicinity of the patterned metallic tips under the magnetic field induced by the Helmholtz coil microscopy set-up. Using the quasi-equilibrium assumption outlined earlier where the beads reach a terminal velocity and the viscous drag force is equivalent to the magnetic force, the magnetic force was determined experimentally (Figure 4.12A) (*106*). From these experiments, it was found that the magnetic chip is capable of exerting forces greater than 100 pN per bead for certain patterns, suggesting that rupturing liposomes is achievable with this set-up (Figure 4.12B and C).

Rupturing the lipid membrane to release cargo

In order to rupture liposomes in this set-up, it is necessary to combine the avidin-coating procedure and the magnetic field induced by the Helmholtz coil. By doing this, we can put the liposomes in tension by fixing them at a location within the channel and then applying a magnetic force through the introduction of local magnetic potential gradients. However, the application presents some challenging obstacles. First, the magnitude of the magnetic force achievable is highly dependent on the distance between the bead and the patterned tip. When experimenting with beads in glycerol, the maximum distance across which the magnetic force is capable of is roughly 200 µm. However, at the maximum distance, the magnitude of the force is greatly reduced.

Secondly, adhering streptavidin coated magnetic beads to the liposomes via biotinylated lipid heads can prove challenging or disadvantageous in some regards. Because of the limited binding sites and steric interactions, it is very difficult to achieve at least one bead bound to every liposome. It is possible to seed the liposomes upon

the avidin-coated channel bottom and then flow beads in over the liposomes, but some beads become entrapped in the avidin rather than bound to the biotinylated lipid heads while some liposomes are left without beads bound to them (Figure 4.13A and B). To combat this, blocking with casein has been attempted to prevent non-specific interactions between the streptavidin coated beads and the avidin but the procedure requires additional refinement before establishing the effectiveness of the method. Once a protocol has been successfully developed where beads can reproducibly be bound to seeded liposomes in a consistent manner, testing for rupture capabilities will commence.

Membrane fusion

Owing to the nature of phospholipids and their propensity to self-assemble because of the attraction between their tail groups and repulsion between their head groups, there are a number of considerations one must take in the design of a system to resist the physical phenomena of membrane fusion. For liposomes specifically, a major determinant in the storage time is the rate at which liposomes will fuse with one another to form larger, multilamellar structures. This fusion can occur below the phase transition temperature, making long-term liposomal storage of sensitive cargo, such as biological enzymes, particularly difficult. A number of techniques have been developed to reduce this effect and prolong the time which a liposomes can sit at low temperatures inertly, which will be discussed later in this review. Beforehand, however, it is important to outline the underlying energetics associated with membrane fusion.

As the formation of lipid bilayers is a product of the hydrophobic effect, so too is membrane fusion, as the goal of the system is to minimize solvent-exposed non-polar surfaces (*107-109*). In the case of liposomes, the high-degree of curvature associated with their lipid bilayers is not energetically favorable with regards to the hydrophobic effect. Therefore, there is a propensity to decrease the degree of curvature and fuse with other lipid structures to reduce the overall curvature. However, for this fusion to occur there is a requirement for the formation of a stalk. Stalk formation is typically represented by 5 steps and begins with decreasing distance between two membranes. As membrane fusion is highly dependent on membrane fluctuations, it is essential that the membranes are within proximity where such fluctuations are significant (*108*).

Next, local perturbations in the membranes result in the outer leaflets of the two membranes coming into contact with one another. The resulting contact subsequently decreases the number of solvent-exposed non-polar surfaces, causing the two leaflets to fuse. Once this has occurred, the membranes continue to move closer to one another until the inner leaflets have made contact with one another. Following this, the leaflets move in such a way to decrease curvature, moving the interfaces outward and subsequently forming a pore between the previously distinct membranes.

In the case of liposomes, the further propagation of this pore size or the aggregation of multiple pores in close proximity will result in the fusion of the two vesicles into one larger vesicle. However, in the case of liposome interactions with cells, there are additional proteins involved in the membrane fusion and exocytosis of the two dissimilar membranes. This type of membrane fusion is believed to be catalyzed by synaptic SNARE proteins, or soluble NSF attachment protein receptors (*109*). This group of

proteins includes a number of proteins, including the R-SNAREs and Q-SNAREs. R-SNARES contribute arginine residues while Q-SNARES contribute glutamine residues and include proteins such as syntaxin-1 and synaptosmal-assocaited protein-25, or SNAP-25 (*110*). These proteins are typically small and range between 10-35 kDa which possess a strand of 60-70 amino acids known as the SNARE motif (*110, 111*). It has been demonstrated that spontaneous fusion of multiple liposomes occurs when these SNARE proteins are present in the lipid bilayer. Additionally, these SNARE protein complexes which induce membrane fusion were examined using electron microscopy and found to be rod shaped, measuring roughly 13-14nm long and 2 nm wide (*112*).

Methods of anchoring

A popular application of liposomes is within the realm of targeted drug delivery to tumors as part of cancer treatments. To accomplish this, researchers typically incorporate anti-bodies onto drug-carrying liposomes, either directly onto the lipid head (Type I immunoliposome) or by way of a linking molecule (Type II immunoliposome), such as polyethyleneglycol (*113*). In addition to being potentially useful as linking molecules to allow more flexibility for ligand binding, PEG has been shown to be an especially useful tool for increasing the circulation time of liposomes *in vivo* by functioning as a stealthing mechanism. For an unmodified liposome, a diameter of greater than 300nm will typically result in ineffective drug delivery because of detection and degradation by the mononuclear phagocyte system (*114*). This detection is beneficial in the instance where drug delivery to the MPS is desirable, but for all other areas of interest, this is problematic. The root of the problem with regards to detection

stems from the binding of opsonins to the liposome surface. To combat this effect, the use of PEG chains has become commonplace. The large, hydrophilic regions of the PEG chain result in hydration forces which sterically inhibit the opsonins and drastically improve the circulation time of the liposome (*115*).

However, PEGylated liposomes may not provide the necessary stiffness for shearing liposomes via external magnetic force. Limited research has been performed in the realm of utilizing more rigid anchoring mechanisms, such as polysaccharides. As mentioned previously, saccharides are very commonly used for improving long term stability of liposomes as cryopreservants, including chitosan. However, many researchers have begun to look to chitosan-coated liposomes for mucoadhesion (*116, 117*). Others have created a liposome which features deacylatized N-palmitoyl chitosan anchors embedded within the lipid bilayer (*118*).

Alternative methods for binding liposomes to biological materials *in vivo* include tagging polymer chains with arginylglycylaspartic acid (RGD). RGD is a well-studied peptide which plays a vital role focal adhesions and binding cells to ECM via integrins (*119*). Hydrophobes have also been demonstrated as a useful tool for seeding liposomes on treated substrates. In one instance, researchers used liposomes as a surface treatment to enhance lubrication. The liposomes were tethered to a chitosan-based biopolymer film via dodecyl hydrophobes embedded within the lipid bilayer (*120*). The system showed a significant decrease in coefficient of friction compared to standard conditions of sliding plates and also showed little sign of wear on the seeded liposomes over the course of 50 cycles.

Improving long term stability of liposomes

One common method to improve the encapsulation performance of liposomes is to incorporate sugars such as sucrose, trehalose or others into the aqueous media during the dispersion stage. The sugar groups improve the stability by working as a surfactant and preventing liposomes from binding with one another while in storage below the phase transition temperature of the lipid (*120*). Improving stability of liposomes in long-term storage is also of considerable interest to liposome researchers. One common way of achieving this is by freeze-drying, or lyophilizing, the cargo-filled vesicles before rehydrating in aqueous media (*121-123*).

Chapter 5 Gut-on-a-chip

Introduction

Biomimetic microsystems provide stronger test toolsets that reconstitute human organ structures and functions. These biomimetic systems aim to enable accurate, high-throughput characterization of drug candidates in clinical studies and reduce the number of costly and highly variable in vivo animal models which may differ from the human response (124). Advances in in vitro model systems, such as 3D cell culture models with advanced materials (e.g. hydrogel), have contributed to a better understanding of the form and function of human cells and tissues in physiologically relevant environments (125). However, the reproduction of physiologically critical features including dynamically changing mechanical, chemical, and electrical cues to recapitulate fully functional organs is still challenging and poses significant technical challenges in the replication of living systems using microfluidics techniques (126).

Developing more physiologically accurate model systems requires approaches that match the scale and control of the applicable physiological parameters. With this in mind, microsystems are well-suited as potential solutions for these model systems by providing precise control over essential aspects such as fluid flow, mechanical support, chemical factors, and electrical signals in spatiotemporal cellular environments (*127*). Approaches like compartmentalization have been used in a variety of applications in an attempt to reconstitute primary structure and function of human organs (*128*). Recent accomplishments include recapitulating the lung (*129*), the gut (*130-133*), the blood
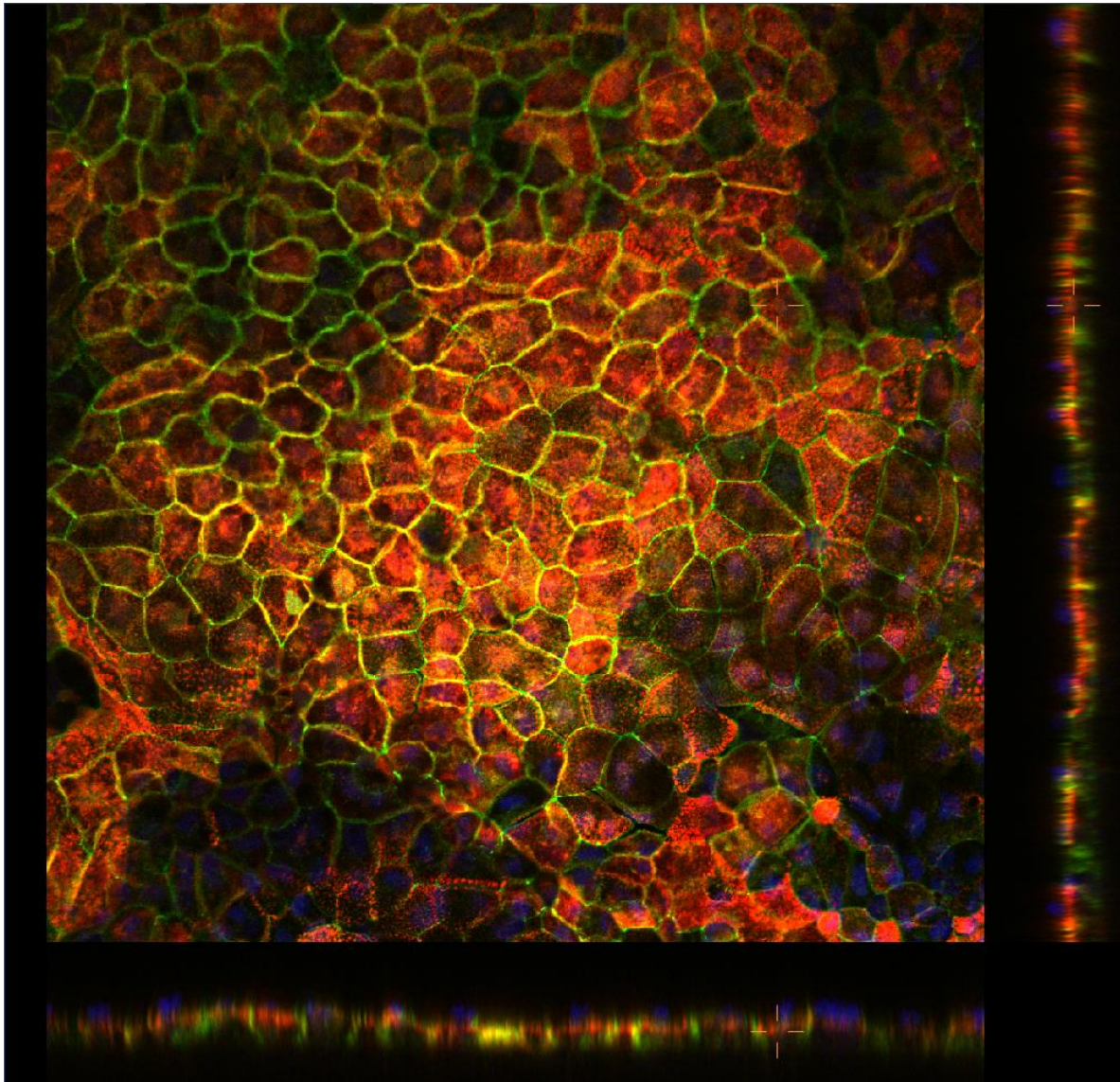
Figure 5.1 Maximum projection of differentiated Caco-2 cell monolayer with three channels stained with immunofluorescence for villin (red) and ZO-1 (green) as well as Hoechst staining for nuclei (1).

vessels (*134*), the liver (*135*), the kidney (*136*), bone (*137*), the brain/CNS (e.g. neurons-on-a-chip) , and muscle (*138*), all of which have shown potential for addressing the challenges in clinical studies. Development of these devices has become a high-impact research area for drug screening in translational medicine and for advanced tissue engineering in regenerative medicine (*17*). Recapitulation of the aforementioned
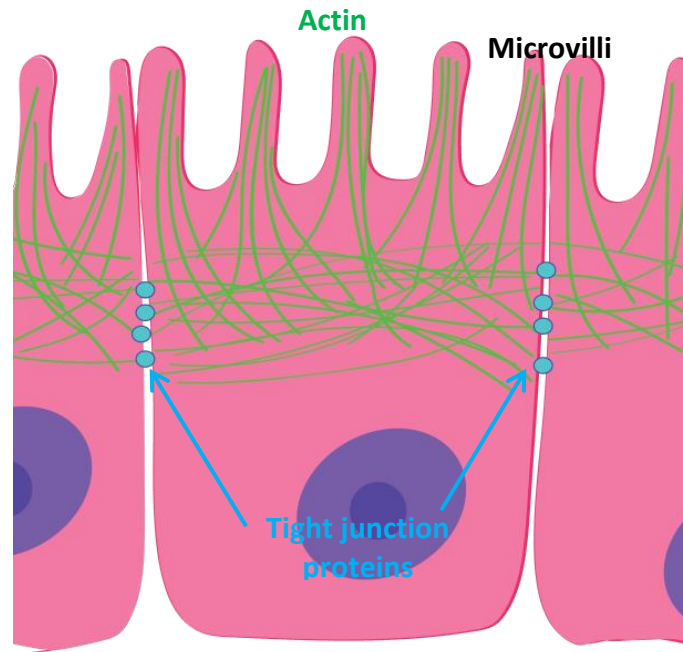
Figure 5.2 Individual differentiated Caco-2 cells produce small finger-like projections along their apical surfaces called microvilli, creating what is known as the brush border. These structures are primarily actin-based. Additionally, neighboring Caco-2 cells produce tight junction proteins such as occludins and cadherins to improve monolayer integrity.

living systems presents a myriad of technical challenges, many of which have been approached with microfluidic techniques.

As part of our role in a grant directed at engineering magnetically activated drug delivery within the human gut, I worked alongside Eric Parigoris to develop a gut-on-a-chip platform which enables us to test our drug delivery capabilities with physiologically relevant human intestinal cells. This work was done in collaboration with Prof. Warren Ruder of the University of Pittsburgh. To do so, we aimed to create a microfluidic system in which to culture Caco-2 cells on a porous PDMS membrane spanning two collinear channels. In this system, it is possible to culture the cells and grow them under low flow rates to stimulate differentiation in a matter of days. This is a stark
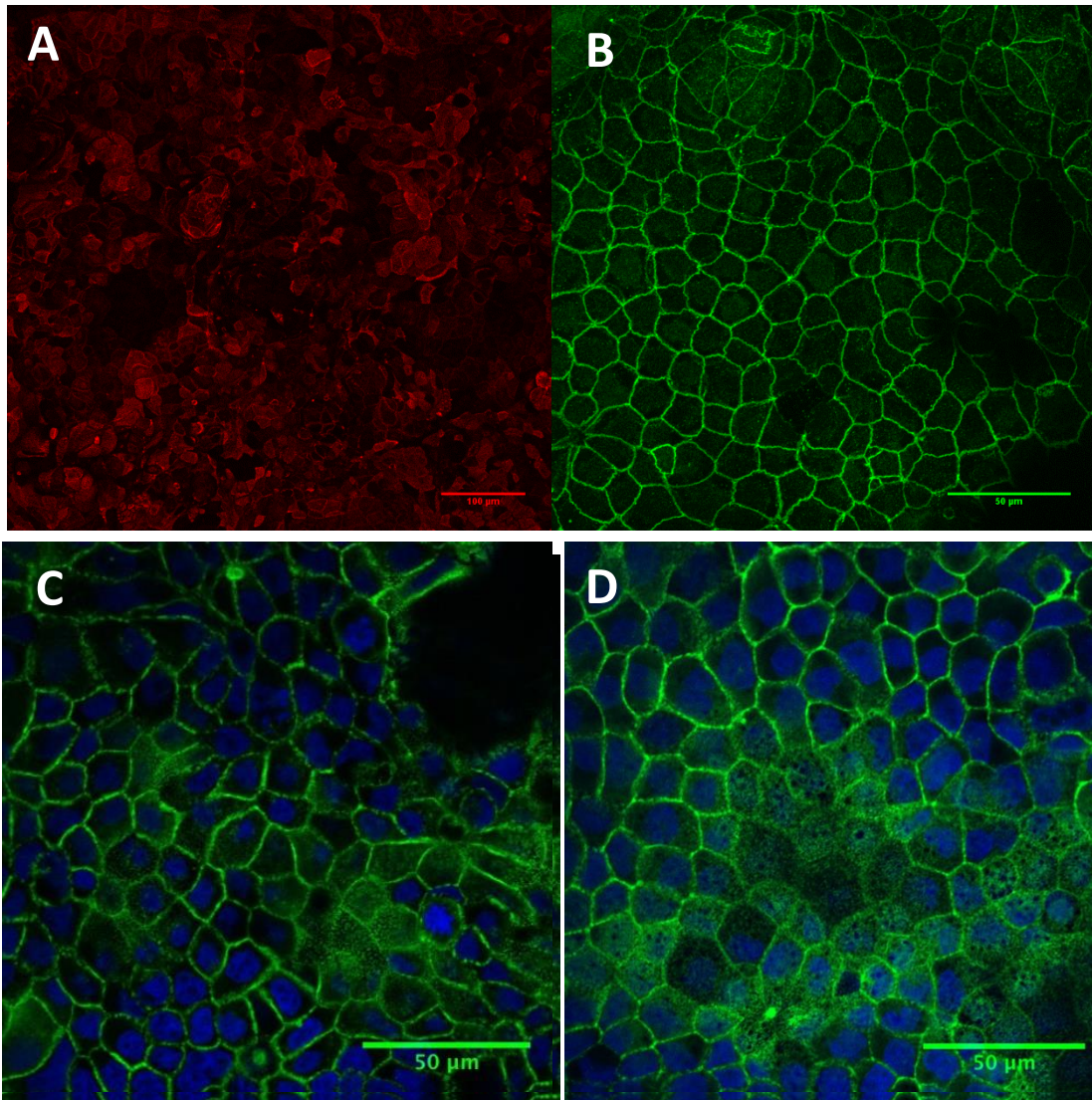
Figure 5.3(A) Microvilli stained using fluorescently tagged villin antibody under healthy conditions. (B) Tight junction protein ZO-1 stained using fluorescently tagged anti-ZO-1 antibody under healthy conditions. (C) Caco-2 stained for actin using fluorescently tagged phalloidin (green channel) and nuclei with DAPI (1) under normal conditions. (D) Caco-2 cells stained for actin and nuclei following 24 hour incubation with LPS. Vacancies in dense actin regions possibly indicate degradation of the microvilli due to the endotoxin.

improvement over the three to four weeks required for differentiation in traditional static Transwell cultures (Figure 5.1). Differentiation for the Caco-2 cell line is extremely important with regards to morphology and cell behavior. *In vivo*, the cells collectively form finger-like protrusions inside the gut called villi in addition to individually producing

actin-based protrusions called microvilli (Figure 5.2), both of which increase surface area and aid in nutrient absorption. Within the microvilli, there is an actin-binding protein named villin which serves as a useful indicator of the formation of the microvilli brush border and thus, differentiation. Equally important to the formation of the brush border is the formation of an integral cell monolayer to serve as an additional barrier beyond the mucosal layer to prevent bacterial infection. Useful indicators of this are tight junction proteins, which include a number of cadherins, occludins and others. For this work, zonal occluding 1 (ZO-1) is targeted using immunostaining to serve as a second indicator of differentiation (Figure 5.2B).

Immunostaining Caco-2 Cells for Differentiation Indicators in Transwell culture

The cells were grown in traditional Transwell inserts for four weeks at 37 °C at 5% CO_2 to ensure differentiation, with liquid growth media changed every two to three days. In order to stain for villin, a primary villin (mouse) antibody (Santa Cruz Biotech) was incubated on the cells for 1 hour followed by 1 hour of incubation with an Alexa Fluor 594 goat anti-mouse antibody. Similarly, to evaluate the presence of tight junction proteins, a rabbit anti-ZO-1 antibody was introduced followed by an Alexa Fluor 488 donkey anti-rabbit antibody. In addition to these fluorophore-tagged anti-bodies, Hoechst staining was performed at a concentration of 0.4 µm/mL for 5 minutes to tag the nucleus as a positional reference for imaging. The cells were imaged using confocal

microscopy to produce a 3 dimensional representation of the structure and further elucidate the presence of the differentiation markers (Figure 5.3A and B).

From this benchmark data, we also looked to evaluate the effects of bacterial infection with regards to mechanical structure of the cells. To do this, we introduced the endotoxin lipopolysaccharide from the bacteria *Escherichia coli* into the Caco-2 Transwell system and incubated for 24 hours before rinsing and staining. Comparing between the control cells, there appeared to be a form of degradation in the microvilli structure in the form on vacancies within the brush border when stained with fluorophore-tagged phalloidin to tag actin structures (Figure 5.3C and D). However, due to the time required to reach differentiation using traditional Transwell culture and the ultimate need for integration with the microfluidic magnetic tensile cytometry system described in the previous chapter, efforts were made to create a microfluidic system in which to grow Caco-2 cells.

Microfluidic gut-on-a-chip design

Drawing much of the inspiration from previous gut-on-a-chip devices, we implemented a set of two channels through which a permeable PDMS membrane is suspended. The two channels feature inlet and outlet channels arranged 20 ° outward from the central axis of the main channel (Figure 5.4A). The same mold is used for both top and bottom channels, forming a symmetric channel geometry when the two channels are bound facing each other to secure the suspended membrane (Figure 5.4C). A channel width of 1000 μm and a height of 150 μm were used to create a relatively large area upon which
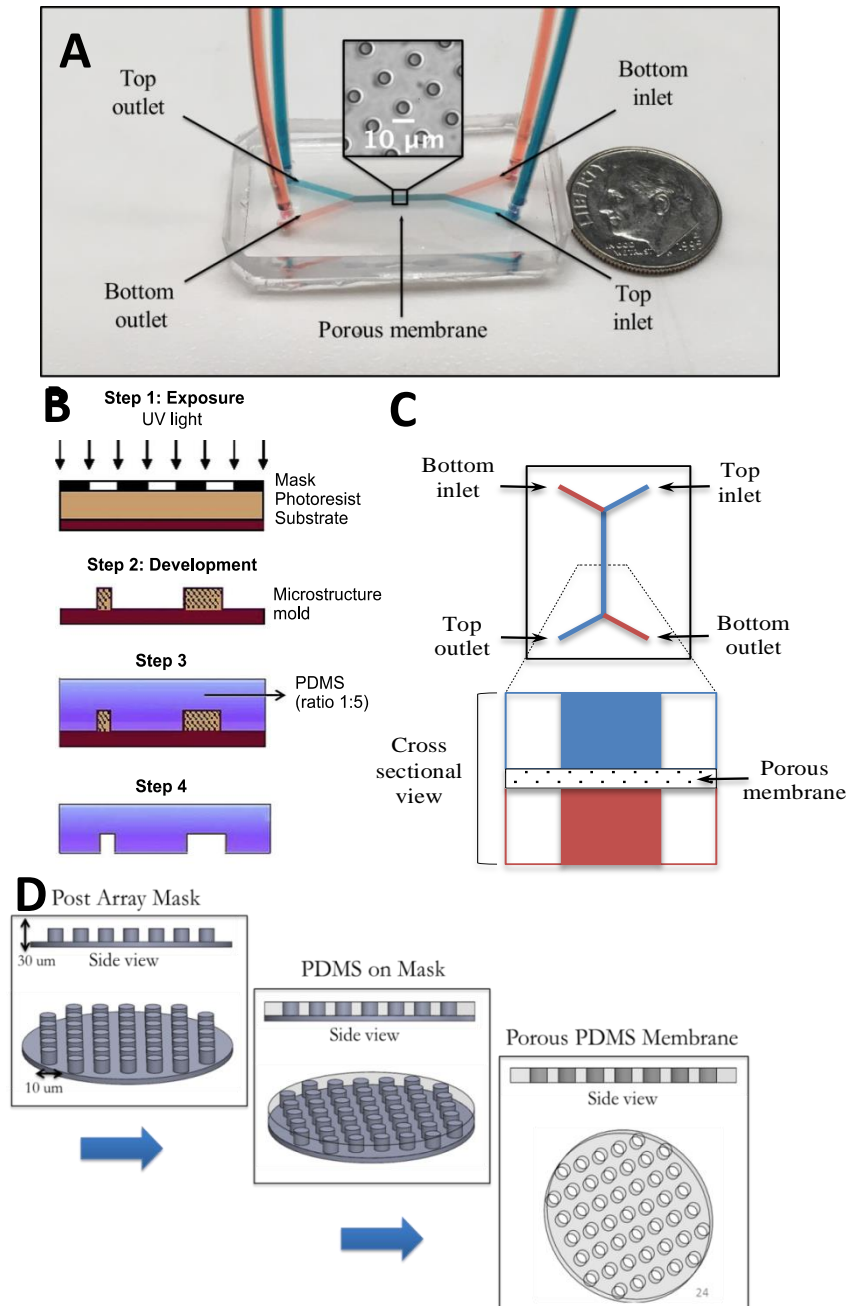
Figure 5.4 (A) Image of the fabricated gut-on-a-chip device with an inset brightfield view of the suspended permeable PDMS membrane. (B) Photolithography procedure used for fabricating channels. (C) Schematic of the gut-on-a-chip device and cross-section view. (D) Outline of process for preparing porous PDMS membrane from a patterned micropost array (courtesy of Eric Parigoris).

to form a cell monolayer in comparison to the size of Caco-2 cells (roughly 30 µm).

While previous gut-on-a-chip designs have featured pneumatic channels flanking the
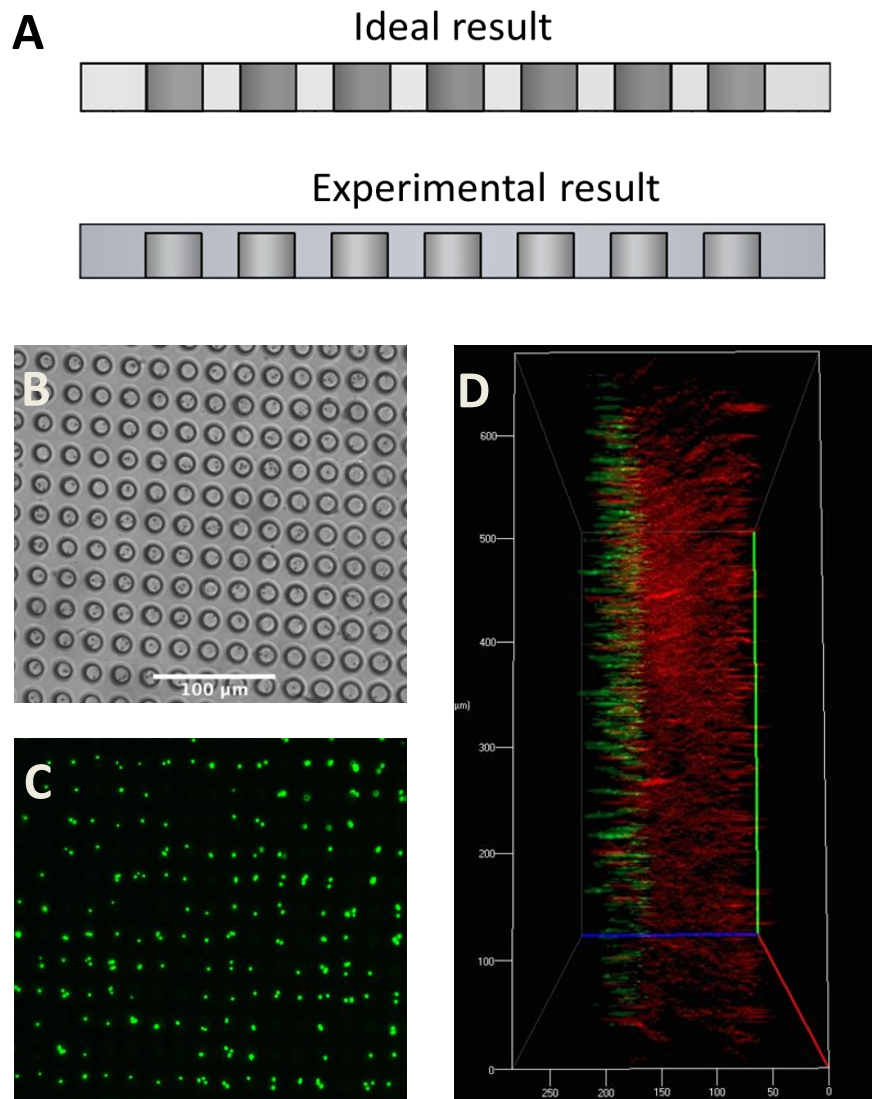
Figure 5.5 (A) Ideal result versus the experimental result featuring a residual layer of PDMS preventing the formation of a permeable structure. (B) Bright field image of beads trapped within the wells form by the microposts and residual PDMS layer. (C) Fluorescence image of beads trapped within the wells formed by the microposts and residual PDMS layer. (D) Confocal image of PDMS doped with Nile Red (red) and green fluorescent beads unable to permeate through the membrane (courtesy of Eric Parigoris).

main channel to mimic peristalsis, it was determined that the pneumatic channels were

not necessary for our implementation due to the negligible advantage presented over

simple fluid flow as well as the possible interference with the components of the magnetic tensile cytometry system in later design iterations.

The channel masks were designed using AutoCAD and printed by a third party (CADArt) to fit on a 4 inch silicon wafer. The channels were then created via traditional photolithography using SU-8 photoresist and developer (Figure 5.4B). Once created, the molds were treated with a silanizing agent to improve workability and prevent cracking of the SU-8 features or wafer. To test the channel design, a store-bough polycarbonate membrane was suspended between two channels and Caco-2 cells were seeded within the channel and allowed to grow 3 days. Due to the small pore sizes and the translucency of the material, the polycarbonate membranes were not ideal for this application, but proved capable of achieving an adherent cell monolayer.

The fabrication of the permeable PDMS membrane on which to seed the cells was the most challenging aspect of the gut-on-a-chip design. As seen in Figure 5.4A, the pores were designed to be 10 µm in diameter with a center to center distance of 30 µm. To create this porous PDMS membrane, an array of posts was microfabricated on a silicon wafer using a series of etching steps. Once the posts were fabricated and silanized, PDMS was spin coated in a thin layer over the posts and allowed to cure (Figure 5.4D). The membrane was then peeled off and tested for permeability within the channel. The primary deficiency with this approach is the need for etching of PDMS to produce pores which span the entire thickness of the membrane. Due to the design of the mold and the nature of spin coating, it is extremely difficult to avoid the formation of a residual thickness of PDMS above the posts (Figure 5.5A). This difficulty is compounded by the fragility of the thin membrane as well as the challenge of transferring a thin PDMS

A

PDMS Membrane

Top Channel

Bottom Channel

Plasma Etching

PDMS Stamping

Uncured PDMS

Device Assembly

Heat

B

Static wet etching

Dynamic wet etching
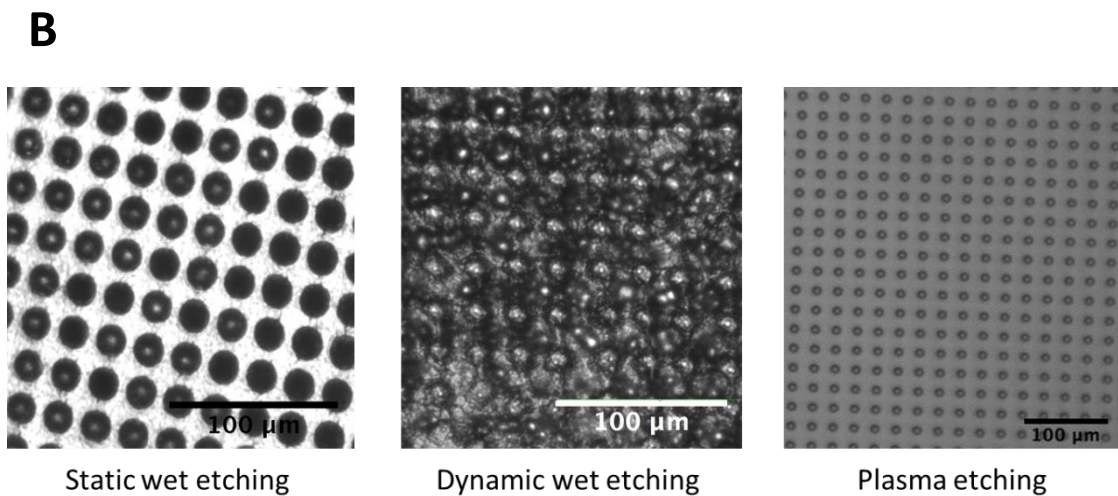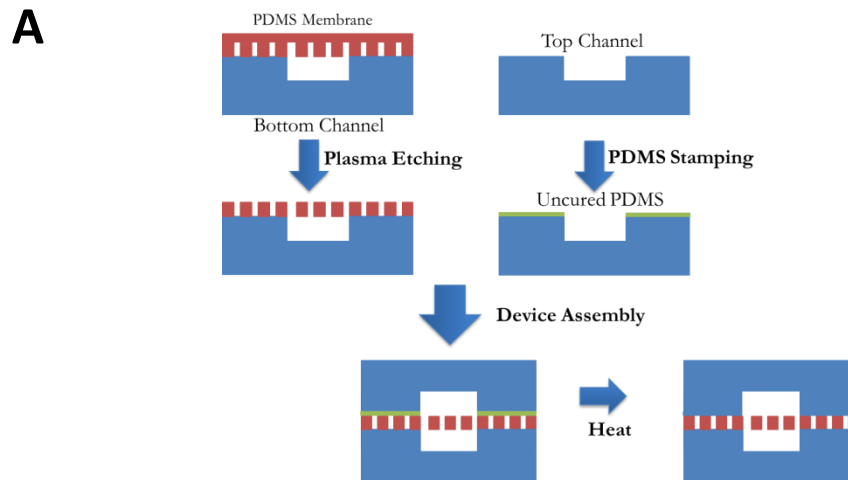
Plasma etching

Figure 5.6 (A) Process for plasma etching PDMS membranes and channel fabrication. (B) Bright field images comparing the three main etching techniques attempted to achieve permeability in the PDMS membrane: static wet etching, dynamic wet etching and plasma etching (courtesy of Eric Parigoris).

membrane which has the tendency to wrinkle or stick to itself. A number of different tests were performed to determine whether or not pore formation was successful in this approach, including permeability assays with Lucifer Yellow dye, fluorescent beads and combining beads with fluorescently doped PDMS membranes before using confocal microscopy to create a 3-D view (Figure 5.5B, C and D). From these metrics, it was determined that the membrane did not have permeable pores owing to the residual
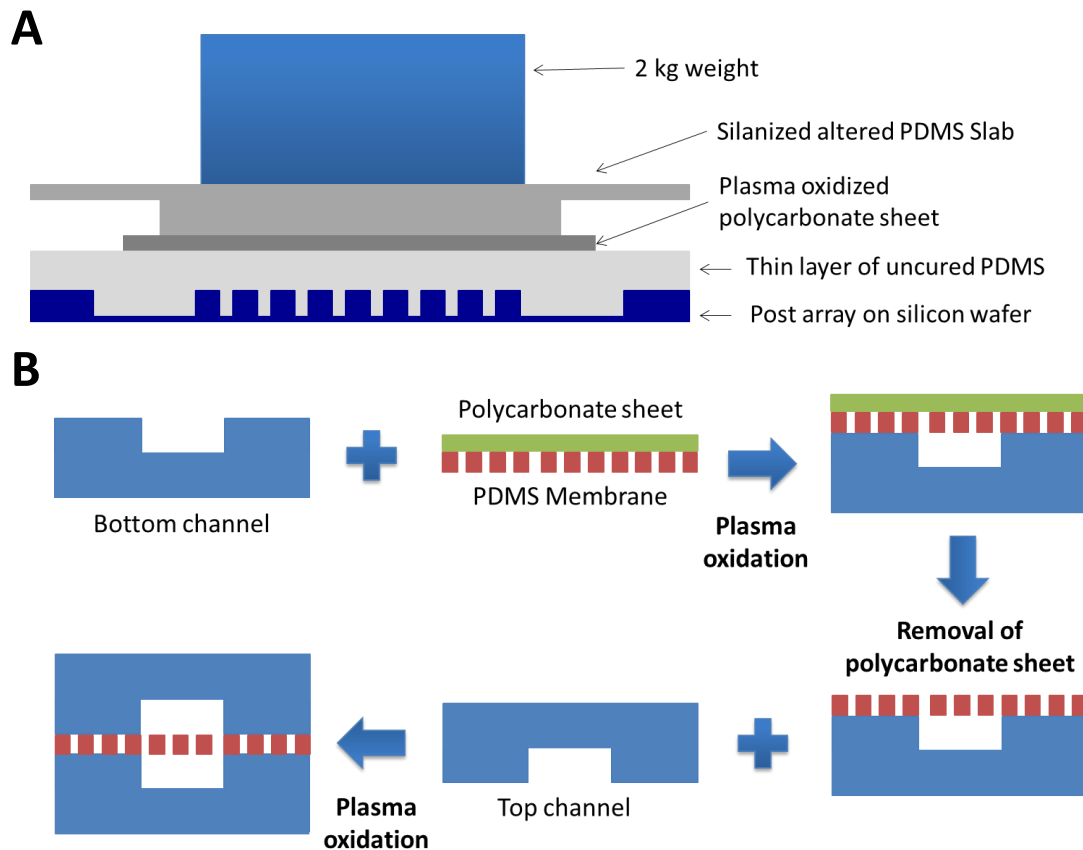
Figure 5.7 (A) Process for fabricating permeable PDMS membranes using the loaded curing apparatus. (B) Fabrication of the gut-on-a-chip device with the sacrificial polycarbonate layer for transferring the permeable membrane.

layer. As a result of this fabrication difficulty, we looked to chemical with a mixture of 1-methyl-2-pyrrolidinone and tetrabutyl-ammonium-fluoride as well as plasma etching of the residual PDMS. However, there were a number of drawbacks to these approaches, including the time required for processing, the cost for equipment time and potential damage to the membrane itself during the procedure leading to rupture (Figure 5.6).

Instead of relying on etching to complete the pores, interactions with other groups who have created similar structures led us to fabricate an apparatus with which to apply even downward pressure during PDMS curing to eliminate the residual layer. To do this,

we created a system of laser cut acrylic discs, one functioning as a base and the other functioning as a load platform. Upwards from the base extends three guide posts which serve to align the load platform to ensure the platform remains horizontal and to prevent any slipping as the PDMS is forced out from the mold. Below the load platform is a silanized PDMS slab to serve as a compliant intermediary material to improve force distribution. The uncured spin-coated PDMS mold is placed on top of the base under the loading platform and polycarbonate sheets are placed over the patterned areas of the mold. The polycarbonate sheets are used as a sacrificial layer to allow easy transfer from the mold to microfluidic channels without concerns of wrinkling or tearing. Additionally, the PDMS to be spin-coated onto the mold is diluted with cyclohexane to reduce viscosity, which thereby improves the wetting when poured over the micro-posts as well as the ease with which the residual PDMS can be forced out using the loaded curing apparatus.When the mold is placed securely in the center of the platform with the polycarbonate sheets appropriately positioned, the load platform and silanized PDMS slab are brought down slowly into contact. Once contact is initiated, a 3 kg weight is carefully placed on the loading platform and the membrane is allowed to cure overnight at room temperature (Figure 5.8A).
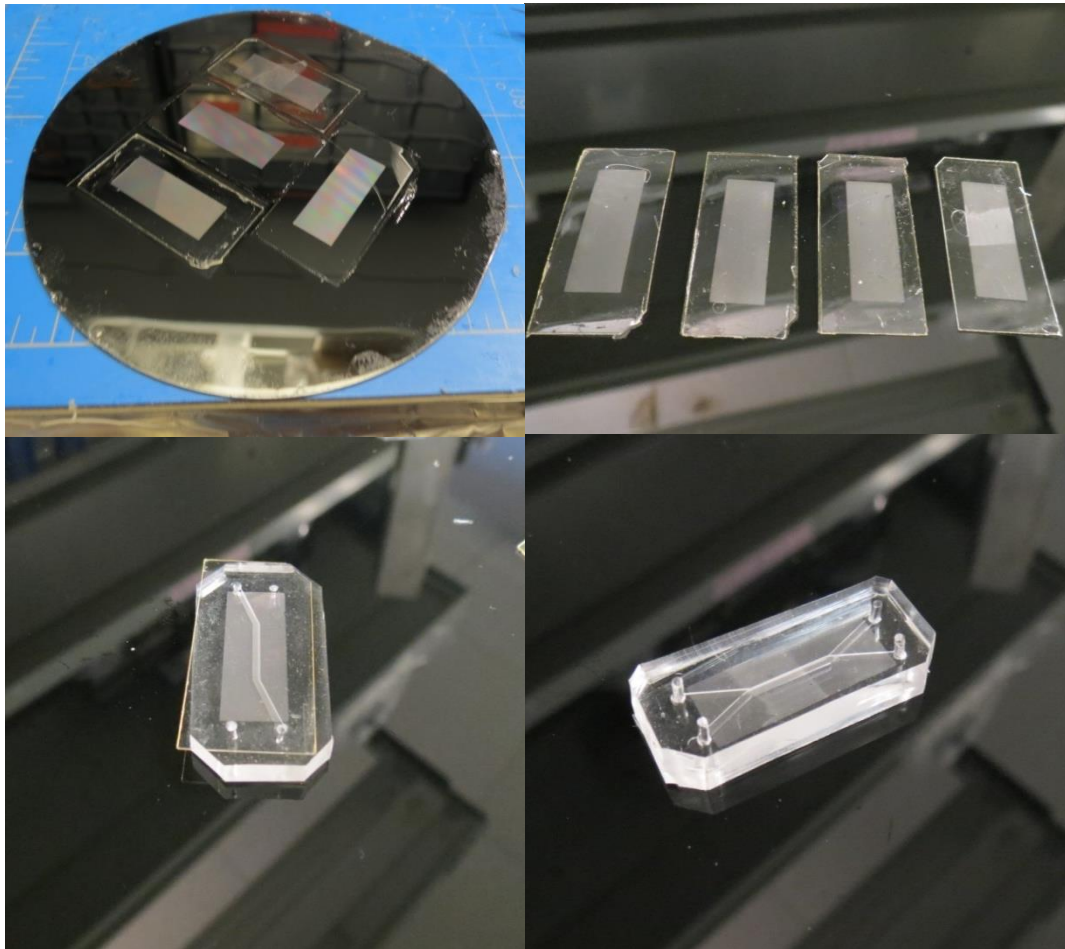
Figure 5.8 (A) Silicon wafer patterned with microposts for permeable PDMS membrane fabrication (B) permeable PDMS membranes on sacrificial polycarbonate sheets for application (C) upper PDMS microfluidic channel with pre-punched holes bound to permeable membrane via plasma oxidation. (D) Completed gut-on-a-chip device featuring top and bottom microfluidic channels separated by permeable membrane with punched inlet and outlet holes for both channels.

Following the overnight curing, the polycarbonate-PDMS membrane composites were carefully peeled from the mold and plasma oxidized before being bound to the lower microfluidic channel of the gut on a chip system (Figure 5.8). In this case, the polycarbonate sheet also functions as a protective coating to ensure that the opposing side of the PDMS membrane is not oxidized prematurely during plasma treatment.

Once the two components were pressed together, they were allowed to bake for 2 hours in an oven at 60 °C to improve the seal. The structures were then removed from the oven and the polycarbonate sheets were carefully peeled off before another plasma oxidation cycle, this time leading to the bonding with the second channel (Figure 5.8). The channels were then placed in the oven once again and were plasma oxidized prior to fluid introduction to render the PDMS surfaces hydrophilic (Figure 5.8B). To test the permeability of the device, food coloring was introduced in the top channel and was able to diffuse through into dH_2O flowing through the bottom channel, indicating the presence of a permeable pore system. This result was further validated with fluorescent showing similar phenomenon under the microscope.

Lastly, the Caco-2 cells were seeded on the suspended permeable membrane to establish the viability of the cells in the environment under constant incubated media flow. After a few days of culture and treatment of the PDMS with collagen to provide an ECM, the Caco-2 cells were able to form a monolayer across the channel width (Figure 5.8C and D). In some locations of the channel, delamination appeared to occur after handling for microscopy. To remedy this, further refinement of the ECM coating step is needed as well as optimization of the flow conditions.
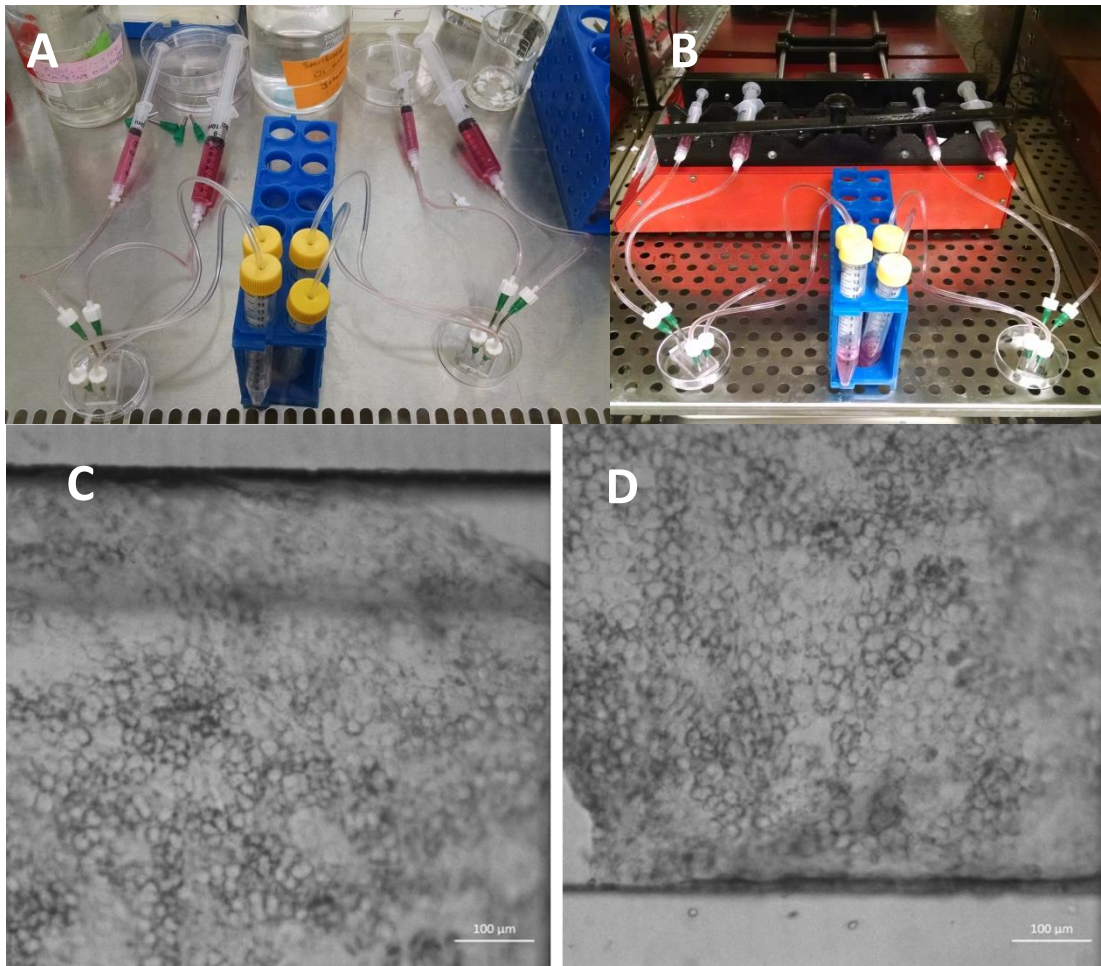
Figure 5.9 (A) Photograph of gut-on-a-chip arrangement within mammalian culture hood following seeding of Caco-2 cells. (B) Photograph of gut-on-a-chip system positioned in the syringe pump within a CO2 incubator. (C and D) Bright-field views of Caco-2 cells seeded within the gut-on-a-chip system (courtesy of Eric Parigoris)

Chapter 6 Summary and future work

Integrating synthetic cells and soft robotics

The next phase of the project will focus on utilizing the signal produced by the sensory bacteria to direct a behavioral response from the soft robot. To accomplish this, we aim to use chemo-sensing bacteria which output luminescence rather than chemo-sensing bacteria which produce GFP. The resulting luminescent is then to be sensed by embedded photodiodes, which can then be translated into action through a CPU. We aim to accomplish by treating each appendage of the robotic gripper as a directional sensor. In the case that the bacteria within one or two appendages detect the chemical IPTG from the outside environment, this initiates luminescence in those cells. The embedded photodiodes win the central region of the device will then detect that signal and relay it to an off-board CPU. The CPU will then act upon this information by initiating motion by activating SMAs on the device to produce a swimming motion in the sensed direction (Figure 6.1A).

Characterization of the luminescent bacteria has been performed to determine the optimal growth conditions within the device. Unlike the fluorescence module utilized in the previous work, the reaction to produce luminescence within the cells is ATP-intensive and the luminescence output will degrade much more rapidly than the fluorescence signal. Measuring the luminescence output of these cells in a plate reader with both M9 and LB media for 5 hours after dilution in fresh media shows the nutrient
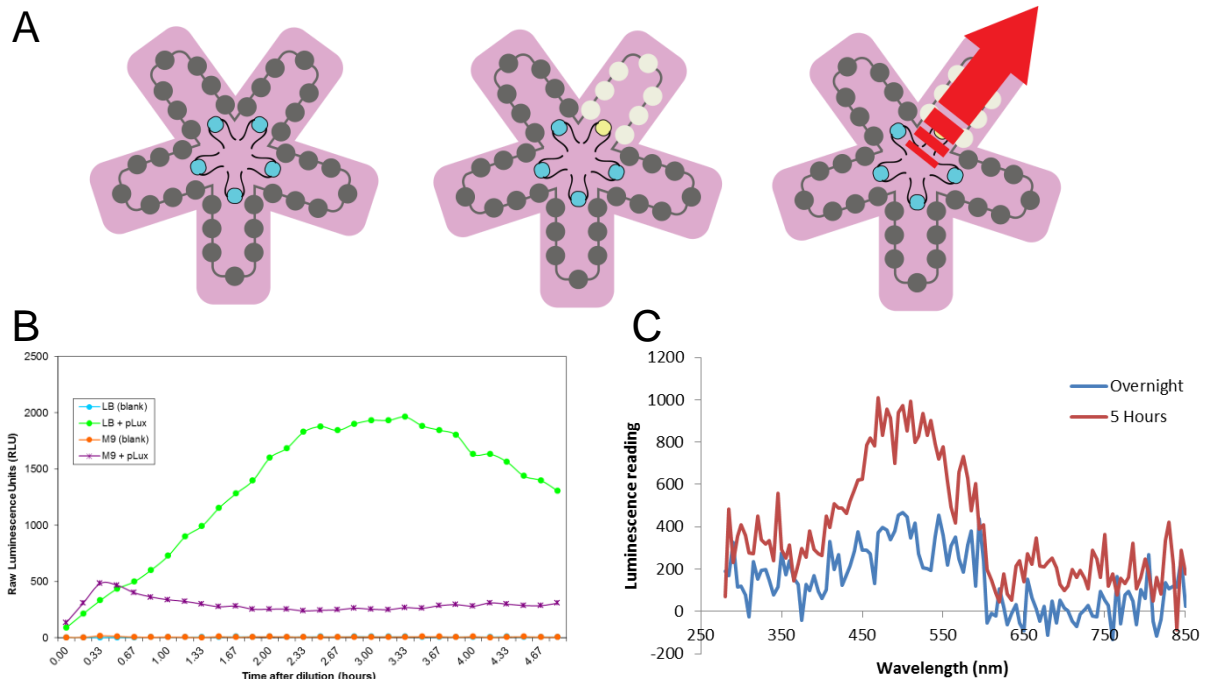
Figure 6.1 (A) Schematic of biosensing robotic motion. Luminescent bacteria is introduced in the patterned wells with embedded photodiodes to observe light levels in each member. In the case of a member detecting IPTG, the bacteria begin to luminescence and the signal is detected by the corresponding photodiode. This information is then translated by an off-board CPU into SMA actuation for motion. (B) Characterization of luminescent bacteria in M9 and LB growth media. (C) Luminescence wavelength scan for bacteria to determine optimal photodiodes. Because the luminescence reaction is heavily dependent on ATP, there is a significant reduction in the signal in cultures grown overnight.

dependency of the reaction, both in regards to the chemical composition of the media as well as the time scale (Figure 6.1B). Furthermore, the light produced is not uniform across wavelengths. To better determine the ideal photodiode to be embedded within the system, a luminescence wavelength scan was performed with a plate reader which showed peak fluorescence in the region of 450-550nm (Figure 6.1C). Tests with photodiodes to detect the luminescence of the cells are on-going but have proven difficult due to the signal strength in combination with the photodiode sensitivities.

Magnetoliposomes and Magnetic Tensile Cytometry Channel

The immediate challenge for the magnetoliposomes project is reliably rupturing the vesicles when anchored within the microfluidic channel. MATLAB will be employed to determine the most effective mu-metal pattern computationally and then implemented into the MTC chip. Once this is determined, the next phase is to optimize the protocol for binding streptavidin coated beads to the liposomes in a way that consistently produces at least one bead bound to each liposome. This might be a factor of flow properties within the channel, a matter of concentration or it might be predominantly influenced by steric inhibition. In the case of the latter, functionalizing the beads with polymer chains to aid in the binding may prove the optimal solution. Once the beads can be consistently and reliably bound to the liposomes and facilitate rupture within the MTC channel, the next step would be to integrate the system with the gut on a chip system and perform the rupture by anchoring the liposomes to cells rather than an avidin coated substrate.

Gut-on-a-chip system

The next step for the gut-on-a-chip development is to improve the adhesion of the cells upon the permeable membrane and verify that the Caco-2 cells reach differentiation within the channel under low fluid flow. To do this, the cells must be immunostained for villin and ZO-1 as done previously using Transwell culture procedures. Following this verification, the gut-on-a-chip will be modified to accommodate the MTC system

designed to work with the liposomes to create a targeted drug delivery assay for magnetically triggered vesicles.

References

1.   C. L. Wanamaker *et al.*, Consequences of polylactide stereochemistry on the properties of polylactide-polymenthide-polylactide thermoplastic elastomers. *Biomacromolecules* **10**, 2904-2911 (2009).

2.   K. Kijsirichareanchai *et al.*, Hands-On Spiral Enteroscopy Training in Soft Cadaver Model: A Multi-National Experience. *Am J Gastroenterol* **105**, S513-S513 (2010).

3.   D. E. Ingber, Integrins, tensegrity, and mechanotransduction. *Gravit Space Biol Bull* **10**, 49-55 (1997).

4.   P. G. Gillespie, U. Muller, Mechanotransduction by hair cells: models, molecules, and mechanisms. *Cell* **139**, 33-44 (2009).

5.   B. Geiger, J. P. Spatz, A. D. Bershadsky, Environmental sensing through focal adhesions. *Nat Rev Mol Cell Biol* **10**, 21-33 (2009).

6.   D. E. Discher, P. Janmey, Y. L. Wang, Tissue cells feel and respond to the stiffness of their substrate. *Science* **310**, 1139-1143 (2005).

7.   T. H. Barker *et al.*, Synergistic effects of particulate matter and substrate stiffness on epithelial-to-mesenchymal transition. *Res Rep Health Eff Inst*, 3-41 (2014).

8.   S. I. Simon, H. L. Goldsmith, Leukocyte adhesion dynamics in shear flow. *Ann Biomed Eng* **30**, 315-332 (2002).

9.   D. A. Hammer, Simulation of cell rolling and adhesion on surfaces in shear flow. Microvilli-coated hard spheres with adhesive springs. *Cell Biophys* **18**, 145-182 (1991).

10.   M. Kim, Phototaxis of Cyanobacteria under Complex Light Environments. *MBio* **8**, (2017).

11.   A. Wilde, B. Fiedler, T. Borner, The cyanobacterial phytochrome Cph2 inhibits phototaxis towards blue light. *Mol Microbiol* **44**, 981-988 (2002).

12.   H. Yang, H. Inokuchi, J. Adler, Phototaxis away from blue light by an Escherichia coli mutant accumulating protoporphyrin IX. *Proc Natl Acad Sci U S A* **92**, 7332-7336 (1995).

13.   A. W. Rutherford, T. A. Moore, Mimicking photosynthesis, but just the best bits. *Nature* **453**, 449 (2008).

14.   R. M. Macnab, D. E. Koshland, Jr., The gradient-sensing mechanism in bacterial chemotaxis. *Proc Natl Acad Sci U S A* **69**, 2509-2512 (1972).

15.   A. W. Feinberg *et al.*, Controlling the contractile strength of engineered cardiac muscle by hierarchal tissue architecture. *Biomaterials* **33**, 5732-5741 (2012).

16.   A. W. Feinberg *et al.*, Muscular thin films for building actuators and powering devices. *Science* **317**, 1366-1370 (2007).

17.   A. Grosberg *et al.*, Muscle on a chip: in vitro contractility assays for smooth and striated muscle. *J Pharmacol Toxicol Methods* **65**, 126-135 (2012).

18.   R. Daniels, J. Vanderleyden, J. Michiels, Quorum sensing and swarming migration in bacteria. *FEMS Microbiol Rev* **28**, 261-289 (2004).

19.   S. P. Diggle, A. S. Griffin, G. S. Campbell, S. A. West, Cooperation and conflict in quorum-sensing bacterial populations. *Nature* **450**, 411-414 (2007).

20. A. A. Dandekar, S. Chugani, E. P. Greenberg, Bacterial quorum sensing and metabolic incentives to cooperate. *Science* **338**, 264-266 (2012).

21. A. F. Taylor, M. R. Tinsley, F. Wang, Z. Huang, K. Showalter, Dynamical quorum sensing and synchronization in large populations of chemical oscillators. *Science* **323**, 614-617 (2009).

22. D. E. Discher, D. J. Mooney, P. W. Zandstra, Growth factors, matrices, and forces combine and control stem cells. *Science* **324**, 1673-1677 (2009).

23. N. Ogihara, N. Yamazaki, Generation of human bipedal locomotion by a bio-mimetic neuro-musculo-skeletal model. *Biol Cybern* **84**, 1-11 (2001).

24. M. Haberland, S. Kim, On extracting design principles from biology: II. Case study-the effect of knee direction on bipedal robot running efficiency. *Bioinspir Biomim* **10**, 016011 (2015).

25. C. P. Chen, J. Y. Chen, C. K. Huang, J. C. Lu, P. C. Lin, Sensor data fusion for body state estimation in a bipedal robot and its feedback control application for stable walking. *Sensors (Basel)* **15**, 4925-4946 (2015).

26. M. D. Bartlett *et al.*, High thermal conductivity in soft elastomers with elongated liquid metal inclusions. *Proc Natl Acad Sci U S A* **114**, 2143-2148 (2017).

27. S. H. Song *et al.*, Turtle mimetic soft robot with two swimming gaits. *Bioinspir Biomim* **11**, 036010 (2016).

28. L. Manfredi *et al.*, A bioinspired autonomous swimming robot as a tool for studying goal-directed locomotion. *Biol Cybern* **107**, 513-527 (2013).

29. S. Marras, M. Porfiri, Fish and robots swimming together: attraction towards the robot demands biomimetic locomotion. *J R Soc Interface* **9**, 1856-1868 (2012).

30. H. Herr, R. G. Dennis, A swimming robot actuated by living muscle tissue. *J Neuroeng Rehabil* **1**, 6 (2004).

31. J. H. Low, C. H. Yeow, Rod-based Fabrication of Customizable Soft Robotic Pneumatic Gripper Devices for Delicate Tissue Manipulation. *J Vis Exp*, (2016).

32. S. Biggar, W. Yao, Design and Evaluation of a Soft and Wearable Robotic Glove for Hand Rehabilitation. *IEEE Trans Neural Syst Rehabil Eng* **24**, 1071-1080 (2016).

33. M. A. Delph, 2nd *et al.*, A soft robotic exomusculature glove with integrated sEMG sensing for hand rehabilitation. *IEEE Int Conf Rehabil Robot* **2013**, 6650426 (2013).

34. H. Tsutsui, Y. Murashima, N. Honma, K. Akazawa, Robot hand with soft tactile sensors and underactuated control. *Conf Proc IEEE Eng Med Biol Soc* **2013**, 4148-4151 (2013).

35. N. Kazem, T. Hellebrekers, C. Majidi, Soft Multifunctional Composites and Emulsions with Liquid Metals. *Adv Mater*, (2017).

36. B. A. Gozen, A. Tabatabai, O. B. Ozdoganlar, C. Majidi, High-density soft-matter electronics with micron-scale line width. *Adv Mater* **26**, 5211-5216 (2014).

37. T. Lu, J. Wissman, Ruthika, C. Majidi, Soft Anisotropic Conductors as Electric Vias for Ga-Based Liquid Metal Circuits. *ACS Appl Mater Interfaces* **7**, 26923-26929 (2015).

38. A. Fassler, C. Majidi, Liquid-phase metal inclusions for a conductive polymer composite. *Adv Mater* **27**, 1928-1932 (2015).

39. D. Rus, M. T. Tolley, Design, fabrication and control of soft robots. *Nature* **521**, 467-475 (2015).

40.   L. Xu *et al.*, Bio-inspired annelid robot: a dielectric elastomer actuated soft robot. *Bioinspir Biomim* **12**, 025003 (2017).

41.   K. W. Jun, J. M. Lee, J. Y. Lee, I. K. Ohl, Bio-lnspired dielectric elastomer actuator with AgNWs coated on carbon black electrode. *J Nanosci Nanotechnol* **14**, 7483-7487 (2014).

42.   M. Follador, F. Tramacere, B. Mazzolai, Dielectric elastomer actuators for octopus inspired suction cups. *Bioinspir Biomim* **9**, 046002 (2014).

43.   C. Jordi, S. Michel, E. Fink, Fish-like propulsion of an airship with planar membrane dielectric elastomer actuators. *Bioinspir Biomim* **5**, 026007 (2010).

44.   F. O. Joseph *et al.*, Development of a coordinated controller for robot-assisted shape memory alloy actuated needle for prostate brachytherapy. *Conf Proc IEEE Eng Med Biol Soc* **2014**, 357-360 (2014).

45.   H. Jin *et al.*, A starfish robot based on soft and smart modular structure (SMS) actuated by SMA wires. *Bioinspir Biomim* **11**, 056012 (2016).

46.   J. Colorado, A. Barrientos, C. Rossi, J. W. Bahlman, K. S. Breuer, Biomechanics of smart wings in a bat robot: morphing wings using SMA actuators. *Bioinspir Biomim* **7**, 036006 (2012).

47.   H. Li *et al.*, An All-Stretchable-Component Sodium-Ion Full Battery. *Adv Mater*, (2017).

48.   Y. Xu *et al.*, Flexible, Stretchable, and Rechargeable Fiber-Shaped Zinc-Air Battery Based on Cross-Stacked Carbon Nanotube Sheets. *Angew Chem Int Ed Engl* **54**, 15390-15394 (2015).

49.   S. Xu *et al.*, Stretchable batteries with self-similar serpentine interconnects and integrated wireless recharging systems. *Nat Commun* **4**, 1543 (2013).

50.   M. Mori, K. Suzumori, M. Takahashi, T. Hosoya, Very High Force Hydraulic McKibben Artificial Muscle with a p-Phenylene-2,6-benzobisoxazole Cord Sleeve. *Adv Robotics* **24**, 233-254 (2010).

51.   M. Meller, J. Chipka, A. Volkov, M. Bryant, E. Garcia, Improving actuation efficiency through variable recruitment hydraulic McKibben muscles: modeling, orderly recruitment control, and experiments. *Bioinspir Biomim* **11**, 065004 (2016).

52.   M. A. Mat Dzahir, T. Nobutomo, S. I. Yamamoto, Development of body weight support gait training system using pneumatic Mckibben actuators -control of lower extremity orthosis. *Conf Proc IEEE Eng Med Biol Soc* **2013**, 6417-6420 (2013).

53.   C. Plesse, F. Vidal, D. Teyssie, C. Chevrot, Conducting polymer artificial muscle fibres: toward an open air linear actuation. *Chem Commun (Camb)* **46**, 2910-2912 (2010).

54.   J. C. Nawroth *et al.*, A tissue-engineered jellyfish with biomimetic propulsion. *Nat Biotechnol* **30**, 792-797 (2012).

55.   E. Andrianantoandro, S. Basu, D. K. Karig, R. Weiss, Synthetic biology: new engineering rules for an emerging discipline. *Mol Syst Biol* **2**, 2006 0028 (2006).

56.   A. S. Khalil, J. J. Collins, Synthetic biology: applications come of age. *Nat Rev Genet* **11**, 367-379 (2010).

57.   D. D. Lewis, F. D. Villarreal, F. Wu, C. Tan, Synthetic biology outside the cell: linking computational tools to cell-free systems. *Front Bioeng Biotechnol* **2**, 66 (2014).

58.   J. Macia, F. Posas, R. V. Sole, Distributed computation: the new wave of synthetic biology devices. *Trends in Biotechnology* **30**, 342-349 (2012).

59. K. Wu, C. V. Rao, Computational methods in synthetic biology: towards computer-aided part design. *Curr Opin Chem Biol* **16**, 318-322 (2012).

60. R. Ohlendorf, R. R. Vidavski, A. Eldar, K. Moffat, A. Moglich, From Dusk till Dawn: One-Plasmid Systems for Light-Regulated Gene Expression. *J Mol Biol* **416**, 534-542 (2012).

61. C. M. Tan, S. J. Lo, P. R. LeDuc, C. M. Cheng, Frontiers of optofluidics in synthetic biology. *Lab Chip* **12**, 3654-3665 (2012).

62. S. Bauer *et al.*, 25th anniversary article: A soft future: from robots and sensor skin to energy harvesters. *Adv Mater* **26**, 149-161 (2014).

63. F. Ilievski, A. D. Mazzeo, R. F. Shepherd, X. Chen, G. M. Whitesides, Soft robotics for chemists. *Angew Chem Int Ed Engl* **50**, 1890-1895 (2011).

64. S. Kim, C. Laschi, B. Trimmer, Soft robotics: a bioinspired evolution in robotics. *Trends Biotechnol* **31**, 287-294 (2013).

65. M. Wehner *et al.*, An integrated design and fabrication strategy for entirely soft, autonomous robots. *Nature* **536**, 451-455 (2016).

66. M. L. Hammock, A. Chortos, B. C. K. Tee, J. B. H. Tok, Z. A. Bao, 25th Anniversary Article: The Evolution of Electronic Skin (E-Skin): A Brief History, Design Considerations, and Recent Progress. *Adv Mater* **25**, 5997-6037 (2013).

67. T. Lu, L. Finkenauer, J. Wissman, C. Majidi, Rapid Prototyping for Soft-Matter Electronics. *Adv Funct Mater* **24**, 3351-3356 (2014).

68. R. F. Shepherd *et al.*, Multigait soft robot. *P Natl Acad Sci USA* **108**, 20400-20403 (2011).

69. S. A. Morin *et al.*, Camouflage and Display for Soft Machines. *Science* **337**, 828-832 (2012).

70. G. R. Gossweiler *et al.*, Mechanochemically Active Soft Robots. *ACS Appl Mater Interfaces* **7**, 22431-22435 (2015).

71. C. Larson *et al.*, Highly stretchable electroluminescent skin for optical signaling and tactile sensing. *Science* **351**, 1071-1074 (2016).

72. M. Calisti *et al.*, An octopus-bioinspired solution to movement and manipulation for soft robots. *Bioinspir Biomim* **6**, 036002 (2011).

73. M. Cianchetti, M. Calisti, L. Margheri, M. Kuba, C. Laschi, Bioinspired locomotion and grasping in water: the soft eight-arm OCTOPUS robot. *Bioinspir Biomim* **10**, 035003 (2015).

74. H. T. Lin, G. G. Leisk, B. Trimmer, GoQBot: a caterpillar-inspired soft-bodied rolling robot. *Bioinspir Biomim* **6**, (2011).

75. R. V. Martinez *et al.*, Robotic tentacles with three-dimensional mobility based on flexible elastomers. *Adv Mater* **25**, 205-212 (2013).

76. K. Suzumori, S. Endo, T. Kanda, N. Kato, H. Suzuki, A Bending Pneumatic Rubber Actuator Realizing Soft-bodied Manta Swimming Robot. *Proceedings of the IEEE International Conference of Robotics and Automation (ICRA)*, (2007).

77. C. L. Zhou, K. H. Low, Design and Locomotion Control of a Biomimetic Underwater Vehicle With Fin Propulsion. *Ieee-Asme T Mech* **17**, 25-35 (2012).

78. R. Deimel, O. Brock, A novel type of compliant and underactuated robotic hand for dexterous grasping. *Int J Robot Res* **35**, 161-185 (2016).

79. X. C. Zhou, C. Majidi, O. M. O'Reilly, Soft hands: An analysis of some gripping mechanisms in soft robot design. *Int J Solids Struct* **64-65**, 155-165 (2015).

80.   A. W. Feinberg, Biological Soft Robotics. *Annu Rev Biomed Eng* **17**, 243-265 (2015).

81.   C. Cvetkovic *et al.*, Three-dimensionally printed biological machines powered by skeletal muscle. *P Natl Acad Sci USA* **111**, 10125-10130 (2014).

82.   T. L. Deans, A. Singh, M. Gibson, J. H. Elisseeff, Regulating synthetic gene networks in 3D materials. *P Natl Acad Sci USA* **109**, 15217-15222 (2012).

83.   Y. Ding, F. Wu, C. Tan, Synthetic Biology: A Bridge between Artificial and Natural Cells. *Life (Basel)* **4**, 1092-1116 (2014).

84.   M. B. Elowitz, S. Leibler, A synthetic oscillatory network of transcriptional regulators. *Nature* **403**, 335-338 (2000).

85.   C. M. Tan, S. Saurabh, M. P. Bruchez, R. Schwartz, P. LeDuc, Molecular crowding shapes gene expression in synthetic cellular nanosystems. *Nat Nanotechnol* **8**, 602-608 (2013).

86.   D. D. Mehta, H. A. Cheyne, 2nd, A. Wehner, J. T. Heaton, R. E. Hillman, Accuracy of Self-Reported Estimates of Daily Voice Use in Adults With Normal and Disordered Voices. *Am J Speech Lang Pathol* **25**, 634-641 (2016).

87.   M. I. Lebedeva, E. V. Rogozhkina, N. A. Tsyba, S. V. Mashko, A New T7 Rna Polymerase-Driven Expression System Induced Via Thermoamplification of a Recombinant Plasmid Carrying a T7 Promoter Escherichia-Coli Lac Operator. *Gene* **142**, 61-66 (1994).

88.   K. Aran, L. A. Sasso, N. Kamdar, J. D. Zahn, Irreversible, direct bonding of nanoporous polymer membranes to PDMS or glass microdevices. *Lab Chip* **10**, 548-552 (2010).

89.   K. X. Jiao, C. L. Graham, J. Wolff, R. G. Iyer, P. Kohli, Modulating molecular and nanoparticle transport in flexible polydimethylsiloxane membranes. *J Membrane Sci* **401**, 25-32 (2012).

90.   J. F. Nagle, Effect of Headgroup Interactions on Lipid Monolayer and Bilayer Transitions. *B Am Phys Soc* **21**, 59-59 (1976).

91.   J. F. Nagle, Lipid Phase-Transition in Biomembranes. *B Am Phys Soc* **21**, 333-333 (1976).

92.   J. F. Nagle, Energetics of Lipid Bilayer Phase-Transitions. *Biophys J* **17**, A49-A49 (1977).

93.   J. F. Nagle, Theory of the Main Lipid Bilayer Phase-Transition. *Annu Rev Phys Chem* **31**, 157-195 (1980).

94.   C. W. Coyne *et al.*, Lipid Bilayer Vesicle Generation Using Microfluidic Jetting. *Jove-J Vis Exp*, (2014).

95.   J. C. Stachowiak *et al.*, Unilamellar vesicle formation and encapsulation by microfluidic jetting. *P Natl Acad Sci USA* **105**, 4697-4702 (2008).

96.   N. Berger, A. Sachse, J. Bender, R. Schubert, M. Brandl, Filter extrusion of liposomes using different devices: comparison of liposome size, encapsulation efficiency, and process characteristics. *Int J Pharmaceut* **223**, 55-68 (2001).

97.   S. M. Johnson, N. Buttress, Osmotic Insensitivity of Sonicated Liposomes and Density of Phospholipid-Cholesterol Mixtures. *Biochim Biophys Acta* **307**, 20-26 (1973).

98.   L. M. Were, B. D. Bruce, P. M. Davidson, J. Weiss, Size, stability, and entrapment efficiency of phospholipid nanocapsules containing polypeptide antimicrobials. *J Agr Food Chem* **51**, 8073-8079 (2003).

99.   E. Betzig *et al.*, Imaging intracellular fluorescent proteins at nanometer resolution. *Science* **313**, 1642-1645 (2006).

100.   H. Du, P. Chandaroy, S. W. Hui, Grafted poly-(ethylene glycol) on lipid surfaces inhibits protein adsorption and cell adhesion. *Bba-Biomembranes* **1326**, 236-248 (1997).

101. H. F. Zhu, J. B. Li, Recognition of biotin-functionalized liposomes. *Chinese Chem Lett* **14**, 832-835 (2003).

102. L. M. Gonzalez, W. C. Ruder, A. P. Mitchell, W. C. Messner, P. R. LeDuc, Sudden motility reversal indicates sensing of magnetic field gradients in Magnetospirillum magneticum AMB-1 strain. *ISME J* **9**, 1399-1409 (2015).

103. L. M. Gonzalez, W. C. Ruder, P. R. Leduc, W. C. Messner, Controlling magnetotactic bacteria through an integrated nanofabricated metallic island and optical microscope approach. *Sci Rep* **4**, 4104 (2014).

104. .

105. W. C. Ruder, C. P. Hsu, B. D. Edelman, Jr., R. Schwartz, P. R. Leduc, Biological colloid engineering: Self-assembly of dipolar ferromagnetic chains in a functionalized biogenic ferrofluid. *Appl Phys Lett* **101**, 63701 (2012).

106. T. Keren-Kaplan *et al.*, Synthetic biology approach to reconstituting the ubiquitylation cascade in bacteria. *Embo J* **31**, 378-390 (2012).

107. W. C. Ruder *et al.*, Three-dimensional microfiber devices that mimic physiological environments to probe cell mechanics and signaling. *Lab Chip* **12**, 1775-1779 (2012).

108. R. Jahn, T. Lang, T. C. Sudhof, Membrane fusion. *Cell* **112**, 519-533 (2003).

109. R. Jahn, H. Grubmuller, Membrane fusion. *Curr Opin Cell Biol* **14**, 488-495 (2002).

110. R. Jahn, Principles of exocytosis and membrane fusion. *Ann Ny Acad Sci* **1014**, 170-178 (2004).

111. G. van den Bogaart, R. Jahn, Inside insight to membrane fusion. *P Natl Acad Sci USA* **108**, 11729-11730 (2011).

112. R. Jahn, Towards a molecular understanding of membrane fusion. *Eur J Cell Biol* **82**, 114-115 (2003).

113. T. Weber *et al.*, SNAREpins: Minimal machinery for membrane fusion. *Cell* **92**, 759-772 (1998).

114. L. H. Cai *et al.*, Soft Poly(dimethylsiloxane) Elastomers from Architecture-Driven Entanglement Free Design. *Adv Mater* **27**, 5132-5140 (2015).

115. T. Sollner *et al.*, Snap Receptors Implicated in Vesicle Targeting and Fusion. *Nature* **362**, 318-324 (1993).

116. M. L. Immordino, F. Dosio, L. Cattel, Stealth liposomes: review of the basic science, rationale, and clinical applications, existing and potential. *Int J Nanomed* **1**, 297-315 (2006).

117. J. Filipovic-Grcic, N. Skalko-Basnet, I. Jalsenjak, Mucoadhesive chitosan-coated liposomes: characteristics and stability. *J Microencapsul* **18**, 3-12 (2001).

118. M. Zaru, M. L. Manca, A. M. Fadda, S. G. Antimisiaris, Chitosan-coated liposomes for delivery to lungs by nebulisation. *Colloid Surface B* **71**, 88-95 (2009).

119. H. W. Tan, M. Misran, Polysaccharide-anchored fatty acid liposome. *Int J Pharmaceut* **441**, 414-423 (2013).

120. R. Zheng *et al.*, Liposomes tethered to a biopolymer film through the hydrophobic effect create a highly effective lubricating surface. *Soft Matter* **10**, 9226-9229 (2014).

121. L. M. Crowe, J. H. Crowe, A. Rudolph, C. Womersley, L. Appel, Preservation of Freeze-Dried Liposomes by Trehalose. *Arch Biochem Biophys* **242**, 240-247 (1985).

122. T. Handa, H. Takeuchi, Y. Ohokubo, Y. Kawashima, Lyophilized Liposomes Prepared by a Modified Reversed-Phase Evaporation Method. *Chem Pharm Bull* **35**, 748-755 (1987).

123. H. Jizomoto, K. Hirano, Encapsulation of Drugs by Lyophilized Empty Dipalmitoylphosphatidylcholine Liposomes - Effect of Calcium-Ion. *Chem Pharm Bull* **37**, 3066-3069 (1989).

124. P. M. Shulkin, S. E. Seltzer, M. A. Davis, D. F. Adams, Lyophilized Liposomes - a Method for Long-Term Storage. *Invest Radiol* **18**, S26-S26 (1983).

125. A. E. McKellar, A. P. Hendry, How humans differ from other animals in their levels of morphological variation. *Plos One* **4**, e6876 (2009).

126. F. Pampaloni, E. G. Reynaud, E. H. Stelzer, The third dimension bridges the gap between cell culture and live tissue. *Nat Rev Mol Cell Biol* **8**, 839-845 (2007).

127. D. Huh, G. A. Hamilton, D. E. Ingber, From 3D cell culture to organs-on-chips. *Trends Cell Biol* **21**, 745-754 (2011).

128. J. El-Ali, P. K. Sorger, K. F. Jensen, Cells on chips. *Nature* **442**, 403-411 (2006).

129. C. Moraes, G. Mehta, S. C. Lesher-Perez, S. Takayama, Organs-on-a-chip: a focus on compartmentalized microdevices. *Ann Biomed Eng* **40**, 1211-1227 (2012).

130. D. Huh *et al.*, Reconstituting organ-level lung functions on a chip. *Science* **328**, 1662-1668 (2010).

131. H. J. Kim, J. Lee, J. H. Choi, A. Bahinski, D. E. Ingber, Co-culture of Living Microbiome with Microengineered Human Intestinal Villi in a Gut-on-a-Chip Microfluidic Device. *J Vis Exp*, (2016).

132. H. J. Kim, H. Li, J. J. Collins, D. E. Ingber, Contributions of microbiome and mechanical deformation to intestinal bacterial overgrowth and inflammation in a human gut-on-a-chip. *Proc Natl Acad Sci U S A* **113**, E7-15 (2016).

133. H. J. Kim, D. E. Ingber, Gut-on-a-Chip microenvironment induces human intestinal cells to undergo villus differentiation. *Integr Biol (Camb)* **5**, 1130-1140 (2013).

134. H. J. Kim, D. Huh, G. Hamilton, D. E. Ingber, Human gut-on-a-chip inhabited by microbial flora that experiences intestinal peristalsis-like motions and flow. *Lab Chip* **12**, 2165-2174 (2012).

135. J. Zhou, L. E. Niklason, Microfluidic artificial "vessels" for dynamic mechanical stimulation of mesenchymal stem cells. *Integr Biol (Camb)* **4**, 1487-1497 (2012).

136. M. C. Shih, S. H. Tseng, Y. S. Weng, I. M. Chu, C. H. Liu, A microfluidic device mimicking acinar concentration gradients across the liver acinus. *Biomed Microdevices* **15**, 767-780 (2013).

137. N. Suwanpayak *et al.*, Blood cleaner on-chip design for artificial human kidney manipulation. *Int J Nanomedicine* **6**, 957-964 (2011).

138. J. Kuttenberger, E. Polska, B. M. Schaefer, A novel three-dimensional bone chip organ culture. *Clin Oral Investig* **17**, 1547-1555 (2013).

139. A. M. Ghaemmaghami, M. J. Hancock, H. Harrington, H. Kaji, A. Khademhosseini, Biomimetic tissues on a chip for drug discovery. *Drug Discov Today* **17**, 173-181 (2012).

140. C. Tan, S. Saurabh, M. P. Bruchez, R. Schwartz, P. Leduc, Molecular crowding shapes gene expression in synthetic cellular nanosystems. *Nat Nanotechnol* **8**, 602-608 (2013).